DISSERTATION

zur Erlangung des akademischen Grades „Doktor der Naturwissenschaften" an der Fakultät für Geowissenschaften, Geographie und Astronomie der Universität Wien:

"DEFORMATION AROUND BASIN SCALE NORMAL FAULTS"

Verfasser

Mag. Darko Spahić

Wien, Oktober 2010

Studienkennzahl It Studienblatt A 091 426

Dissertationgebiet It. Studienblatt Geologie

Betreuerin/Betreuer: Prof. Dr. Bernhard Grasemann

"Oni koji žele nešto da nauče nikada nisu bili besposleni!"

("Those who have wish to learn, they never had been vacuous")

CHARLES-LOUIS DE SECONDAT, BARON DE LA BRÈDE ET DE MONTESQUIEU (1689-1755)

Table of Contents

Abstract

Faults in the earth crust occur within large range of scales from micro-scale over mesoscopic to large basin scale faults. Frequently deformation associated with faulting is not only limited to the fault plane alone, but rather forms a combination with continuous near field deformation in the wall rock, a phenomenon that is generally called fault drag.

The correct interpretation and recognition of fault drag is fundamental for the reconstruction of the fault history and determination of fault kinematics, as well as prediction in areas of limited exposure or beyond comprehensive seismic resolution. Based on fault analyses derived from 3D visualization of natural examples of fault drag, the importance of fault geometry for the deformation of marker horizons around faults is investigated. The complex 3D structural models presented here are based on a combination of geophysical datasets and geological fieldwork.

On an outcrop scale example of fault drag in the hanging wall of a normal fault, located at St. Margarethen, Burgenland, Austria, data from Ground Penetrating Radar (GPR) measurements, detailed mapping and terrestrial laser scanning were used to construct a high-resolution structural model of the fault plane, the deformed marker horizons and associated secondary faults. In order to obtain geometrical information about the largely unexposed master fault surface, a standard listric balancing dip domain technique was employed. The results indicate that for this normal fault a listric shape can be excluded, as the constructed fault has a geologically meaningless shape cutting upsection into the sedimentary strata. This kinematic modeling result is additionally supported by the observation of deformed horizons in the footwall of the structure. Alternatively, a planar fault model with reverse drag of markers in the hanging wall and footwall is proposed.

7

A second part of this thesis investigates a large scale normal fault in the central Vienna Basin from commercial 3D seismic data. In addition to detailed conventional fault analysis (displacement and fault shape), syn-and anticlinal structures of sedimentary horizons occurring both in hanging wall and footwall are assessed. Reverse drag geometries of variable magnitudes are found to correlate with local displacement maxima along the fault. In contrast, normal drag is observed along segment boundaries and relay zones. Thus, the detailed documentation of the distribution, type and magnitude of fault drag provides additional information on the fault evolution, as initial fault segments as well as linkage or relay zones can be identified.

Zusammenfassung

In der Erdkruste treten Störungen über einen großen Bereich von mikro- über makroskopisch bis zu weitläufigen Störungen in großen Becken auf. Häufig ist die Deformation im Zusammenhang mit Störungen nicht nur auf die Störungsfläche selbst begrenzt, sondern ist vielmehr eine Kombination mit kontinuierlichen Verbiegung des Gesteins in der Störungsumgebung. Dieses Phänomen wird als *fault drag* bezeichnet.

Die korrekte Interpretation und Erkennung von fault drag ist wesentlich für die Rekonstruierung der Störungsgeschichte, für die Bestimmung der Störungskinematik und für die Störungsprognose in schlecht aufgeschlossenen Gebieten oder bei unzureichender Seismikauflösung.

Der Einfluss der Störungsgeometrie auf die Deformation von Markerhorizonten in der Umgebung von Störungen basiert auf Störungsanalysen, die durch 3D Visualisierung von natürlichen Beispielen von fault drag untersucht wurden. Die komplexen strukturellen Modelle, die in dieser Arbeit untersucht worden sind, beruhen auf einer Kombination aus geophysikalischen Datensätzen und geologischer Feldarbeit.

Anhand eines Beispiels von fault drag im Aufschlussmaßstab im Hangenden einer Abschiebung in St. Margarethen (Burgenland, Österreich) konnte mit Daten von Georadarmessungen (GPR), einer ausführlichen Kartierung und einem terrestrischen Laser Scan ein hochauflösendes strukturelles Model der Störungsfläche, der deformierten Markerhorizonte und den damit verbundenen sekundären Störungen konstruiert werden.

Eine Methode zur Bilanzierung von listrischen Störungen wurde zur kinematischen Analyse angewendet, um geometrische Informationen über die weitgehend schlecht aufgeschlossene Hauptabschiebung zu bekommen. Die Ergebnisse zeigen, dass eine listrische Störungsgeometrie für diese

Abschiebung ausgeschlossen werden kann, da die konstruierte Störung wieder nach oben in die überlagernden Sedimente schneidet und somit geologisch nicht sinnvoll ist. Die Ergebnisse dieser kinematischen Analysen werden noch zusätzlich unterstützt durch das Auftreten von deformierten Horizonten im Liegenden der Abschiebung. Alternativ wird eine planare Störungsgeometrie mit reverse drag von Markern im Hangenden und im Liegenden der Abschiebung vorgeschlagen.

Der zweite Teil dieser Arbeit untersucht eine Abschiebung im großen Maßstab im zentralen Wiener Becken anhand von kommerziellen 3D Seismikdaten. Zusätzlich zu der konventionellen Störungsanalyse (Versatz und Störungsform) sind syn- und antiklinale Strukturen von sedimentären Horizonten, die im Liegenden und im Hangenden der Abschiebung zu finden waren, kartiert worden. Es konnte gezeigt werden, dass reverse drag-Geometrien unterschiedlich starker Magnituden mit lokalen Versatzmaxima entlang der Störung korrelieren. Im Unterschied dazu konnte normal drag entlang von Segmenträndern und Transferzonen nachgewiesen werden.

Daraus folgt, dass die ausführliche Dokumentation der Verteilung, die Art und die Magnitude des fault drag zusätzliche Information über die Störungsentstehung liefert, da sowohl initiale Störungssegmente als auch Verbindungs- und Transferzonen identifiziert werden können.

Проширени абстракт

Раседи у Земљиној кори се могу појавити у различитим димензијама, од микро-, преко мезо- до великих басенских раседа. Често деформација која се настаје синхроно са раседом није ограничена искључиво на раседну површ, већ је то комбинација раседа и континуиране деформације у околним стенама, који се генерално назива Реверсни Драг (Reverse Drag).

Правилна интерпретатција и препознавање реверсног драг-а је основа за реконструкцију постепеног развоја и историје раседне кинематике, као за предикцију у подручијима лимитираних изданака или подручја изван одговарајуче резулуције сеизмичких података. Базирано на анализи раседа изведеној на основу тродимензионалне анализе визуализованих раседа и њихових драг-ова, важност геометрије седимената око раседа и њихова еволуција су детаљно истраживане.

Комплексни тродимензионални структурно-геолошки модели су базирани на комбинацији геофизичких подака и теренског геолошког рада уз који је коришћена најновија ласерка технологија. Сви подаци као што су коненционалне регионално-геолошки подаци и резултати теренског картирања (дифиталне геолошке карте, трасе раседа извучене на ласрског фотографији – ортфото), геофизика (Георадарски снимци - радарграми и тродимензионални сеизмички блок) као и географски подаци (координате узете помоћу DGPS -а тј. Дигиталног Глобал Поситионинг Система као и аероснимци) су интегрисани у Географски Информациони Систем (GIS) и накнадно у тродимензионално структурно-геолошке моделе.

Деформације настале близу површине анализиране су путем комбинацијом Георадарског мерења тј снимања, теребским картирањем

која су овбавњена у близини шљункаре (тип површинског копа) која се налази Ст.Маргаретену, Бургенланд, Аустрија. Истраживано подручје је лоцирано у оквиру источне маргине Ајзенштат-Шопронског басена који сам под-басен Бечког басена. У шљункари средњемиоценска сукцесија се сатоји од слојева конгломерата, песковитих конгломерата, финозрних пескова и алервприта варијабилне дебњине који су видњиви дуж од око 10м зида шњункаре који се пружа правцем запад – исток. Ови неконсолидовани седименти су пресечени бројним коњугативним раседима правца пружања север – југ који тону ка истоку без видљивог синседиментног прираста слојева. Ови раседи смичу, повлаче и померају ову велику седиментну сукцесију која има облик антиформе. Овакав облик седимената указује да ова кластична сукцесија је у ствари разкровљена повлата већег раседа регионалног значаја који је лоциран у близини.

Да бих се добила трећа димензија картираних раседа и околних структура, мрежа 40-то мегахерцних георадрграма је снимљена. Радаргрми су постављени паралелно и управно на картирани изданак. Интерпретација раседних структура снимљених радаргрмима, је подпомогнута ортофотографијом која је навучена на претходно снимљени ласерски скен изданка. Пошто су подаци са, и иза изданка интегрисани у тродимензионални структурно-геолошки модел, да би се добила информација о дубинској геометрији раседа, стандарним метод „балансирања падних домена" је коришћен.

Студија великих басенсих деформација је базирана на основу утицаја раста сегментованог раседа на миценсе седименте централног Бечког басена. Обострани утицај је приказан комбинацијом тродимензионалних и кинематских параметара. Испитивани су маркер хоризонти у повлати и подини Маркграјфнојзидл раседа, где према 3Д сеизмичким подацима раседна површ истог је неправилног-закривљеног облика. Након формирања коплексног 3Д модела, почетна аистраживања су базирана на конвенцијалној анализи раседа

12

приказујући орјентацију, дисплејсмент и курватуру као тродимензионалне карте. Ова три параметра су обезбедили податке о кинематици и морфологији раседа, међутим резултати нсиу били довољни да се реконструише еволуција раседа и дефинише шема сегментације.

Како би се одредили старији сегменти раседа, ово истраживање се фокусира на појаву нормалног и реверсног драг-а на маркер хоризонтима, пре свега о домену повлате. Анализом односа између геометрије раседне површине и раседног драг-а, формирана је метода која допушта олакшану идентификацију индивидуалних раседних сегмената па и фазну реконструкцију раседне еволуције.

Acknowledgements

constructive reviews, especially detailed, careful reviews of the manuscripts that are eventually resulted in remarkable speed of the papers acceptance.

I would like to thank to my family, who supported and encouraged me during my years in Vienna, but also in a turbulent time before, and therefore I would like to dedicate this PhD Thesis to them. Especially I would like to thank to my mother, Prof. Svetlana Spahic for the overall support, encouragement, and introduction to a magnificent 3D world through the Plane Geometry and Perspective in Art lessons.

I dedicate my deepest gratitude for guidance and support through B.Sc and M.Sc studies to my late mentor and friend Prof. Dr. Milun Marovic that was tragically killed in 2009 during the geological mapping fieldwork of Libyan Kufra Basin. Also, I own endless gratitude to my late grandmother Prof. Trifunovic Evdokia (Daca) that during my early school time pass to me love for Natural Sciences, Mathematics and Earth Sciences before all.

1.Introduction

Faults in the Earth's crust occur at a large range of scales from microscopic to the scale of plate boundaries with hundreds of kilometers in length. Frequently, deformation associated with faulting is not only expressed by discontinuous displacement along a distinct fault surface, but is associated with continuous deformation in the surrounding rock (Pollard & Segall, 1987), which is expressed by folding of originally planar layers. Following the convention of Hamblin (1965) two types of fault drag may occur, normal and reverse drag, which are either convex (normal drag) or concave (reverse drag) in the direction of slip along the fault. In many investigations deflected markers with reverse drag geometry are exclusively used as evidence for a listric fault geometry (e.g. Tearpock and Bischke, 2003), where displacement along the fault is accommodated by a rollover anticline in the hanging wall. However, numerical and analogue studies (e.g. Reches and Eidelman, 1995; Grasemann et al., 2003) illustrated the fact that reverse drag forms in association with slip on planar faults of finite extent, if the angle between the fault and the marker is roughly higher than 30°. Additionally, it was shown that reverse drag is not necessarily related to a reactivation of a normal fault as a thrust in a compressional tectonic regime. This alternative interpretation of fault drag has significant implications for e.g. estimates of hydrocarbon volumes in fault-related anticlinal structures, deformation history of regions with crustal extension, and earthquake hazards associated with continental normal faults (e.g. Resor, 2008).

1.1 <u>Definition of fault drag, current state of research and motivation</u>

Fault drag geometries and flanking structures have been described and analyzed by, e.g. Barnett et al., 1987; Passchier, 2001; Exner et al. 2004; Coelho et al. 2005; Grasemann et al. 2005 and Wiesmayr and Grasemann, 2005 on field outcrop scale or analogue and numerical modeling.

Investigating the cause of host rock deformation numerous recent publications have established that the perturbation strain generated by slip along a distinct fault plane compensates the incompatibilities between the background strain and the displacement along the fault by deflection of originally planar marker layers (e.g. Passchier 2001; Grasemann et al. 2001; Passchier et al. 2005; Grasemann et al. 2005; Exner and Dabrowski, 2010).

Following on these basic results from ideal elliptical, planar and isolated faults and recognizing that host-rock deformation near faults is a direct consequence of slip distribution and the mechanical interaction of faults, this study focused on the geometrical characteristics non-planar, irregular natural fault surafces and the associated host-rock deformation on outcrop and basin scale. The results provided a tool that can lead to better assessment of geometrical features, reconstruction of fault growth and understanding of mechanical properties of propagating faults.

1.2 <u>Aim and approach</u>

In order to identify natural fault drag geometries, the study was divided in three main stages:

- A natural three-dimensional example of deflected markers in the vicinity of a normal fault at the meso-scale was assessed with the aim to construct, a surface-subsurface structural 3D model.

- Based on the structural data collected in the first stage, kinematic balancing techniques (depth-to-detachment restoration, Tearpock and Bischke, 2003) are employed to constrain the geometry of the unexposed parts of the fault. Form the results, a plausible scenario for the formation of the observed fold structures in the hanging wall and footwall of the investigated normal fault is deduced.

- From a commercial 3D seismic dataset in the central Vienna basin, deflected sedimentary horizons adjacent to a major normal fault are mapped in high accuracy. In combination with a detailed fault analysis, the initiation and evolution of a large normal fault is constrained.

The study area of the project is located in thee Vienna Basin (E Austria) and the southeasterly adjacent Eisenstadt-Sopron Basin (Fig. 1-1), where natural fault zones are developed in Miocene sediments.

The fault investigated in stage 1 &2 is situated at the Eastern margin of the Eisenstadt-Sporon Basin and has a length of a few kilometers in strike and at least 40 m of height. This master fault and the associated smaller faults in the hanging wall layers were mapped in a quarry and a three-dimensional structural model was generated by from Terrestrial Laser Scanning and Ground Penetrating Radar data.

The normal fault analyzed in stage 3, the Markgrafneusiedl fault in the central Vienna Basin, has an extent of several tens of kilometers along strike and reaches from the surface down to ~2250 ms of TWT down to the pre-Neogene basement. The three-dimensional seismic dataset (Seymatzdue) was provided by the OMV AG, together with existing interpretations of stratigraphic horizons and borehole data.
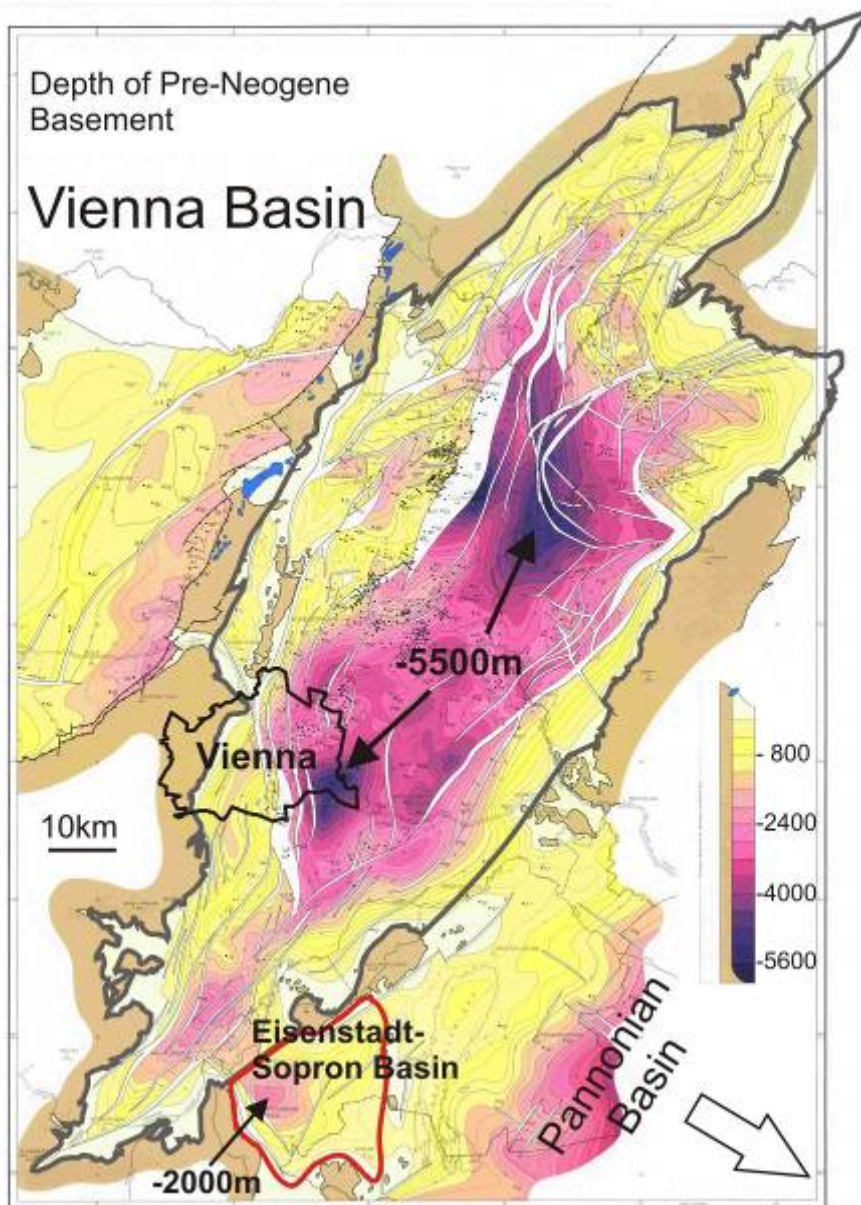
Fig 1-1. Investigated areas (Vienna and Eisenstadt-Sopron Basins) positioned within the structural map of the pre-Neogene basement (modified after Kröll & Wessely, 1993).

1.3 <u>**Normal fault systems - geometrical properties and linkage processes**</u>

Normal faults are of particular importance in basin formation and hydrocarbon development, whereby the major role can be subdivided in two

equally significant characteristics, i.e. fault geometry and role of interaction and linkage between fault segments.

1.3.1 Listric faults

The most common interpretation of host-rock deformation is the concept of a hanging-wall rollover anticline of layers above a listric normal fault (Fig. 1-2) with or without syn-tectionic growth strata (e.g. Shelton, 1984; McClay and Scott, 1991). Three essential features characterize a listric normal fault: a flat detachment surface, a rigid footwall, and rollover anticline in the hanging wall (e.g. Shelton, 1984). Numerous models aimed to reproduce the hanging wall deformation, whereby the most prominent is the analogue model of McClay and Scott, 1991. The analogue model is based on the rigid footwall that is thereby represented by a suitable shaped cardboard upon which a rubber slice represents a listric fault curving into a flat detachment at the base of the model.
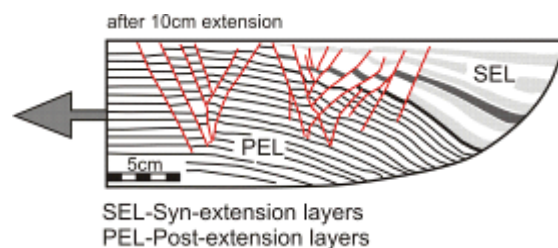
Fig 1-2. Analogue model of growth strata deposited above an active listric normal fault, which merges with a layer-parallel detachment at depth (modified after Yamada and McClay, 2002).

The hanging wall deformation pattern above a ramp-flat detachment can be divided in four zones: (i) an upper zone of rotational deformation adjacent to the upper and steeper part of the listric fault; (ii) a translation zone producing the upper rollover and associated crestal collapse system, (iii) a rotational zone encompassing the ramp syncline and the lower sections of the rollover; (iv) a translation zone where the entire hanging wall is translated horizontally above the flat detachment.

Generally, two kinematic groups of rollover systems are distinguished: (1) the aforementioned fault rollovers induced by extensional displacement along a listric fault whereby the footwall behaves as a rigid body (listric faults sensu strictu) and (2) 'expulsion rollovers' which develop due to the withdrawal of a weak material layer (e.g. salt or clay) within the footwall layers (for a review see Krézsek et al., 2008; Dutton et al., 2004 and references cited therein). By using scaled analogue experiments with layered brittle and ductile materials Krézsek et al., (2008) simulated the development of listric growth faults and expulsion rollover systems during gravitational spreading of a passive margin sedimentary wedge detached on salt (Fig 1-3).
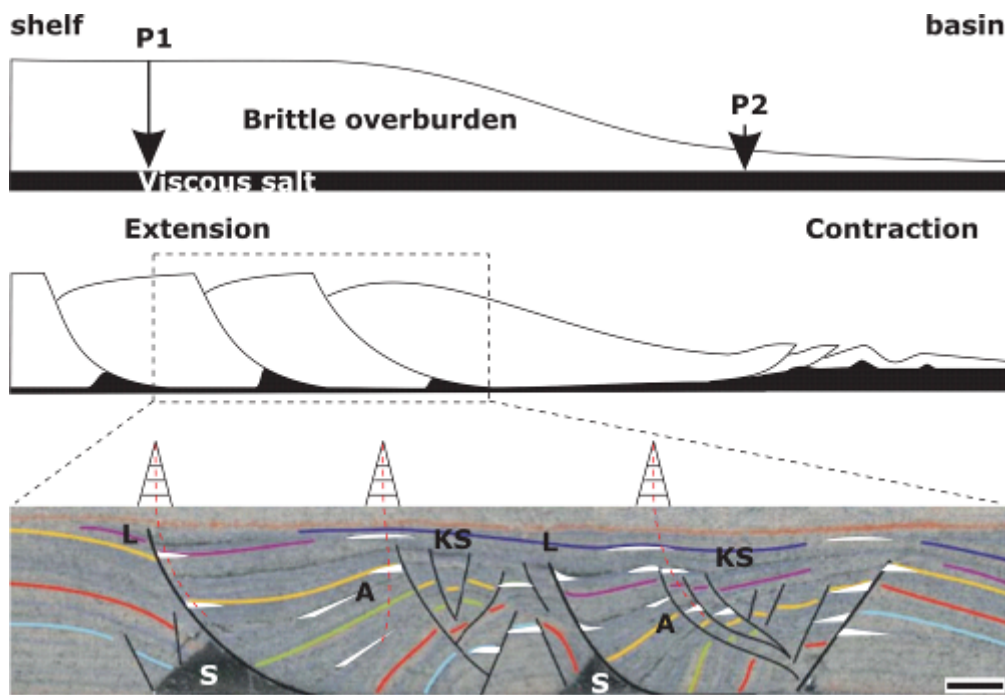
Fig 1-3. Schematic diagram illustrating the effect of different overburden thickness on the generation of listric faults above a weak layer (modified after Krezsek et al., 2008).

The results indicate that the mobilization of salt controls the strain history of local faults developed in the sedimentary wedge. Hence, the rollover kinematics is strongly related to sedimentation patterns and their rate, i.e. portions with higher deposition rate will have a larger mass and

therefore such constellation of geological bodies can induce salt expulsion resulting in a listric normal fault geometry.

Both models of listric normal faults have a different concept of the behavior of the footwall. Unlike the rafting model that assumes a weak or ductile detachment and footwall, the group of listric fault models sensu strictu assumes that the footwall during ongoing deformation behaves as a rigid body. In many cases, such an assumption has poor geological evidence and is mechanically not valid if the footwall sediments are identical to the hanging wall strata. Grasemann et al., 2005 listed several reasons that contribute to the perception that fault footwalls are rigid. The first is due to the fact that the drag effect in the footwall that can be much less than those in hanging wall. A second reason that might contribute to the perception that fault footwalls are rigid is that reverse drag on either side of the fault may be associated with little or no drag on the opposing side, especially if structural levels above or below the central marker are observed. Finally, physical models of listric faults are simple based on a listric fault geometry predefined by the model boundary conditions. However, more recent listric models (Imber et al., 2003) revealed that footwall deformation can play an import role, e.g. by footwall collapse where the active bounding fault steps back into the footwall block.

1.3.2 Planar faults of finite length

Although concept of a listric fault is widely accepted, in many cases the listric (downward-flattening) geometry of the fault surface is poorly constrained, and is more an imposed conceptual model than an observation (Barnett et al., 1987; Grasemann et al., 2005). In other words, often a normal fault in nature is only partially constrained, as e.g. exposed fault traces in an outcrop do not display the entire fault geometry, or the quality of seismic data can decrease with depth so that the lower fault sections are blurred.

In contrast, fault drag may actually occur along a planar (i.e. non listric) fault of finite length, where slip results in a heterogeneous stress and displacement field develop within the rock adjacent to the fault (Grasemann et al., 2005, Fig 1-4).
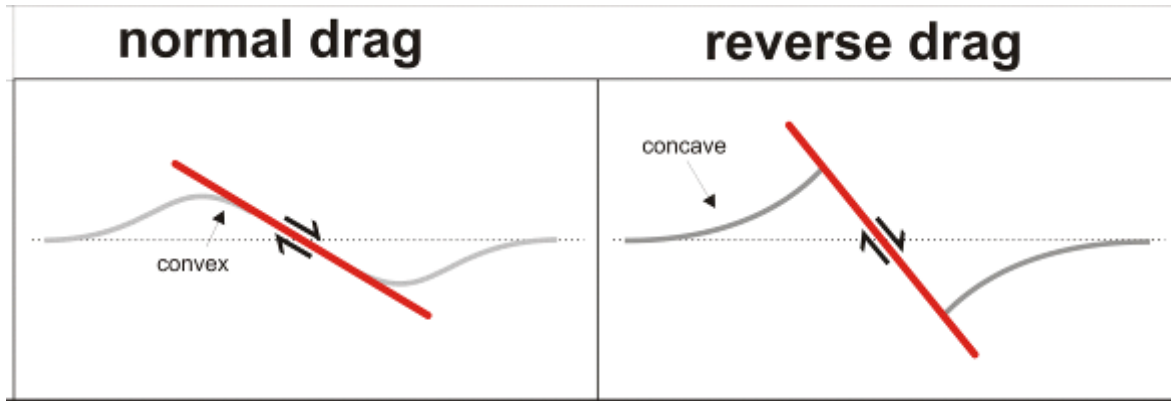
Fig 1-4. Fault drag of a central marker along a normal fault. Normal drag refers to markers that are convex in the direction of slip and reverse drag to markers that are concave in the direction of slip (modified after Grasemann et al., 2005).

Using the linear elasticity theory, the geometrically idealized model identified the influencing parameters which result in the formation of fault drag. The discontinuous displacement along the slip surface is compensated by a continuous deformation field in the adjacent matrix, which is also called perturbation strain (e.g. Passchier et al., 2005). Due to this heterogeneous deformation field, originally straight markers are deflected in the vicinity of the fault. It was shown that exclusively the angular relationship between the fault and the maker determines the type of drag, i.e. at low angles (<30°) normal drag, at high angles (>30°) reverse drag is developed. Several other numerical and analogue studies investigated the development of fault drag (or flanking structures) around slip surfaces and analyzed the variable geometries which occur in different flow kinematics and geometric relationships between the fault and the markers (e.g. Grasemann et al., 2003; Exner et al., 2004; Wiesmayr and Grasemann, 2005; Kocher and

Mancktelow, 2005 and 2006). Most importantly, all the models showed that fault drag is developed in both hanging wall and footwall domain.

During progressive deformation, an initially straight marker line passing through the centre of the fault is displaced. This deflected central marker forms symmetrical folds, which are convex (i.e. normal drag) in the direction of shear along the discontinuity; offset and deflection of the non-central marker lines decrease towards the tips of the fault (Exner et al, 2004). This decrease in intensity of deflection is subsequently investigated in the process of fault growth by segment linkage.

1.4 <u>Fault growth by segment linkage</u>

Conventional fault growth models suggest that the enlargement of elliptical faults is a function of a progressive increase of displacement with time (e.g. Walsh et al., 2002). Mechanically, a systematic increase of displacement and fault length produces a larger fault. Linked normal faults usually consist of complex zones of overstepping and linked segments that affect fault geometry creating irregularities of the fault plane along strike and dip. In addition to geometrical irregularities, a fault that is a result of segment linkage through time displays irregular displacement patterns (see chapter 5 Peacock, 2002). A good example of how geometry can vary along a normal fault is illustrated in a summary figure of Marchal et al., 2003, see Fig 1-5.

The most common technique used to analyze the accumulation of slip and finite displacement on a fault are displacement – distance plots (D-x plot). The success of this technique is largely due to the fact that fault segments and linked faults exhibit a variability in displacement-distance profiles, in contrast do isolated faults with continuous displacement profiles. Such irregularities originate from the interaction and linkage of fault segments.
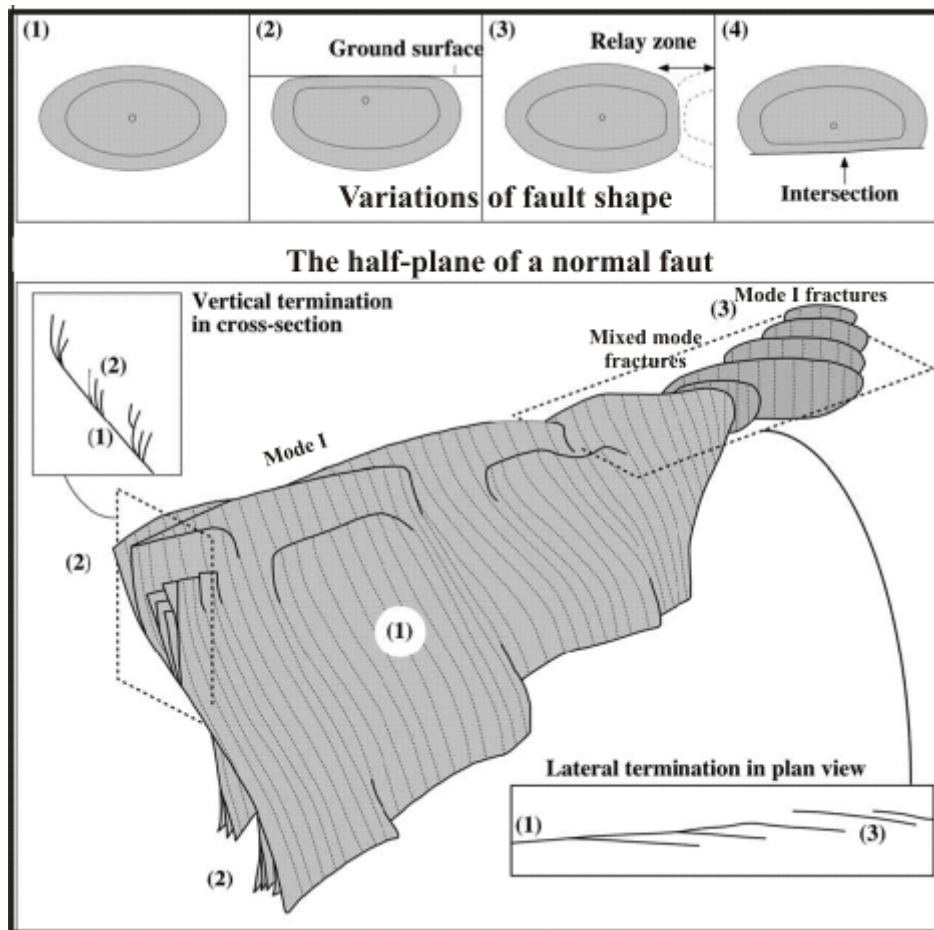
Fig 1-5. Upper section: variations in normal fault shape: (1) the simplest shape for a blind fault is an elliptical plane; (2) Fault shape affected by interaction with other features: restriction by the ground surface; (3) Overlap with another fault plane forming a relay zone; (4) Intersection with another fault plane. Three basic patterns that may combine to form complex fault shapes. Lower section: (1) The half plane of a normal fault composed of a principal plane; (2) Branched secondary fault planes at the vertical termination; (3) en-échelon secondary fault planes at the lateral termination (modified after Marchal et, 2003).
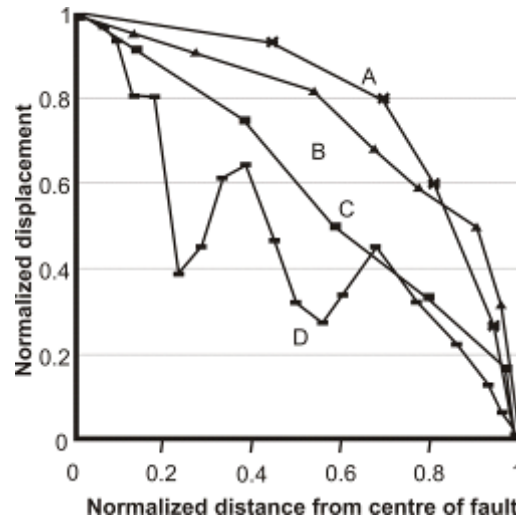
Fig 1-6. Examples of displacement - distance profiles for individual fault segments: A-connected fault, B-offset fault, C-nearly isolated fault, D-complex fault composed of fault segments (modified after Peacock & Sanderson, 1991).

More recently, 3D geometrical analyses of fault surfaces, mostly derived from 3D seismic data provided additional insight in different segmentation patterns (e.g Marchal et al., 2003; Lohr et al., 2008). Using a combination of both tools, a significant progress in deciphering of fault segmentation patterns was achieved.

1.5 <u>Key questions addressed in the thesis</u>

This thesis comprises several interrelated studies that are designed to improve the knowledge of three-dimensional fault mechanics and fault-drag development from basin- to outcrop- scale. The key questions that were addressed by the thesis are:

(1) IS THE OCCURRENCE OF ANTICLINES IN THE HANING WALL OF A NORMAL FAULT A RELIABLE INDICATOR FOR A LISTRIC FAULT SHAPE?

(2) CAN FAULT DRAG OCCUR NEAR LARGE BASIN-SCALE FAULTS?

(3) IS IT POSSIBLE TO OBSERVE NORMAL AND REVERSE DRAG ALONG THE OPPOSITE SIDE OF A LARGE NATURAL FAULT SURFACE?

(4) IS THERE A LINK BETWEEN INDIVIDUAL FAULT DRAG AND FAULT DOMAINS, I.E. CAN FAULT DRAG SERVE AS INDICATOR OF SEGMENTS AND/OR LINKAGE ZONES? IS THE MANGITUDE OF DRAG RELATED TO THE SIZE OF THE FAULT PLANE?

(5) IS FAULT DRAG OF DIFFERENT TYPE (NORMAL OR REVERSE) ANALOGOUS TO THE CORRESPONDING PERIODS OF FAULT GROWTH?

1.6 <u>Outline of the thesis</u>

This PhD thesis was conducted within the FWF project "Modeling of natural fault systems at various scales" and comprises results from three-dimensional structural modeling of natural fault surfaces and the associated deformation in the surrounding rock. Each phase of the research is represented by a publication submitted or already approved for publishing in international peer-reviewed scientific journals.

Following on this introductory chapter, the next part of the thesis (chapter 2, based on an extended abstract in Trabajos de Geologia), is focused on the ground-penetrating radar study conducted in a Miocene, unconsolidated sediments at a gravel pit in the Eisenstadt-Sopron Basin. Details about the various acquisition techniques, processing and finally the construction of a 3D structural model are provided.

Since near-surface geophysical methods provided no satisfactory insight in the deeper structural levels, in chapter 3 more detailed field observations and the previously described shallow subsurface visualization techniques were combined to construct a balanced cross section of the

normal fault and the overlying sedimentary strata. This chapter is published in the International Journal of Earth Sciences. The results of this study lead to the conclusion that the listric fault model is not applicable for this normal fault, and instead a reverse drag of markers along a planar fault of finite length is proposed.

In Chapter 4, the effects of segment linkage were analyzed around a large-scale normal fault from 3D seismic data of the central Vienna Basin. From detailed fault analysis and mapping of the adjacent marker horizons, numerous fault segments could be identified. Most importantly, the usefulness of a detailed structural analysis of fault drag is demonstrated, as individual segments can be determined from the distribution and magnitude of fault drag. This chapter is submitted to the Journal of Geophysical Research for publication.

A final synthesis in chapter 5 summarizes the results of the previous chapters in a general context, discusses specific similarities and differences of fault drag with respect to fault size and geometry, and finally gives an outlook for further research focus arising from unsolved problems and findings of this thesis.

References

Barnett, J. A. M., Mortimer, J., Rippon, J.H., Walsh, J.J., Watterson, J., 1987. Displacement Geometry in the Volume Containing a Single Normal Fault. American Association of Petroleum Geologists B 71, 925-937.

Exner, U., Mancktelow, N.S., Grasemann, B., 2004. Progressive development of s-type flanking folds in simple shear. Journal of Structural Geology 26, 2191–2201.

Exner, U., Dabrowski, M., 2010. Monoclinic and triclinic 3D flanking structures around elliptical cracks. Journal of Structural Geology, in press.

Dutton, D. M., Lister, D, Trudgill, B.D., Pedro, K. 2004. Three-dimensional geometry and displacement configuration of a fault array from a raft system, Lower Congo, Offshore Angola: Implications for the Neogene turbidite play. In: Davies, R.J., Cartwright, J.A., Stewart, S.A., Lappin, M., Underhill, J.R.. (Ed.), 3D seismic technology: Application to the exploration of sedimentary basins. Geological Society, London, Memoirs, 29, 133-142.

Grasemann, B., Stüwe, K., 2001. The development of flanking folds during simple shear and their use as kinematic indicators. Journal of Structural Geology 23, 715-724.

Grasemann, B., Martel, S., Passchier, C., 2005. Reverse and normal drag along a fault. Journal of Structural Geology 27, 999-1010.

Hamblin, W. K., 1965. Origin of "reverse drag" on the down-thrown side of normal faults. Geological Society of America Bulletin 76, 1145-1164.

Hinsch, R., Decker K, Wagreich M, 2005. 3-D mapping of segmented active faults in the southern Vienna Basin. Quaternary Science Revievs 24, 321-336.

Kocher and Mancktelow, 2005. Dynamic reverse modeling of flanking structures: a source of quantitative kinematic information. Journal of Structural Geology 27, 1346-1354.

Kocher and Mancktelow, 2006. Flanking structure in anisotropic viscous rock. Journal of Structural Geology 28, 1139-1145.

Krezsek, C., Adam J, Grujic D, 2007. Mechanics of fault and expulsion rollover systems developed on passive margins detached on salt: insights from analogue modelling and optical strain monitoring. Geol Soc Lond Spec Publ 292(1), 103-121.

Kröll, A., Wessely, G, 1993. Wiener Becken und angrenzende Gebiete. Geologische Themenkarte der Republik Österreich 1:200.000. Geologische Bundesanstalt. Wien.

Lohr, T., Krawczyk, C.M., Oncken, O., Tanner, D.C. 2008. Evolution of a fault surface from 3D attribute analysis and displacement measuremants. Journal of Structural Geology 30, 690-700.

Marchal, D., Guiraud, M., Rives, T., 2003. Geometric and morphologic evolution of normal fault planes and traces from 2D to 4D. Journal of Structural Geology 25, 135-158.

McClay, K. R., Scott AD, 1991. Experimental models of hanging wall deformation in ramp-flat listric extensional fault systems. Tectonophysics 188, 85-96.

Passchier, C. W., 2001. Flanking structures. Journal of Structural Geology 23, 951–962.

Passchier, C. W., Mancktelow, N. S., Grasemann, B., 2005. Flow perturbations: a tool to study and characterize heterogeneous deformation. Journal of Structural Geology 27, 1011-1026.

Peacock, D. C. P., Sanderson, D.J., 1991. Displacements, segment linkage and relay ramps in normal fault zones. Journal of Structural Geology 13, 721 - 733.

Peacock, D. C. P., 2002. Propagation, interaction and linkage in normal fault systems. Earth-Science Reviews 58, 121-142.

Pollard, D. D., Segall, P., 1987. Theoretical displacements and stresses near fractures in rocks. . In: Atkinson, B.K. (Ed.), Fracture Mechanics of Rock. Academic Press, London, pp. 277–349.

Resor, P. G., 2008. Deformation associated with a continental normal fault system, western Grand Canyon, Arizona. GSA Bulletin 120, 414-430.

Shelton, W. J., 1984. Listric normal faults, an illustrated summary. Am Assoc Petrol Geol Bull 68, 801-815.

Strauss, P., Harzhauser M, Hinsch R, Wagreich M, 2006. Sequence stratigraphy in a classic pull-apart basin (Neogene, Vienna Basin). A 3D seismic based integrated approach. Geol Carpathica 57, 185-197.

Tearpock, D. J., Bischke, R.E., 2003 Applied Subsurface Geological Mapping. pp 821.

Walsh, J. J., Nicol, A., Childs, C., 2002. An alternative model for the growth of faults. Journal of Structural Geology 24, 1669-1675.

Wiesmayr, G., Grasemann, B., 2005. Sense and non-sense of shear in flanking structures with layer-parallel shortening: implications for faultrelated folds. Journal of Structural Geology 27, 249–264.

Wiesmeyer, G., 2005. Kinematic and mechanical quantification of fault related fold structures. Unpublished PhD Thesis. pp 79.

Yamada, Y., McClay K, 2003. Application of geometric models to inverted listric fault systems in sandbox experiments. Paper 1: 2D hanging wall deformation and section restoration. J of Struc Geol 25, 1551-1560.

2. Possibilities of Ground Penetrating Radar (GPR) in shallow subsurface 3D structural modeling (an example from St. Margareten gravel pit, Eisenstadt-Sopron Basin)

Abstract

Field mapping and ground penetrating radar (GPR) measurements were carried out near a gravel pit located at St. Margarethen, Burgenland, Austria. The investigated area is located at the eastern margin of the Eisenstadt-Sopron Basin, a subbasin of the Vienna Basin. In the gravel pit a Middle Miocene succession consisting of layers of conglomerates, sandy conglomerates, fine-grained sands and silts with variable thicknesses between 1 and 4 m are exceptionally well exposed along a ~10 m high W-E striking wall. The unconsolidated sediments are cut by numerous roughly N-S striking high angle normal faults, offsetting, dragging and tilting the sedimentary layering.

In order to obtain information about the third dimension of the mapped fault structures, a network of sections parallel to the outcrop wall and perpendicular to the faults was investigated with GPR applying centre frequencies ranging from 40 MHz to 80 MHz.

A three-dimensional fault model was constructed from the results of fault mapping and from georeferenced two-dimensional radargrams using the structural modelling software Gocad. Structural and lithological observations from the quarry walls provided crucial information for the interpretation of the radargrams. Combining the fault and horizon mapping from the individual GPR profiles with the information from the adjacent outcrop, triangulated fault planes and sedimentary horizons were generated in the structural model.

2.1 <u>Introduction</u>

The investigation of fault surfaces through geological fieldwork is a common approach to constrain kinematics, timing and structures related to crustal tectonic processes. In many cases, investigated geological structures are only partially exposed, restricting geoscientists to compile a geological interpretation based on measurements and observations of the accessible part of a geological structure. In order to achieve a more complete picture of the structures in the subsurface, geophysical methods represent an essential addition to field geological studies. One of the geophysical tools to analyze shallow subsurface geology, Ground Penetrating Radar (GPR), has been applied from sedimentary geology (e.g. Ékes and Hickin, 2001) , through application in boreholes (e.g. Serzu et al., 2004) up to the non-geological detection of buried mines or illegal waste (e.g. Daniels, 2004).

In recent years, GPR is widely used to study near-surface sediments and more recently in near-surface structural geology. Ground Penetrating Radar (GPR) surveys have been largely concentrated on unraveling of various shallow sedimentary patterns. Beginning with the work of Ulriksen, 1982, the GPR technique has been applied in a large number of case studies to image sedimentary structures, the architecture in the shallow subsurface. Gradual entrance in field of structural geology was promoted by Meschede et al., 1997 whereby use of 2D GPR unraveled rollover structures associated with faults in a Middle Triassic limestone of SW Germany. In other studies, 2D radargramms visualized e.g. the hanging wall of active faults in the Betic Cordillera applying high-resolution frequencies (Reiss et al., 2003), or the delta facies and sedimentary architecture of Cypress Creek, West Vancouver (Roberts et al., 2003). To infer the active Markgrafneusiedl Fault in Pleistocene deposits and to correlate the structures with the deeper fault

levels of the Vienna Basin, 2D GPR profiling was applied using the 40 and 500MHz frequency (Chwatal et al., 2005).

The faults investigated in this study crosscut a Miocene, poorly consolidated succession of gravel and sand. In order to extend the information from the exposed section and characterize the spatial distribution of the faults in 3D, we conducted measurements with Multiple Low Frequency (MLF) 40MHz and 80MHz GPR antennae in the area adjacent to the outcrop wall. In addition to closely spaced (0.5m) 40 MHz sections perpendicular to the strike of the faults, several 80 MHz sections were recorded. The GPR coulisse sections that are perpendicular to the fault strike demonstrate the utility of GPR data and surface mapping for investigation of shallow structures (extension of fault traces). On the other hand, the results of GPR application in unconsolidated near-surface material revealed the high sensitivity of this geophysical method in respect to particular sediment and humidity conditions.

2.2 <u>Regional setting, lithology and geometry of structural features of the investigated area</u>

The Vienna Basin is a pull-apart basin that developed during the Oligocene/Miocene extrusion of the Eastern Alps towards the Pannonian region in the E along sinistral, NE-SW trending strike slip faults and roughly N-S trending normal faults. Part of this regional geodynamic setting is recorded in extensional tectonics in unconsolidated sediments of the Neogene Eisenstadt-Sopron Basin, a sub-basin of the Vienna Basin (Fig 2-1). Along a W-E striking wall in a gravel pit 5 km SSE of St. Margarethen, Burgenland, Austria, several generations of conjugate sets of W and predominantly E-dipping normal faults are exposed in unconsolidated sediments. In the 1:50 000 geological map of the area (REF!), a major fault separating Badenian marls in the E from Sarmatian delta sediments in the W is indicated (Fig. 2-2).
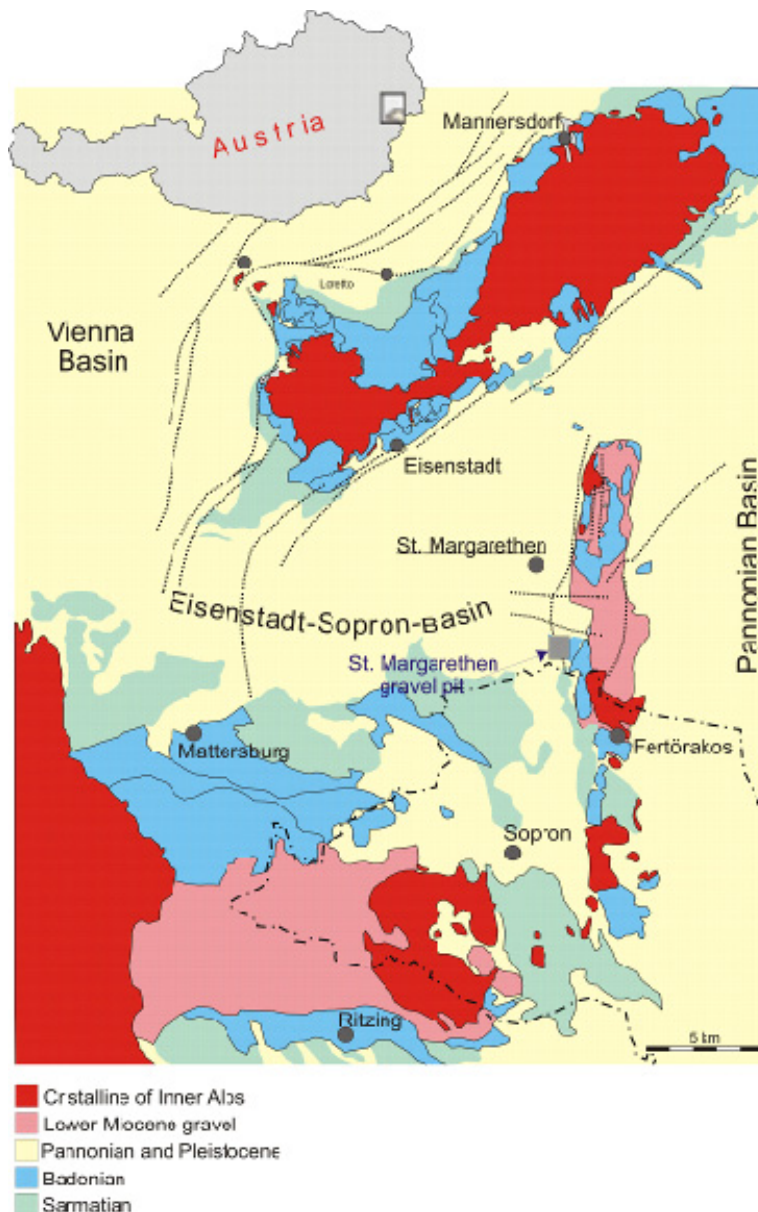
Fig 2-1. Position of the researched area (black rectangle) (modified after, Hofmann, T (ed.), 2007)

Sediments in the W of the fault were deposited during the Middle Miocene (Sarmatian and Pannonian age) and are successions of deltaic gravels with intercalations of shallow marine calcareous sands (Fig 2-3) (Sauer et al., 1992). Although the major fault surface is poorly exposed, the Sarmatian layers in the hanging wall are accessible for detailed structural analysis. The length of the faults ranges from several decimeters to several tens of meters, (and most faults record a marked displacement gradient.

Measured offset of marker layers along exposed faults ranges from centimeters up to several meters. Because there is a marked difference in the compositions of the layered sequences (e.g. well-sorted conglomerate consisting of coarse-grained pebbles alternating with fine-grained carbonate rich sands), the markers are easily identified on the hanging wall and footwall side of the faults.
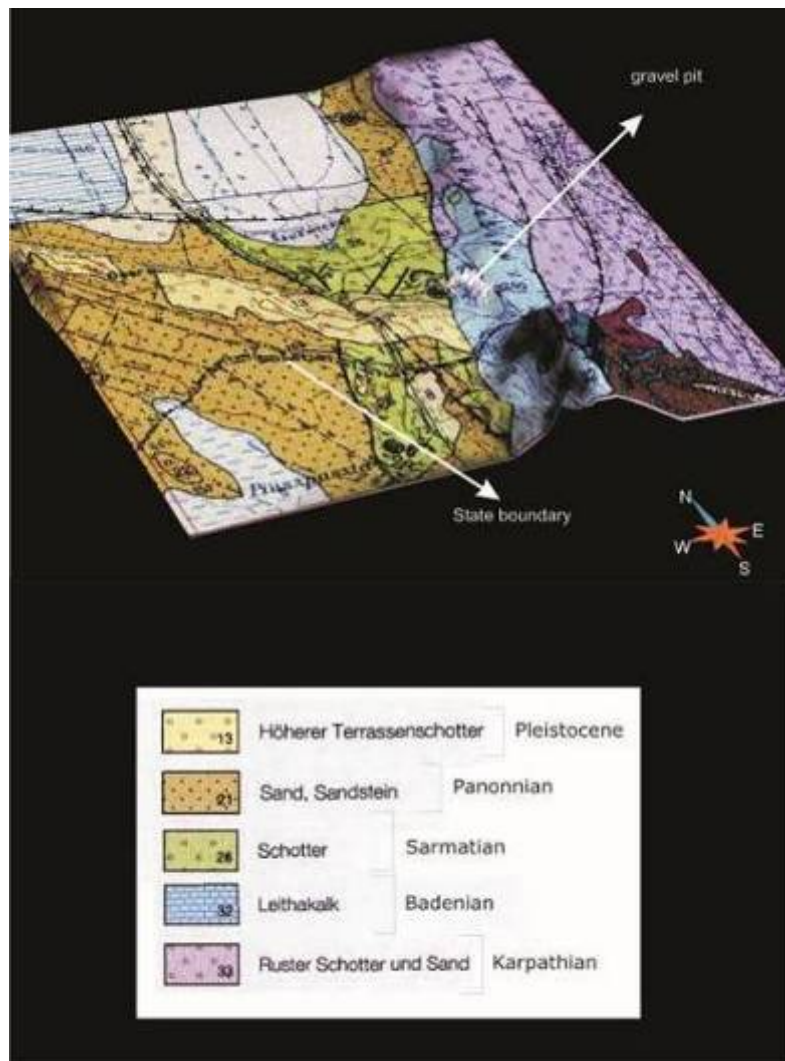
Fig 2-2. Digital Elevation Model of Geological map of Austria, sheet Rust, 1:50000 (Herman et al., 1991)

Fig 2-3. W-E striking outcrop wall in the gravel pit 5 km SSE of St. Margarethen, Burgenland. Photo looking towards N. The darker layer in the middle of the wall consists of coarse grained pebbles, which has been offset by numerous extensional faults mainly dipping towards W.

2.3 Ground Penetrating Radar (GPR) measurements

In order to extend the information of the two-dimensional exposure in the St. Margarethen gravel pit in the third dimension with the aim to construct a three-dimensional structural model, ground-penetrating radar measurements were carried out in numerous sections parallel and perpendicular to the outcrop wall using different transmitter antennas of 40 & 80MHz (Reiss et al., 2003; Sauer., 2004).

The GPR device consists of a plastic frame allowing the switch of antennas represented as four metal pistons. Between the unshielded antennas, the electromagnetic wave records measurements at the half distance between them. The distance along the recorded sections was measured with a tape, and as the instrument is not in direct contact with the ground marks must be made at regular intervals.

The optimal depth for geological subsurface interpretation with the 40 MHz GPR unshielded antenna is at 15-20 m, although the maximal recording depth of the device is down to 30 m, in comparison to only 9 m for a 80 MHz antenna.. The quality of the radargrams is mostly dependant on the noise level and the strata reflection energy. Another very important factor, which causes a high noise level, is a rugged topography, as the wobbling of the

antenna causes interference in subsurface reflections recording patterns. In order to locate the sections as accurate as possible, the geographical positions were recorded with a differential GPS device (Trimble GeoXH, with a horizontal accuracy of ca. 0.25 m).

The recorded radargrams were processed in Reflex (Sandmeier Scientific Software), which is software for seismic reflection/refraction and GPR processing and interpretation (see Chapter 2.1.3) for the 40MHz radargram processing steps). The processed radargrams were georeferenced using the recorded DGPS data in the three-dimensional visualization software Gocad (Earth Decision).

2.3.1 Processing steps of the 40 and 80 MHz GPR radagrams

The GPR sections were collected in a step mode with the MLF 40 and 80 MHz system. The data were sampled with a step size of 0.5m and 2.40m antennae spacing, marking every meter of along each section. The system includes operator with back-pack (console, portable computer and 12V battery) or remote cable extension.

Recorded radargram coulisse sections of a 40 and 80MHz data were processed in Reflex (Sandmeier Scientific Software), which is specialized software for seismic reflection/refraction and GPR data processing and interpretation. Used velocity (distance/travel time) for electromagnetic (EM) wave in this case was 0.12 m/ns, which is the speed of EM waves through dry sand (Baker et al., 2007). The processing steps in Reflex software used for the 40 MHz frequencies data are following:

- geometry corrections in Trace Interpolation/Resorting option (section length),

- 2D filter within Background removal applied to smooth each traces with one radargram section, bandpass frequencies 10-15-60-80, and

- 2D filter applied by average xy-Filter for 3 traces and 3 samples.

Similarly, 80 MHz radargrams have almost the same processing steps:

- geometry corrections in Trace Interpolation/Resorting option (section length),

- 2D filter within Background removal applied to smooth each traces with one radargram section, bandpass frequencies 40-60-110-150, and

- 2D filter applied by average xy-Filter for 3 traces and 3 samples.

2.4 <u>Structural 3D model in Gocad</u>

In order to interpret the sections and to construct a structural model, the two different frequencies the 40 MHz and 80 MHz radargrams, were compiled in Gocad.

The processed radargrams were imported into Gocad and converted from time to depth to attain a correct representation of the subsurface geometries. Mapping of distinct structural features was performed on each radargram. Reflectors which display a fairly continuous, rather flat pattern which is traceable over a certain distance was identified as sedimentary layering (Fig. 2-4). In contrast, fault surfaces cannot be directly identified in the GPR sections, but need to be inferred from the disruption of sedimentary layers. In this way, several sedimentary horizons and fault surfaces were mapped and compiled to 3D planes from several sections.

2.5 <u>Results and Discussion</u>

At the investigated outcrop, normal faults occur either as isolated segments, or as sets of high-angle faults dipping in the same direction, or

finally as conjugate fault sets. Displacement magnitude (from centimeters up to several meters) varies significantly between the different fault sets, but also along the individual fault traces. In the outcrop, these faults of confined length are associated with reverse drag of the adjacent sedimentary layers. As a result of the displacement gradient from the center towards the fault tips, and the close spacing of the individual faults, the layering is rotated between the faults (Exner and Grasemann, 2010).

A difference in the radargrams of the 40 and 80 MHz GPR frequencies is evident in Fig 2-4, as 40 MHz provide deeper but low-resolution radargrams and 80 MHz are shallow but high-resolution sections (Fig 2-4). The 80 MHz sections display some strata information about shallow distribution of layering (Fig 2-4, right), but larger faults unfortunately are not depicted.

After the GPR radargrams were processed, two types of structural features can be identified exclusively on the 40 MHz frequency: (i) partial imaging of fault traces (faults in fig 2-5) and (ii) tilting of sedimentary layers between these faults. In addition, the reflection of particular marker horizons and their offset along faults with offsets larger than 10 m can be clearly mapped from the radragram sections using line-based fault and horizon picking techniques.
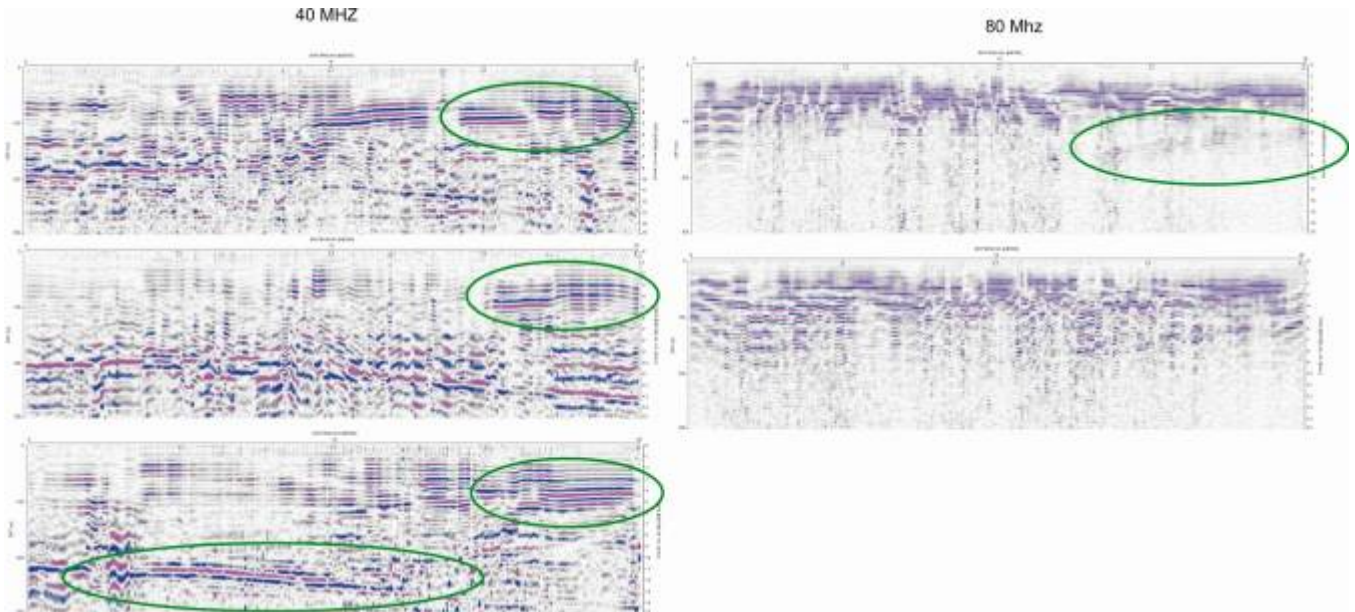
Fig 2-4. 40 (left) and 80MHz (right) radargrams with marked (green ellipse) geological features

Importantly, a combination of frequencies provided satisfactory resolution to exclude the hypothesis of a flat detachment directly below the exposed normal fault set.

2.6 <u>Conclusion</u>

A three-dimensional, shallow subsurface structural model of extensional faults in unconsolidated sediments was constructed applying different techniques: (i) GPR recording of coulisse sections, (ii) DGPS recording of the GPR sections, and (iii) field mapping of the outcrop. The three-dimensional structural model provides basic information of structural architecture behind the outcrop, recording no visible horizontal or subhorizointal surface that might represent a flattened section of a listric fault.
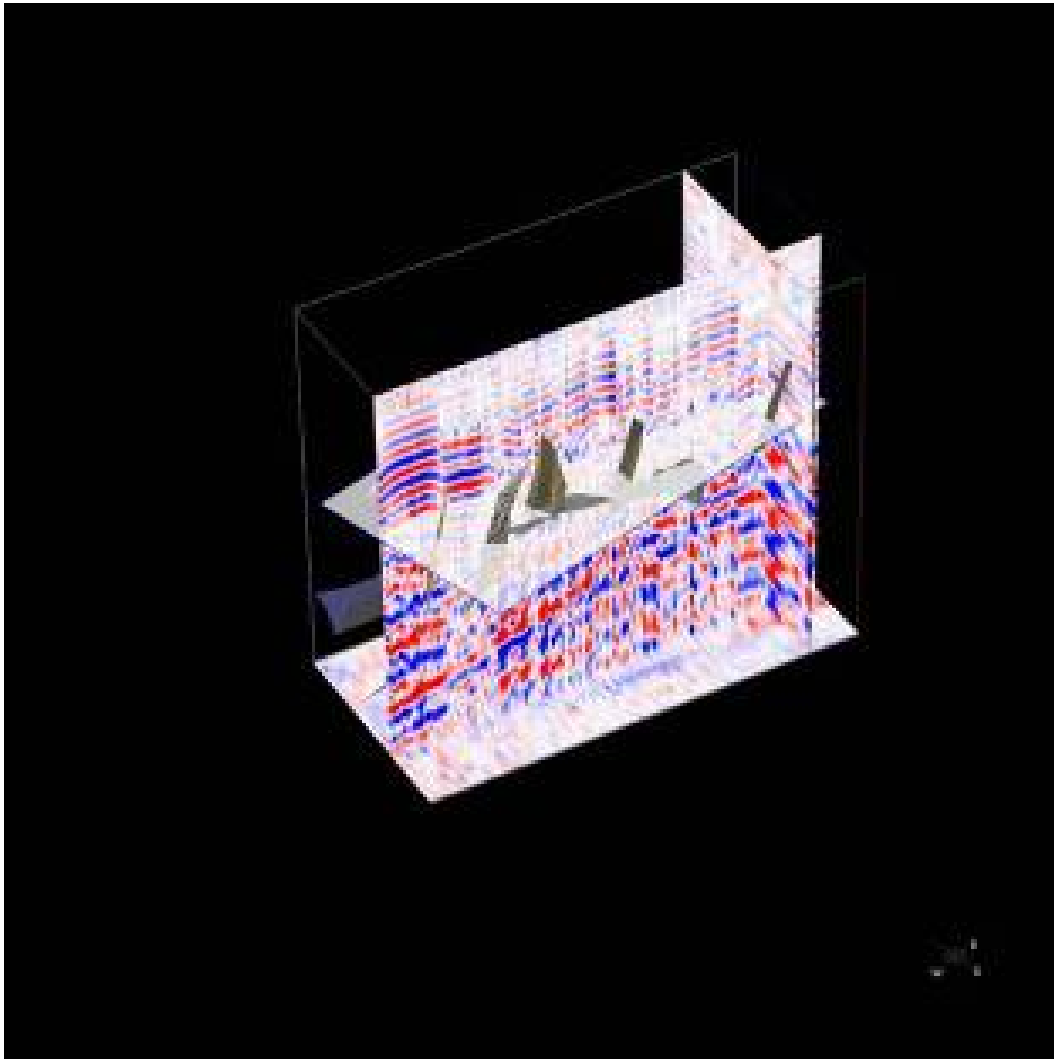
Fig 2-5. 3D model of a fault system. The colored surfaces are faults mapped behind the outcrop wall by using 40MHz GPR radargrams.

References

Baker, G. S., Jol HM, 2007. An introduction to ground penetrating radar (GPR). In: Bristow CS, Jol HM (eds) Ground penetrating Radar in sediments. Geol Soc Lond Spec Publ 211, pp 1-18.

Bristow, C. S., Jol HM, 2003. Ground Penetrating Radar in Sediments. Geol Soc London Spec Publ 211, 265.

Chwatal, W., Decker K, Roch K-H, 2005. Mapping active capable faults by high-resolution geo-physical mathods: examples from the central Vienna basin. Austrian J of Earth Sci 97, 52-59.

Daniels, D., 2004. Ground Penetrating Radar, 2nd Edition. pp 734.

Èkes, C., Hickin, E.J., 2001. Ground penetrating facies of the paraglacial Cheekye Fan, southwestern British Columbia, Canada. Sedim. Geol., 199-217.

Exner, U., Grasemann, B., 2010. Deformation bands in gravels: displacement gradients and heterogeneous strain. J of Geol Soc. 167; issue.5; p. 905-913.

Hermann, P., Pascher, G., Pistotnik, J. (1991): Geological map of Austria: Sheet 78-Rust, Geologischen Bundesanstalt, Wien.

Hofmann, T., 2007. Wien, Niederösterreich, Burgenland. Wanderungen in die Erdgeschichte. Dr. Fritz Pfeil, München 22, pp 167.

Meschede, M., Asprion, U. and Reicherter, K., 1997. Visualization of tectonic structures in shallow-depth high resolution ground-penetrating radar (GPR) profiles. Terra Nova 9, 167-170.

Reiss, S., Reicherter, K. R. and Reutner, C.-D., 2003. Visualization and characterization of active normal faults and associated sediments by high-resolution GPR. In: Bristow, C.S. & Jol, H.M (eds) Ground penetrating Radar in sediments. Geol.Soc., London, Spec Pub 211, 247-255.

Roberts, M. C., Niller, H.-P. and Helmstetter, N., 2003. Sedimentary architecture and radar facies of a fan delta, Cypress Creek, West Vancouver, British Columbia. In: Bristow, C.S. & Jol, H.M (eds) Ground penetrating Radar in sediments. Geol Soc London, Spec Pub 211, 111-126.

Sauer, D., Felix-Henningsen, P., 2004. Application of ground penetrating radar to determine the thickness of pleistocene periglacial slope deposits. J of Plant Nut Soil Sci 167, 752-760.

Sauer, R., Seifert, P., Wessely, G., Piller, W. E., Kleemann, E., Fodor, L., Hofmann, T., Mandl, G., Lobitzer, H., 1992. Guidebook to excursions in the Vienna Basin and the adjacent Alpine-Carpathian thrustbelt in Austria. Mitteil Österr Geol Gesselschaft 85, 1-264.

Serzu, M.H., Kozak, E.T., Lodha, G.S., Everitt, R.A., Woodcock, D.R. 2004. Use of borehole radar techniques tocharacterize fractured granitic bedrock at AECL's underground research laboratory. J. of App. Geophys. 137-150.

Ulriksen, C. P. F., 1982. Application of impulse radar to Civil Engineering. Ph.D. thesis Lund Univ of Techn , Lund, Sweden.

3. Listric versus planar normal fault geometry: an example from the Eisenstadt-Sopron Basin (E Austria)

Abstract

In a gravel pit at the eastern margin of the Eisenstadt-Sopron Basin, a satellite of Vienna Basin (Austria), Neogene sediments are exposed in the hanging wall of a major normal fault. The anticlinal structure and associated conjugated secondary normal faults were previously interpreted as a rollover anticline above a listric normal fault. The spatial orientation and distribution of sedimentary horizons and crosscutting faults was mapped in detail on a laser scan of the outcrop wall. Subsequently, in order to assess the 3D distribution and geometry of this fault system, a series of parallel ground penetrating radar (GPR) profiles were recorded behind the outcrop wall. Both outcrop and GPR data were compiled in a 3D structural model, providing the basis for a kinematic reconstruction of the fault plane using balanced cross section techniques. However, the kinematic reconstruction results in a geologically meaningless normal fault cutting down- and up-section. Additionally, no evidence for a weak layer serving as ductile detachment horizon (i.e. salt or clay horizon) can be identified in stratigraphic profiles. Instead, the observed deflection of stratigraphic horizons may be caused by a displacement gradient along a planar master fault, with a maximum displacement in the fault center, decreasing towards the fault tips. Accordingly, the observed deflection of markers in the hanging wall – and in a nearby location in the footwall of the normal fault – is interpreted as large scale fault drag along a planar fault that records a displacement gradient, instead of a rollover anticline related to a listric fault.

Keywords: Listric fault, fault drag, ground penetrating radar, balanced cross section

3.1 <u>Introduction</u>

Listric faults or shovel shaped faults (Suess 1909) are defined as curved normal faults in which the dip decreases with depth resulting in a concave upwards shape (e.g. Bally 1983; Shelton 1984). Two features are considered as characteristic of listric normal faults (Wernicke and Burchfiel 1982): (i) a steep upper part of the normal fault flattening downwards or merging with a low-angle detachment; and (ii) the down-warping or reverse drag (Hamblin 1965) of the hanging wall block forming a rollover anticline. Investigations of the origin of this widespread phenomenon that is very often used as a tool in hydrocarbon explorations (Tearpock and Bischke 2003 and references therein) are predominantly focused on the importance of fault shape. Broadly, two kinematic groups of rollover systems appear common: fault rollovers induced by extensional displacement along a listric fault shape and expulsion rollovers developed because of salt withdrawal (e.g. Ge et al. 1997; Krézsek et al. 2007; Brun and Mauduit 2008, 2009). Kinematic and geometric balancing techniques of extensional rollover anticlines provided reconstructions of the depth of an underlying detachment horizon (Chamberlin 1910; Wernicke and Burchfiel 1982; Tearpock and Bischke 2003). The understanding of the geometric evolution of listric fault systems was significantly improved by employing scaled analogue models (e.g. McClay 1990; McClay and Scott 1991; Xiao and Suppe 1992; Yamada and McClay 2003; Dooley et al. 2003) and more recently numerical models (Crook et al. 2006). Analogue models comprise a deformable hanging wall, composed of unconsolidated sand that is extended over a rigid footwall block (Yamada and McClay 2003). By employing rigid footwall blocks, the geometry of the master fault is predefined by the footwall block shape and remains fixed throughout the deformation history. However, some authors suggested that footwall deformation or collapse could be important

mechanisms during extension along listric faults (Gibson et al. 1989; Brun and Mauduit 2008; Krézsek et al. 2007), which are inherently neglected in analogue models or balancing techniques assuming a rigid footwall. Based on mechanical arguments, the common assumption that a hanging wall rollover anticline automatically implies a listric fault geometry (e.g. Shelton 1984; Yamada and McClay 2003) was questioned by several authors (e.g. Barnett et al. 1987; Mauduit and Brun 1998; Grasemann et al. 2005; Brun and Mauduit 2008). Alternatively, reverse drag of strata both in the hanging wall and in the footwall may develop around a planar fault surface, where the displacement decreases towards the fault tips (e.g. Barnett et al. 1987; Gupta and Scholz 1998; Mansfield and Cartwright 2000).

In this study we investigate a normal fault system in a southeastern satellite basin of the Vienna Basin (Austria), where tilting of sediments close to the fault was previously interpreted as a rollover anticline associated with a listric fault geometry (Decker and Peresson 1996). This paper focuses on the exposed hanging wall of the normal fault, comprising (1) field mapping supported by terrestrial laser scanning of the outcrop (2) GPR imaging of the deformed sediments and (3) geometric reconstruction of the fault geometry by coulisse cross section balancing. An integrated structural model is used to discuss the plausibility of a listric normal fault.

3.2 <u>Regional setting</u>

The Vienna Basin, located between the Alpine- and the Carpathian mountain belt, formed in the Miocene as a result of the lateral extrusion of the Eastern Alps (Royden 1985; Ratschbacher et al. 1991). Mostly SW-NE trending transtensive strike-slip and normal faults permitted the deposition of up to 5000 m of marine to lacustrine sediments in the center of the basin from the Carpathian fold belt and Pannonian basin (e.g. Fodor 1995). The multi-staged tectonic evolution started with a piggyback basin in the Lower Miocene positioned on the top of Alpine advancing thrust sheets (Wagreich,

2000), followed by a pull-apart stage in the Middle to Upper Miocene. After a Pannonian basin inversion phase, E-W extension lasted at least until the Pleistocene (Decker 1996) and is probably still active (Chwatal et al. 2005; Decker et al. 2005; Hinsch et al. 2005). The basin was extensively studied for hydrocarbon exploration (Wessely 1988; Strauss et al. 2006).

In the southeast, the Vienna Basin is connected to the Eisenstadt-Sopron Basin, which is a small satellite basin with 2000 m of sediment infill. The economically less important and thus less explored basin is bordered by normal faults (Fig. 3-1) and experienced its main subsidence phase in the Badenian (Schmid et al. 2001). The eastern margin of the basin is defined by the N-S trending Köhida normal fault system (Fodor 1995).
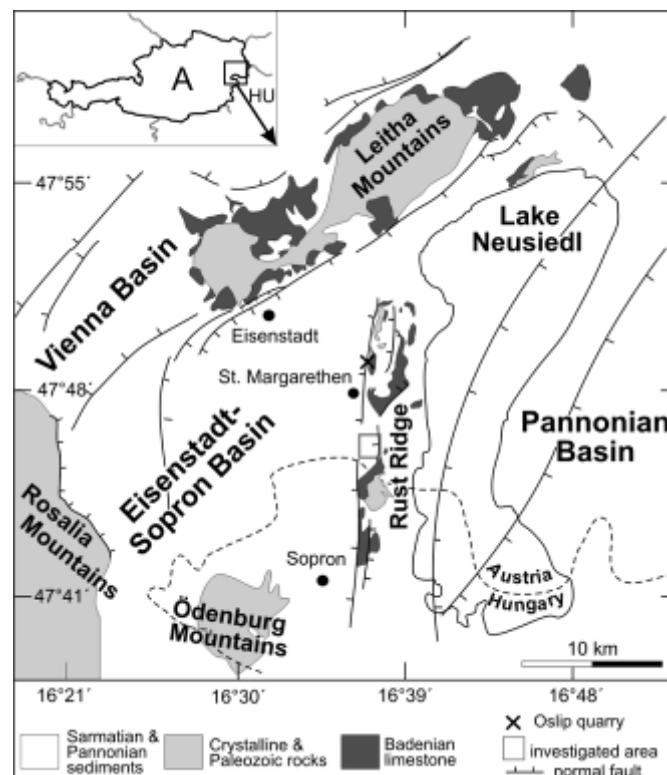
Fig.3-1 Tectonic sketch map of the Eisenstadt-Sopron Basin (eastern Austria).The investigated gravel pit is located on the eastern basin margin, 5 km south of the village St. Margarethen. A normal fault (referred to as master fault in the text) juxtaposes Badenian silts and limestone in the E with Sarmatian and Pannonian gravels and sands in the W (modified after Schmid et al. 2001)

The investigated outcrop (Fig. 3-2) is situated at the eastern margin of the Eisenstadt-Sopron basin, along a NNE –SSW striking normal fault, a part of the Köhida fault system, displacing Badenian calcareous silt in the East against a succession of Sarmatian and Pannonian gravels and calcareous sands in the West (Harzhauser and Kowalke 2002). In the southern part of the investigated area, both footwall and hanging wall sediments are covered by Pleistocene gravels, which post-date the activity of the normal fault. Approaching the fault plane, the hanging wall strata record an increase in dip angle from West to East, which was interpreted as rollover anticline associated with a listric normal fault by Decker and Peresson 1996.
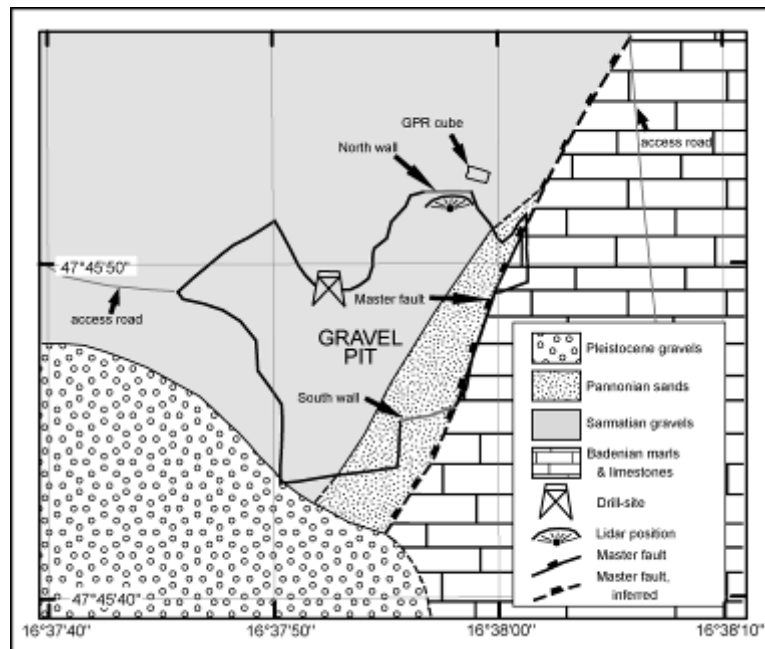
Fig. 3-2 Detailed map showing the investigated outcrop walls and GPR location in the gravel pit and the surrounding geology. The master fault juxtaposes Badenian marls and limestones in the E with Sarmatian and Pannonian gravels and sands

3.3 **Data acquisition, processing and results**

The investigated outcrop is located inside a gravel pit situated ca. 5km south of the village St. Margarethen, Burgenland, Austria (Fig. 3-1). A WNW-dipping normal fault (referred to as master fault in the following text) was mapped along the eastern margin of the pit (Decker and Peresson 1996). While the footwall of the master fault consisting of Badenian sediments is hardly exposed, the hanging wall comprising a sequence of middle Miocene (Sarmatian and Pannonian) gravels, silts and sands (Harzhauser and Kowalke 2002) can be studied in detail. The sedimentary beds are tilted up to ca. 35° towards the master fault, forming an anticlinal structure in the hanging wall of the master fault (Fig. 3-3a).
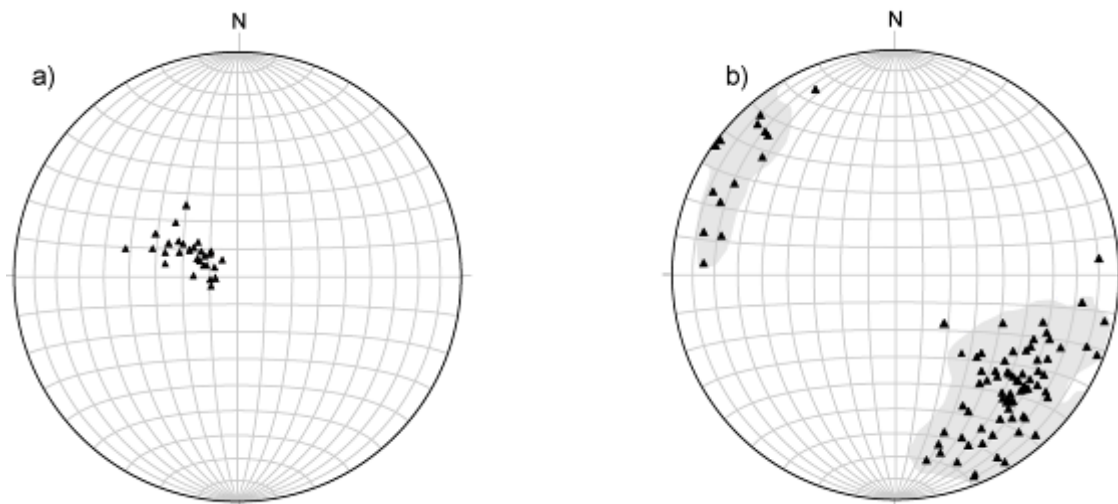
Fig. 3-3 Equal area projections, lower hemisphere: a poles to bedding planes (29) and b poles to fault planes (90), max. value: 16.2% at 311 / 62, contours at: 1.20 measured along the northern wall.

Additionally, several smaller normal faults with variable length and displacement, oriented subparallel and conjugate to the master fault, crosscut the sedimentary beds (Fig. 3-4b). In order to generate a 3D structural model and constrain the geometry and kinematics of the master fault, the following methods were applied: (i) detailed structural measurements of the sedimentary layers and the exposed faults, (ii) terrestrial laser scanning to obtain a high-resolution digital surface model

and georeferenced, rectified image of the outcrop wall, (iii) GPR survey behind the scanned wall to image the unexposed 3D geometry of the sedimentary beds and faults, and (iv) 2D section balancing to reconstruct the geometry of the proposed listric normal fault at depth. Combining these datasets, we generated a 3D structural model of the normal fault and the deformed hanging wall sediments.

3.3.1 Structural data

The investigated outcrop is located at the northeastern margin of the gravel pit, where a 10 m high and 30 m wide E-W oriented wall exposes the Sarmatian-Pannonian succession in the hanging wall of the master fault (Fig. 3-2).

We identified five characteristic marker units (M1-M5 in Fig. 3-4b) in the exposed section which were later used for correlation with horizons mapped in the GPR data.

Along the outcrop, the dip of the planar sedimentary layers increases gradually from W to E, with a dip towards the E of 8° in the W to a maximum of 34° in the E. This anticlinal structure was earlier interpreted as an expression of hanging wall collapse above a listric normal fault (Decker and Peresson 1996). In detail, the increase of dip is not only related to a gentle folding, but dip variations occur abruptly at secondary normal faults oriented parallel and at a conjugate angle to the master fault (Fig. 3-4b). Most of the observed faults are more accurately described as deformation bands (Exner and Grasemann, 2010), restricted to the lower gravel in M2 and displacing the sedimentary layering only some few centimeters.
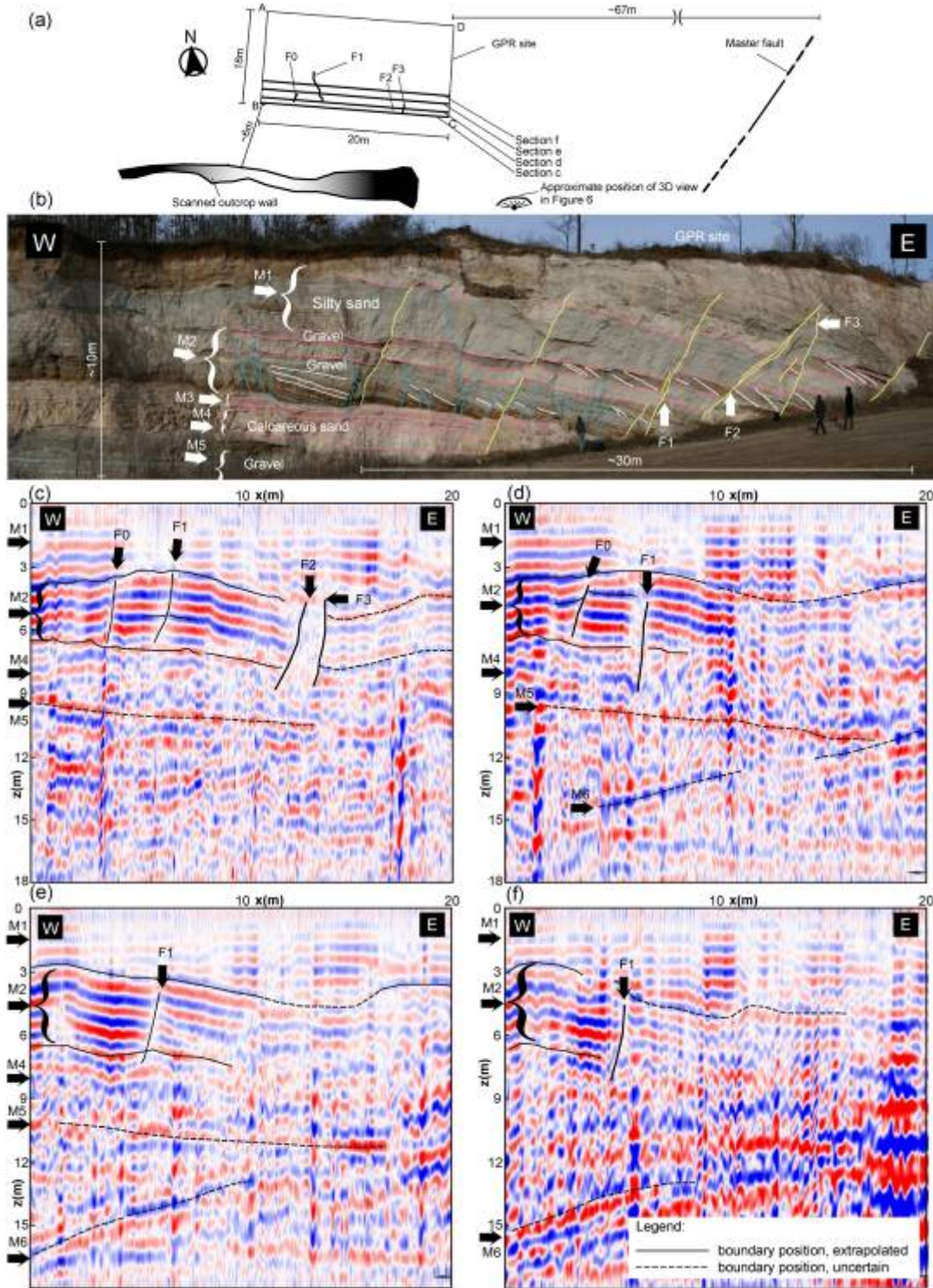
Fig.3- 4 a Map view of the investigated site, depicting the position of the scanned outcrop wall and the location of the GPR site; b Geological interpretation of the investigated wall, identifying the marker horizons (M1-M5), faults (marked in yellow) and deformation bands (blue); c-f GPR

sections N of and roughly parallel to the outcrop wall. Profile c is at ca. 6 m distance from the wall, the distance between the individual profiles is between 0.5 and 1.5 m as indicated in Fig. 3-4a. Variations in reflection intensity are interpreted as marker horizons, i.e. variation in lithological composition, most of which can be traced in all four sections. Subvertical offsets in the GPR signal can be correlated with larger fault structures; the fault F1 is observed in all sections, while the signals of F1 and F3 are lost further to the N.

These small faults record a displacement gradient from the center towards the tips, which promotes the development of reverse drag in the adjacent sedimentary layers (Hamblin 1965; Grasemann et al. 2005). Propagation and rotation of some faults lead to vertical coalescence and the generation of faults with larger offset up to a maximum of 4 m, crosscutting the entire exposed section. As all of the observed long faults cut across sedimentary horizons with a documented hiatus of several thousands of years (Harzhauser and Kowalke 2002), and no increase in thickness of the Sarmatian beds towards the master fault is documented, a synsedimentary generation of these faults can be ruled out.

Borehole data from a groundwater exploration drilling, located inside the gravel pit ca. 100 m SW of the outcrop wall (marked in Fig. 3-2), do not provide any indication of a possible detachment horizon, i.e. salt or silt, down to a depth of 20m below the exposed section. Instead, the succession of Sarmatian gravels and sands continues without any notable disturbances.

3.3.2 Ground Penetrating Radar

Ground penetrating radar (GPR) is commonly employed for detecting near surface geological features in sediments (e.g. Bristow and Jol 2003). Furthermore, several recent studies document the applicability of this method for the detection of faulted sedimentary horizons in the shallow subsurface. Meschede et al. (1997) observed the tectonic surfaces and rollover structures associated with faults in Middle Triassic limestone of SW Germany along 2-D profiles. The hanging wall of active faults was visualized

in the Betic Cordillera (Reiss et al. 2003) with high frequency antennas. To infer the active Markgrafneusiedel Fault in shallow Pleistocene deposits and to correlate it with the deeper fault levels of the Vienna Basin, 2-D GPR profiling was applied using both low and high frequencies (Chwatal et al. 2005).

A dense network of parallel GPR profiles provides the opportunity to image sedimentary horizons and faults in the prolongation along strike N of the exposed section. The investigated site was a 20 m x 19 m sized area (Fig. 3-4a). Though several antennae frequencies where applied and tested, we restrict the interpretation to the best results obtained with a center frequency of 40 MHz. The raw data are of moderate quality and gain significance by a simple but effective signal processing (background removal, bandpass filtering 15 to 80 MHz, weak smoothing). There is a low signal to noise ratio (S/N ratio) in the raw recordings. The reason for this remains unclear since disturbing surface features are absent and the soil was rather dry. However, strong reverberations suggest the presence of fluids. We interpret that although the extensive tree cover was recently removed, the still existing roots contain a relatively high amount of water.

Forty-one 40 MHz GPR sections were collected along 20 m long, E-W oriented lines with a relative spacing of 0.5 m. The sections are parallel to the exposed wall and perpendicular to the N-S striking faults. Assuming a propagation velocity of 0.12 m/ns (Bristow and Jol 2003), the signal penetration depth is approximately 15 m. The processed GPR sections were interpolated into a depth-converted cube such that sections with arbitrary directions can be visualized. Since the topography is rather flat and even, no topographic correction was applied.

Four representative GPR profiles striking parallel to the outcrop wall (Fig. 3-4a) are presented in Fig. 3-4,c-f. The strong reflections, located between 3 and 6 m below the surface, can be correlated with the M2 gravel horizons identified in the outcrop section. Below, the marker horizons M4,

M5 and M6 can be tentatively assigned to single high reflectors in the individual sections. Most reflectors slightly dip towards the E, or show an undulating geometry. Abrupt disturbances, representing a lack of energy in an otherwise continuous reflection band, are interpreted as faults. Some faults (e.g. F1) can be identified in several sections, thus providing additional constraints on their strike direction (Fig. 3-4a). The 40 MHz antenna did not depict smaller sized faults mapped in the outcrop, which have less than 3 m in length and correspondingly only some centimeters or decimeters of displacement. Finally, another strong reflector M6, which is not exposed at the nearby outcrop wall, was recorded in most 40 MHz GPR sections. This horizon, approximately 17 m below surface (and ~7 m below the base of the exposed wall) conspicuously dips in the opposite direction to the upper reflectors, i.e. 25° to the SW.

3.3.3 Laser scan and 3D model

We used a terrestrial laser scan (TLS) system (RIEGL LMS-Z420i), consisting of a high-performance long-range 3D laser scanner and a calibrated high-resolution digital camera mounted onto the scanner head, to generate a digital surface model and a rectified image of the investigated outcrop wall. The entire wall and the surroundings were scanned from a single point, which was recorded using a Differential Global Positioning System receiver (DGPS). The point-cloud of xyz-coordinates acquired by TLS was imported into Gocad, a three-dimensional visualization software, and the points corresponding to the outcrop wall were meshed to form a virtual outcrop surface, onto which the rectified image was draped (McCaffrey et al. 2005). By integrating the measurements of the respective bedding and fault planes, a 3D structural model of the outcrop data was generated (Fig. 3-5), taking account of the exact location and orientation of the structural features. To compare the structural measurements collected at the outcrop wall with the GPR imaging results, we integrated both datasets into the 3D model, providing the framework for the further structural interpretation.

Apart from digitizing numerous faults along the outcrop wall, three distinctive fault surfaces were additionally mapped in the GPR dataset. Although the outcrop wall is located at a rather large distance (ca. 6 m) from the closest GPR section, we were able to connect the fault traces from the GPR sections with three of the larger faults in the outcrop and construct strike and dip of the fault planes. Similarly, the well traceable marker horizons M2 and M6 were connected to horizon surfaces in the structural model (Fig 3-5).
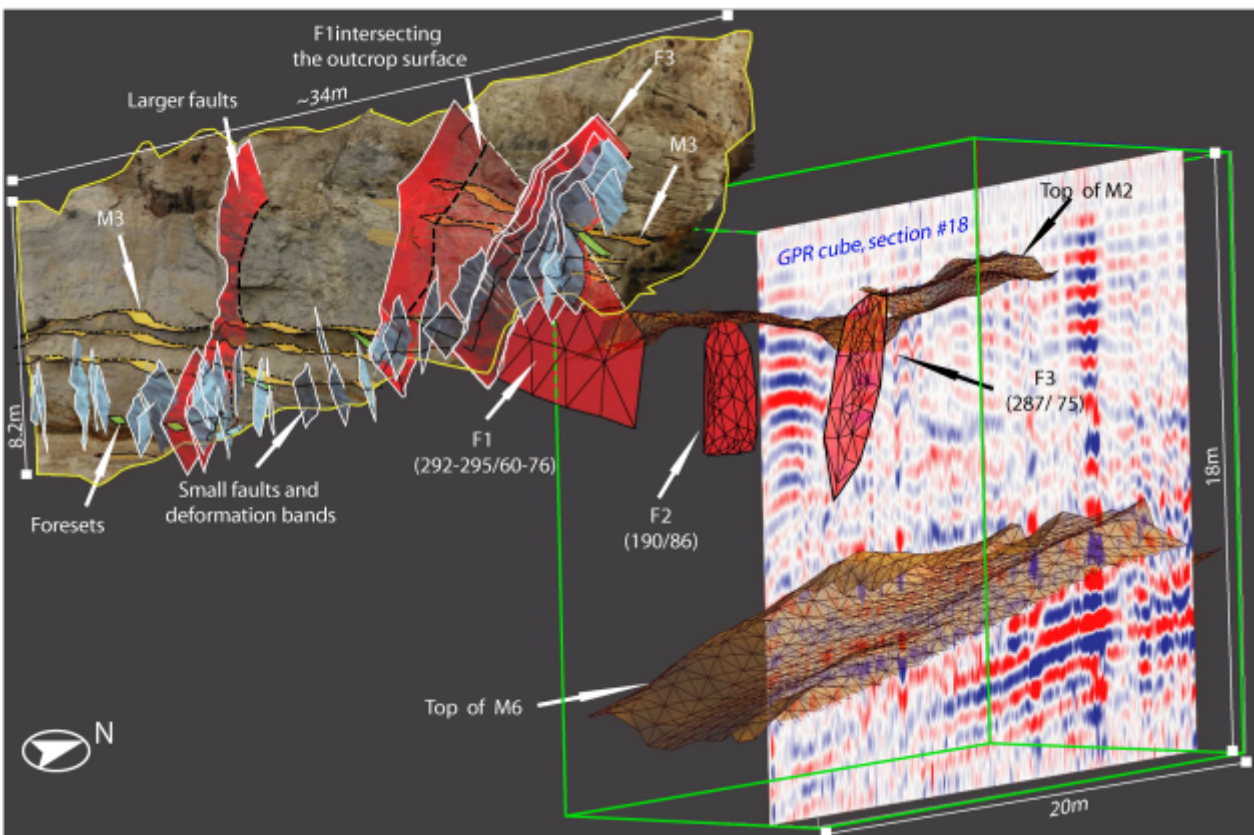
Fig. 3-5 3D structural model constructed from the rectified outcrop image draped on terrestrial laser scan (TLS) data and the ground penetrating radar (GPR) cube (in the background). No vertical exaggeration. The exposed fault and horizon surfaces are constructed in great detail, accurately respecting the dip and dip direction of each element. Selected fault and horizon surfaces mapped from GPR data are connected to the outcrop structures (e.g. F1).

3.4 Depth to detachment construction assuming a listric fault geometry

A great number of geometrical reconstructions of extensional faults has been proposed and discussed by several authors (e.g. Davison 1986; Williams and Vann 1987; White 1992; Yamada and McClay 2003). Most of these models are based on the geometric relationships between the hanging wall structures and the underlying detachment using vertical, oblique or flexural slip restoration assuming either conservation of the area/bed-length on a cross-section and/or constant slip along the fault (for a discussion of models with area change and slip gradients see Wheeler 1987). All these models have in common that sediments in the hanging wall above a rigid fault surface with a listic geometry deform into a rollover anticline, while the footwall remains undeformed (Tearpock and Bischke 2003 and references therein). Comparing different reconstruction techniques with a positive inversion analogue experiment, Yamada and McClay (2003) suggested that the inclined simple shear model most accurately approximates the restoration of the hanging wall deformation. This technique assumes that deformation of the hanging wall occurs by simple shear along inclined slip planes, which are either parallel to syn- or antithetic faults (White et al. 1986; Dula 1991). The shear angle of these faults is frequently estimated using the Mohr-Coulomb Theory resulting in dip angles between 60°-70° (Tearpock and Bischke 2003). In order to reconstruct the master fault geometry from a hanging wall rollover anticline, the heave of a marker horizon must be known. The bed thicknesses along the shear planes remain fixed and therefore this technique always results in a hanging wall area-balanced reconstruction. Practically, the marker horizon is divided into domains of constant dip and the amount of displacement between the dip domains is defined by the distance along the plane between the reconstructed and the deformed geometry of the marker horizon.

Being aware of the limitations of geometrical reconstructions, we used the inclined simple shear model in order to reconstruct the depth of the detachment, assuming that a rigid listric fault forced the deformation of the marker horizon M3 of the northern and southern pit walls in St. Margarethen (Fig. 3-2). The most sensitive parameter, which strongly influences the location and the orientation of the detachment, is actually the spatial position constrained by the widths and orientations of the dip-domains with respect to the orientation of the fault plane containing the hanging wall cutoff of the marker horizon. Therefore, the dip domains were constructed as accurately as possible using the 3D structural model including the exposed sections of M3 as well as its spatial orientation in the subsurface. According to the mean of the measured fault planes in the hanging wall (Fig. 3-3b), the dip of the inclined shear planes is 72°. The fault plane containing the hanging wall cut-off of the marker horizon M3 dips 60° towards WNW. Our depth-to-detachment calculations of both the northern and southern pit walls in St. Margarethen gave almost identical but geologically meaningless results, because the constructed detachments do not flatten at depth but have an U-shaped geometry (Fig. 3-6). The construction of the domain closest to the observed master fault results in a plausible initial flattening of the detachment segment in the next domain. However, the constructed detachment segments of all other domains record continuous steepening and dip in the opposite direction than the steep part of the exposed fault at the surface (i.e. towards ESE) resulting in the geologically meaningless U-shape fault geometry. We therefore conclude that the assumption of a rigid listric fault plane for the normal fault in St. Margarethen might be incorrect and other mechanisms were responsible for forming a hanging wall anticline.
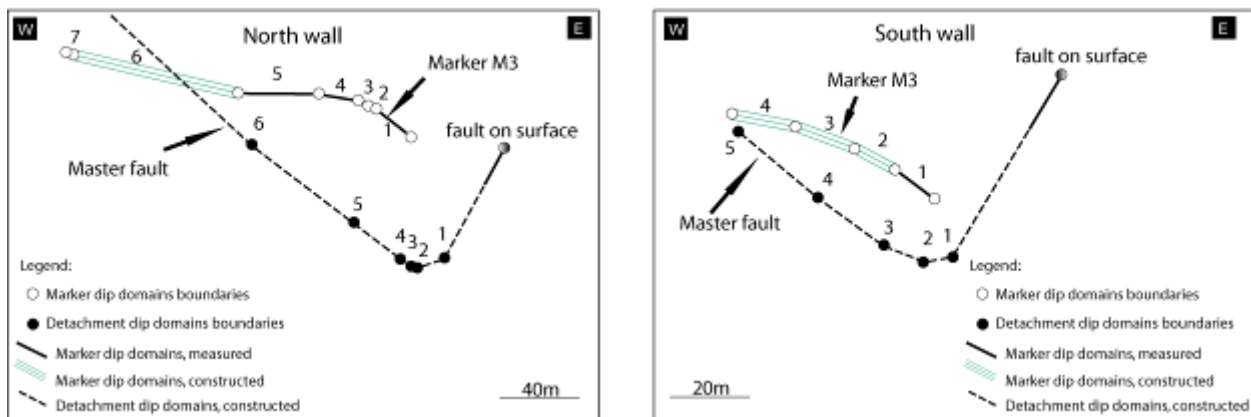
Fig. 3-6 Balanced cross sections, a north wall and b south wall, using a dip domain technique in order to reconstruct the continuation of a listric fault at depth (Tearpock and Bischke, 2003). We omitted a full-scale graphical reconstruction in order to avoid an abundance of auxiliary lines. The input parameters into the models are (i) the spatial orientation of the marker bed M3 and (ii) the true dip of the master fault at the hanging wall cutoff level. Both reconstructed sections do not result in a listric fault with a sub-horizontal detachment at depth but in geologically meaningless structure.

3.5 Discussion

3.5.1 Listric versus planar fault geometry

Since both concepts of fault related deformation, i.e. a rollover anticline above a listric fault as well as reverse drag in the hanging wall of a planar fault, result in similar finite geometries, their respective applicability to the studied outcrop is discussed in the following section. Importantly, this study is restricted to mechanical models of anticlines related to normal faults, and does not consider hanging wall anticlines occurring along inverted normal faults related to a compressional reactivation with thrust kinematics (e.g. McClay, 1995).

Balancing techniques of listric faults are based on the concept of the displacement of the hanging wall along a curved fault surface, separating the deformable sedimentary pile in the hanging wall from an undeformable footwall (Fig. 3-7a). In these models, the shape of the fault largely controls the deformed geometry of the hanging wall. The success of the model of listric faults is largely based on the highly intuitive results of sandbox models (e.g. McClay 1990; McClay and Scott 1991), which result in geometries directly comparable to interpreted extensional faults from seismic sections (e.g. Bally 1983; Butler 2009). Since listric faults and associated hanging wall anticlines are common targets for hydrocarbon exploration, the balancing methods like the technique applied in this study have been widely used in order to support seismic interpretations (e.g. Gibbs 1984; Williams and Vann 1987). In order to increase the fit between observations and models, numerous modifications of the model and the balancing technique have been suggested (for a review see Tearpock and Bischke 2003; Yamada and McClay 2003), some of which even imply deformation of the footwall (e.g. Koyi and Skelton 2001; Imber et al. 2003; Kré́szek et al. 2007). Our simple restoration of the extensional fault in St. Margarethen does not result in a geologically plausible subhorizontal lower part of a listric fault. The applied method is based on the assumptions of listric fault models but the constructed results are geologically meaningless and therefore we conclude that extension and hanging wall deformation were controlled by a different mechanical process.

A completely different group of models explain rollover structures (Fig. 3-7b), also referred to as reverse drag (Hamblin 1965), by displacement gradients along the fault (e.g. Barnett et al. 1987; Watterson et al. 1998). These models account for the frequent observation that a fault of finite length records lateral and vertical variations in displacement magnitude (e.g. Mansfield and Cartwright, 2000). Such a displacement gradient induces wall-rock strains eventually leading to a bending, i.e. reverse drag, of markers at a high angle to the fault plane (Grasemann et al. 2005).

65
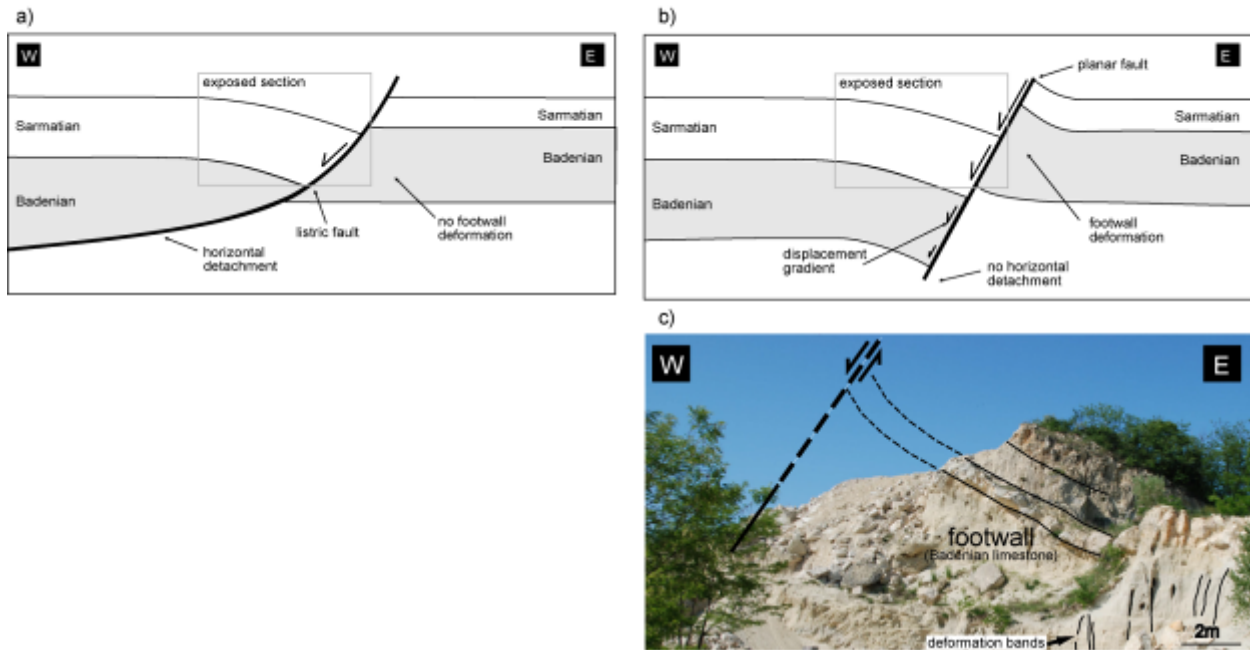
Fig. 3-7 Generalized cross sections comparing the two conceptual models. a Listric fault model with constant displacement along a fault, which flattens at depth into a sub-horizontal detachment. The hanging wall is deformed into a rollover anticline but there is no deformation within the footwall. b Model of a planar fault of finite length recording a displacement gradient. Fault movement induced perturbation strain which causes reverse drag in the hanging wall and in the footwall. The exposed section in St. Margareten record nearly identical geometry that characterizes the both models. c Outcrop picture of the Oslip quarry (location marked in Fig. 3-1) in a footwall position along the N-S trending fault system, exposing Badenian limestone and sand layers dipping to the E with ca. 40°, which is interpreted as reverse drag and associated deformation bands in the footwall of the normal fault.

The faults in these models are planar and not listric, and even slip gradients along "anti-listric" faults may often result in reverse drag (Reches and Eidelman 1995). If such a displacement gradient model is applied to the studied outcrop in St. Margarethen, the reverse drag observed in the hanging wall Sarmatian sediments may alternatively be explained by a slip gradient along a planar master fault. The deformation in the Sarmatian sediments is accommodated by secondary faults and deformation bands of finite length, which themselves record a displacement gradient and associated smaller scaled reverse drag (Exner and Grasemann 2010).

Because the master fault exposed in the gravel pit of St. Margarethen cannot be traced further to the S across the Austrian-Hungarian border, where there is no evidence of extension in the Sarmatian/Pannonian sediments, a slip gradient on the master faults is geologically highly plausible. Displacement gradient as the primary mechanism for the drag in the Sarmatian sediments is furthermore supported by the GPR data and the integrated 3D structural model (Fig. 3-5), which show that the magnitude of the drag of marker horizons is changing along the strike of the master fault. Although the displacement gradient models predict fault drag in the hanging and the footwall, the magnitude and sense is strongly dependent on the exposed part of the fault and theoretically can juxtapose reverse drag in the hanging wall with normal or no drag in the footwall (Barnett et al. 1987; Grasemann et al. 2005). Unfortunately, the footwall in the quarry in St. Margarethen is not exposed. However, in direct continuation along the strike of the normal fault system to the N (Fig. 3-1, quarry Oslip), the Badenian sediments in the footwall of the master fault are strongly deformed by the formation of deformation bands and record a dip of 30° towards the W (Fig. 3-7c). We interpret that this tilt of the Badenian sediments below the master fault represents the footwall reverse drag. Based on the regional geological map, the dip variations of the Badenian sediments are clearly related to the faulting and therefore favour models which predict footwall deformation.

3.5.2 Hydrocarbon traps

The occurrence of hydrocarbon-trapping listric fault systems has been of great interest for oil and gas exploration around the world (e.g. Dula 1991; Nunns 1991; Withjack et al. 1995; Desheng 1996; Rowan et al. 1998; Bhattaracharya and Davies 2001; Dutton et al. 2004). Rollover anticlines are the least risky traps for petroleum depending on the juxtaposition of a shale seal across the fault plane (Allen and Allen 2005). The fault plane itself may or may not seal, allowing either lateral or vertical migration to higher structural levels (Weber 1978). However, detailed subsurface mapping of

listric faults frequently extends below the level of coherent seismic data decreasing the reliability of interpretation. Furthermore, it has been shown that flattening normal faults are disappearing in the seismic data with increasing depth ("downwards dying growth faults", e.g. Tearpock and Bischke 2003). Consequently, refined balanced cross section techniques (see recent review by Poblet and Bulnes, 2005), analogue (e.g. Vendeville and Cobbold 1988; Gaullier et al. 1993; Mauduit and Brun 1998), and numerical (Erickson et al. 2001 and references cited therein) models have been used in order to aid seismic interpretations. Especially mechanical models introducing interaction between a newly formed steep normal fault and a pre-existing ductile low-angle detachment layer, have increased the knowledge about plausible rheological and geometrical settings for normal faults, which flatten at depth. However, it is important to note that a large number of models which introduce ductile layers are strictly speaking not listric faults sensu strictu but can be better explained by a raft tectonic model, which is based on mechanical instabilities (Mauduit et al. 1997).

Here we argue that planar faults recording a displacement gradient may result in similar geometries as listric faults with rollover anticlines. This model is especially attractive, where (i) the fault records a high-angle relationship with the marker layers, (ii) the fault cuts rocks of similar material behaviour in the hanging wall and in the footwall, (iii) the fault has a finite length and records a displacement gradient and (iv) no ductile layer (e.g. salt) is present at depth. An exceptional illustrative example has been investigated by a detailed 3D seismic interpretation of extensional faults in the Leona field in the Eastern Venezuela Basin (Porras et al. 2003). In this interpretation, the major oil accumulations are confined to seals forming normal and reverse drag folds along faults with displacement gradients. Normal-drag folds form the largest traps, with extended reservoirs in the footwall of master normal faults, whereas reverse-drag folds provide the structural closure for trapping in the hanging wall.

3.6 <u>Conclusions</u>

We created a 3D structural model of deformed Sarmatian and Pannonian Sediments in the hanging wall of a normal fault bordering the eastern margin of the Eisenstadt-Sopron Basin. Spatial field measurements of faults and sedimentary layering, a terrestrial laser scan of an outcrop wall and GPR data behind the outcrop wall were integrated into the structural model. The dip of the sediments increases towards the west-dipping master fault resembling a rollover structure above a listric normal fault. However, balanced cross sections based on standard dip domain techniques used for construction of listric faults do not result in geologically plausible structures. Considering the absence of a ductile horizontal layer at depth and the fact that the master fault terminates along strike towards the S, we argue that the observed reverse drag in the sediments is related to a slip gradient along a planar normal fault of finite length.

References

Allen PA, Allen JR (2005) Basin Analysis: Principles and Applications. Wiley-Blackwell. pp 560

Bally AW (1983) Seismic expression of structural styles. A picture and work atlas (3 vols). Am Ass Petrol Geol Stud Geol 15

Barnett JAM, Mortimer J, Rippon JH, Walsh JJ, Watterson J (1987) Displacement Geometry in the Volume Containing a Single Normal Fault. Am Assoc Petr Geol B 71:925-937

Bhattacharaya, JP, Davies, RK, 2001. Growth faults at the prodelta to delta-front transition, Cretaceous Ferro sandstone, Utah. Mar Petrol Geol 18: 525-534.

Bristow CS, Jol HM (2003) An introduction to ground penetrating radar (GPR) in sediments. In Bristow CS, Jol HM (eds). Ground Penetrating Radar in Sediments. Geol Soc Lond Spec Publ 211:1-7

Brun JP, Mauduit TP-O (2008) Rollover in salt tectonics: The inadequacy of the listric fault model. Tectonophysics 457:1-11

Brun JP, Mauduit TP-O (2009) Salt rollers: Structure and kinematics from analogue modelling. Mar Petrol Geol 26:249-258

Butler, R (2009) Apulian foreland, offshore SE Italy. Virt Seis Atl

Chamberlin RT (1910) The Appalachian folds of central Pennsylvania. J Geol 18:228-251

Chwatal W, Decker K, Roch K-H (2005) Mapping active capable faults by high-resolution geo-physical mathods: examples from the central Vienna basin. Austrian J Earth Sci 97:52-59

Crook AJL, Wilson SM, Yu JG, Owen DRJ (2006) Predictive modeling of structure evolution in sandbox experiments. J Struct Geol 28:729-744

Davison I (1986) Listric normal fault profiles: calculation using bed-length balance and fault displacement. J Struct Geol 8:209-210

Decker K (1996) Miocene tectonics at the Alpine-Carpathian junction and the evolution of the Vienna Basin. Mitt Ges Geol Bergbaustud Österr 41:33-44

Decker K, Peresson H (1996) Rollover and hanging-wall collapse during Sarmatian/Pannonian synsedimentary extension in the Eisenstadt Basin. Mitt Ges Geol Bergbaustud Österr 41:45-52

Decker K, Peresson H, Hinsch R (2005) Active tectonics and Quaternary basin formation along the Vienna Basin Transform fault. Quat Sci Rev 24:305-320

Desheng L (1996) Basic characteristics of oil and gas basins in China. J Southe Asian Earth 13:299-304

Dooley T, McClay K, Pascoe R (2003) 3D analogue models of variable displacement extensional faults: application to Revfallet Fault system off shore mid Norway. In Nieuwland, D A (ed) New Insights into Structural Interpretation and Modelling. Geol Soc Lond Spec Publ 212:151-167

Dula WF (1991) Geometric models of listric normal faults and rollover folds. Am Assoc Petr Geol B 75:1609-1625

Dutton DM., Lister D, Trudgill BD, Pedro K, (2004) Three-dimensional geometry and displacement configuration of a fault array from a raft system, Lower Congo, Offshore Angola: Implications for the Neogene turbidite play. In: Davies RJ, Cartwright JA, Stewar SA, Lappin M, Underhill JR. (ed) 3D seismic technology: Application to the exploration of sedimentary basins. Geol Soc Lond Mem 29: 133-142.

Erickson SG, Strayer LM, Suppe J (2001) Mechanics of extension and inversion in the hanging walls of listric normal faults. J Geophys Res 106:26655-26670

Exner U, Grasemann B (2010) Displacement gradients and heterogeneous strain along deformation bands in gravels. J Geol Soc London

Fodor L (1995) From transpression to transtension: Oligocene-Miocene structural evolution of the Vienna Basin and the East Alpine-Western Carpathian junction. Tectonophysics 242:151-182

Gaullier V, Brun JP, Guérin G, Lecanu H (1993) Raft tectonics: the effects of residual topography below a salt décollement. Tectonophysics 228:363-381

Ge H, Jackson PAM, Vendeville B (1997) Kinematics and Dynamics of Salt Tectonics driven by Progradation. Am Assoc Petr Geol B 81:398-423

Gibbs AD (1984) Structural evolution of extensional basin margins. J Geol Soc London 141:609-620

Gibson JR, Walsh JJ and Watterson J (1989) Modelling of bed contours and cross-sections adjacent to planar normal faults. J Struct Geol 11:317-328

Grasemann B, Martel S, Passchier CW (2005) Reverse and normal drag along a fault. J Struct Geol 27:999-1010

Gupta A, Scholz CH (1998) A model of normal fault interaction based on observations and theory. J Struct Geol 22:865-879

Hamblin WK (1965) Origin of "reverse drag" on the down-thrown side of normal faults. Geol Soc Am Bull 76: 1145-1164.

Harzhauser M, Kowalke T (2002) Sarmatian (Late Middle Miocene) Gastropod Assemblages of the Central Paratethys. Facies 46:57-82

Hinsch R, Decker K, Wagreich M (2005) 3-D mapping of segmented active faults in the southern Vienna Basin. Quat Sci Rev 24:321-336

Imber J, Childs C, Nell PAR, Walsh JJ, Hodgetts D, Flint S (2003) Hanging wall fault kinematics and footwall collapse in listric growth fault systems. J Struct Geol 25:197-208

Koyi HA, Skelton A (2001) Centrifuge modelling of the evolution of low-angle detachment faults from high -angle normal faults. J Struct Geol 23:1179-1185

Krézsek C, Adam J, Grujic D (2007) Mechanics of fault and expulsion rollover systems developed on passive margins detached on salt: insights from analogue modelling and optical strain monitoring. In: Jolley, SJ, Barr, D, Walsh, JJ, Knipe, RJ (eds) Structurally Complex Reservoirs. Geol Soc Lond Spec Publ 292:103-121

Mansfield CS, Cartwright JA (2000) Stratal fold patterns adjacent to normal faults: observations from the Gulf of Mexico. In: Cosgrove J W, Ameen MS (eds) Forced Folds and Fractures. Geol Soc Lond Spec Publ 169:115-128

Mauduit T, Brun JP (1998) Development of growth fault/rollover systems: Birth, growth, and decay. J Geophys Res 103:18119-18136

McCaffrey KJW, Jones RR, Holdsworth RE, Wilson RW, Clegg P, Imber J, Holliman N, Trinks I (2005) Unlocking the spatial dimension: digital technologies and the future of geoscience fieldwork. J Geol Soc London 162 :927-938

McClay KR (1990) Extensional fault systems in sedimentary basins: a review of analogue model studies. Mar Petrol Geol 7:206–233

McClay KR (1995) The geometries and kinematics of inverted fault systems; a review of analogue model studies. In Buchanan JG and Buchanan PG (eds) Basin inversion. Geol Soc Lond Spec Publ 88:97-118

McClay KR, Scott AD (1991) Experimental models of hanging wall deformation in ramp-flat listric extensional fault systems. Tectonophysics 188:85-96

Meschede M, Asprion U, Reicherter K (1997) Visualization of tectonic structures in shallow-depth high resolution ground-penetrating radar (GPR) profiles. Terra Nova 9:167-170

Nunns AG (1991) Structural restoration of seismic and geologic sections in extensional regimes. Am Assoc Petr Geol B 75:278-297

Poblet JBM, Bulnes M (2005) Fault slip, bed-length and area variations in experimental rollover anticlines over listrc normal faults: influence in extension and depth to detachment estimations. Tectonophysics 396:97-117

Porras JS, Vallejo EL, Marchal D, Selva C (2003) Extensional Folding in the Eastern Venezuela Basin: Examples from Fields of Oritupano-Leona Block. Search and Discovery Article #50003:7

Ratschbacher L, Frisch W, Linzer H-G, Merle O (1991) Lateral extrusion in the Eastern Alps: 2, Structural analysis. Tectonics 10:257-271

Reches Z, Eidelman A (1995) Drag along faults. Tectonophysics 247:145-156

Reiss S, Reicherter KR, Reutner C-D (2003) Visualization and characterization of active normal faults and associated sediments by high-resolution GPR. In: Bristow CS, Jol HM (eds) Ground Penetrating Radar in Sediments. Geol Soc Lond Spec Publ 211:247-255

Rowan MG, Hart BS, Nelson S, Flemings PB, Trudgill BD, (1998) Three-dimensional geometry and evolution of salt related growth-fault array: Eudene Island 330 field, offshore Louisiana, Gulf of Mexico. Mar Petrol Geol 15: 309-328.

Royden LH (1985) The Vienna Basin: A thin-skinned pull-apart basin. In: Strike-slip deformation, basin formation, and sedimentation (ed Biddle K T, Christie-Blick N). SEPM Spec Pub 37:319-338

Schmid HP, Harzhauser M, Kroh A (2001) Hypoxic Events on a Middle Miocene Carbonate Platform of the Central Paratethys (Austria, Badenian, 14 Ma). Ann Naturhist Mus Wien 102A:1-50

Shelton W J (1984) Listric normal faults, an illustrated summary. Am Assoc Petrol Geol Bull 68:801-815

Strauss P, Harzhauser M, Hinsch R, Wagreich M (2006) Sequence stratigraphy in a classic pull-apart basin (Neogene, Vienna Basin). A 3D seismic based integrated approach. Geol Carpath 57:185-197

Suess E (1909) Das Antlitz der Erde. Tempsky F, Freitag G, Prag and Wien, Leipzig.

Tearpock DJ, Bischke RE (2003) Applied Subsurface Geological Mapping. pp 821

Vendeville B, Cobbold PR (1988) How normal faulting and sedimentation interact to produce listric fault profiles and stratigraphic wedges. J Struct Geol 10:649-659

Wagreich M (1990) A slope-apron succession filling a piggyback basin the Tannheim and Losenstein Formations (Aptian – Cenomanian) of the eastern part of ther North Calcareous Alps (Austria). Mitt Österr Geol Ges 93:31-54

Watterson J, Nicol A, Walsh JJ (1998) Strains at the synchronous conjugate normal faults. J Struct Geol 20:363-370

Weber KJ (1978) Hydrocarbon distribution patterns in Nigerian growth fault structures controlled by structural style and stratigraphy. J Petrol Sci Eng 1:91-104

Wernicke B, Burchfiel BC (1982) Modes of extensional tectonics. J Struct Geol 4:105-115

Wessely G (1988) Structure and development of the Vienna basin in Austria. In: Royden LH, Horváth F (eds). Am Assoc Petr Geol B 45:333–346

Wheeler J (1987) Variable-heave models of deformation above listric normal faults: the importance of area conservation. J Struct Geol 9:1047-1049

White N (1992) A Method for Automatically Determining Normal Fault Geometry at Depth, J Geophys Res 97:1715-1733

White NJ, Jackson JA, McKenzie DP (1986) The relationship between the geometry of normal faults and that of the sedimentary layers in their hanging walls. J Struct Geol 8:897-909

Williams G, Vann I (1987) The geometry of listric normal faults and deformation in their hanging walls. J Struct Geol 9:789-795

Withjack MO, Islam QT, La Pointe PR (1995) Normal faults and their hanging-wall deformation; an experimental study. Am Assoc Petr Geol B 79:1-18

Xiao H, Suppe J (1992) Origin of Rollover. Am Assoc Petrol Geol Bull 76:509-529

Yamada Y, McClay K (2003) Application of geometric models to inverted listric fault systems in sandbox experiments. Paper 1: 2D hanging wall deformation and section restoration. J Struct Geol 25:1551-1560

4. Identifying fault segments from 3D fault drag analysis

Abstract

The influence of segmented fault growth in Miocene sediments of the central Vienna Basin is demonstrated by a combination of three-dimensional geometric and kinematic parameters. In detail, we investigate marker horizons in the hanging wall and footwall of with the highly irregular Markgrafneusiedl normal fault surface from 3D seismic data. In addition to conventional fault analysis, e.g. orientation, displacement and curvature, we focus our study on the occurrence of normal and reverse drag of marker horizons, predominately in the hanging wall. By analyzing the relationship between fault surface geometry and fault drag within the marker horizons we are able to identify individual fault segments and constrain several stages of progressive fault evolution. By a detailed analysis of fault drag, fault segments may be detected which are not recorded by displacement maxima or fault morphology in equivalent detail. In addition, tracking of marker deflections geometries in the hanging wall facilitates the identification or prediction of equivalent structures in the footwall, which are obliterated in seismic data by the fault shadow, but may represent unconventional hydrocarbon traps in the footwall of a normal fault.

4.1 <u>Introduction</u>

The concept of fault growth by segment linkage is a common method used to explain the processes of fault evolution on various scales. Processes of segment linkage have been investigated from a micro and meso scale (e.g. Childs et al., 1996; Kristensen et al., 2008) up to the regional deformations (Peacock and Sanderson, 1991; Kelly et al., 1998; Gawthorpe et al., 2003; Marchal et al., 2003; Walsh et al., 2003; Davis et al., 2005). The segment linkage model assumes a progressive growth scheme, whereby the properties of a mature fault surface are a product of cumulative displacement increase due to the progressive enlargement and coalescence of individual segments (e.g. Nicol et al., 1995; Peacock, 2002; Walsh et al., 2002). Commonly, identification of fault segments is accomplished by analysis of the displacement distribution on the fault, which is sometimes combined with studies of fault morphology (e.g. Watterson, 1986; Barnett et al., 1987; Walsh and Watterson, 1989; Cartwright et al, 1995; Contreras et al., 2000; Kim and Sanderson, 2005; Marchal et al., 2003; Lohr et al., 2008).

Displacement along an isolated elliptical fault typically shows a decrease from the fault center to the tips (Walsh and Watterson, 1989). To accommodate this displacement gradient along the fault, adjacent marker layers show a deflection towards the fault commonly described as reverse fault drag, compensating the discontinuous displacement along the fault by a continuous displacement within the host rock (Barnett et al., 1987; Peacock and Sanderson, 1991; Reches and Eidelman, 1995; Gupta and Scholz, 2000; Grasemann et al., 2005). This conceptual model of the synchronous and mechanically related development of a hanging wall anticline and a footwall syncline adjacent to a normal fault is especially favorable in the case where a connection to a low-angle detachment fault at depth is not evident.

In this work, a high-resolution commercial 3D seismic dataset was analyzed, providing excellent spatial imaging of a ~16km long segment of the Markgrafneusiedl normal fault in the Vienna Basin, Austria. By detailed mapping of the fault plane and associated syn-and anticlines in the adjacent marker horizons a 3D structural model was created. From the depth-converted geometrical model we analyzed the displacement distribution and its relation to the observed fault drag. Thereby, we demonstrate that fault drag is a valuable additional criterion to constrain the evolution of large normal faults by the coalescence of initial segments.

4.2 <u>Geological setting</u>

The investigated area is located at the central part of Vienna basin (Fig 4-1a). This thin-skinned rhombohedral basin (Royden, 1985) covers 5000 km^2 and has been extensively studied for hydrocarbon exploration (Wessely, 1988; Hamilton et al., 2000; Strauss et al., 2006; Fuchs and Hamilton, 2006; Hölzel et al., 2010) as well as for seismic activity (Decker, 2005; Hinsch, et al., 2005a).

The Vienna basin is characterized by the three distinct stages of evolution, whereby the investigated near-fault sequence belongs to the pull-apart phase. The early basin formed in the lower Miocene (23 Ma) as a result of the lateral escape of the Eastern Alps (Ratschbacher et al., 1991; Peresson and Decker, 1997) along the Vienna Basin transfer fault whereby a final foreland imbrication lasted up to the Karpathian stage (17 Ma) (piggyback basin stage, Decker, 1996). The Early to Middle Miocene stratigraphic cycle uncomfortably covered pre-Miocene Alpine-Carpathian nappes whereby a successor left stepping en-échelon fault pattern was

comprised of the NE-striking sinistral faults and NNE-striking normal faults.
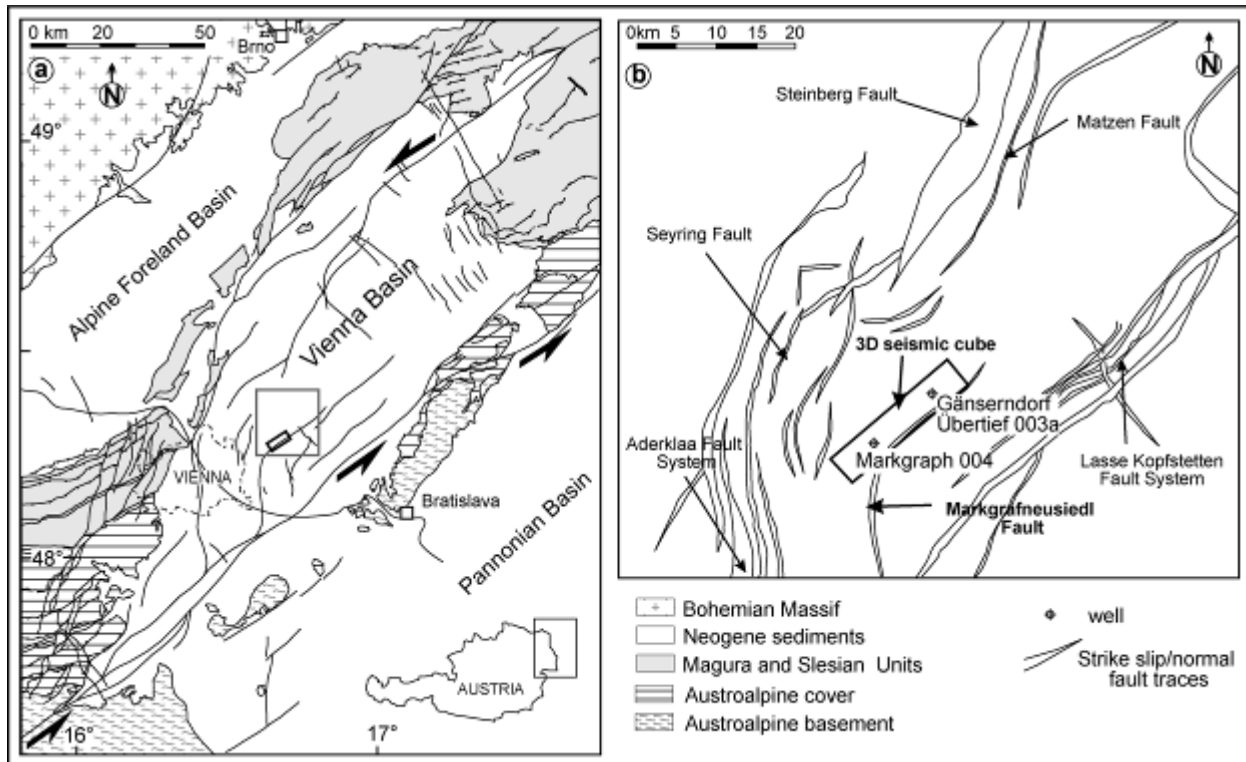
Figure 4-1. (a) Tectonic sketch map of the Vienna basin (modified after Strauss et al., 2006), (b) Position of the 3D seismic block Seyzamdue (OMV) near the Markgrafneusiedl fault that is investigated in this study, and the two deep exploration boreholes Markgrafneusiedl 004 and Gänserdorf Übertief 003a. Fault heaves from the structural map of the pre-Neogene basement (modified after Kröll and Wessely,1993).

The most prominent Salzach-Ennstal-Mariazell-Puchberg fault (Linzer et al., 2002) and accompanying structures delimited extensional duplexes (Decker, 1996). During this pull-apart stage of basin evolution, (Fodor, 1995; Decker, 1996) horizontal extension enabled rapid subsidence of up to 1500mm/Ma (Hölzel et al., 2008), whereby normal faulting was induced by lateral confinement of eastwards material removal (Peresson and Decker, 1997). Two depocenters were differentiated enabling sequence deposition dating from the Badenian (~16 Ma) (e.g. Fodor, 1995) up to the Pannonian age (8 Ma) (Hamilton et al., 2000).

The entire fault network (Fig 4-1b) of within Matzen-Schönkirchen gas and oil field (Brix and Schultz, 1993) located within Vienna Basin is almost

entirely known from 2D and 3D seismic data (Sauer et al., 1992). The central Vienna Basin normal faults are kinematically linked to strike-slip systems, whereby tectonic activity between Lower Sarmatian (13 Ma) and Lower Pannonian (~ 11,5 Ma) produced thick hanging wall growth strata that accompanied slip along normal faults (Hinsch et al., 2005b). However, in contrast to this general trend of sediment accumulation observed in sedimentary piles along the normal faults in the most of Vienna Basin, the investigated Markgrafneusiedl normal fault does not exhibit a prominent difference in the adjacent sediment thickness (Fig 4-2). Only a minor difference in a near-fault thickness of the hanging wall and footwall seismic record is observed below the top horizon h5 (Middle Pannonian). Therefore, this exclusively normal fault with no evidence of strike-slip movement (Beidinger, 2009) can be characterized by a lack of a prominent rollover. Instead of a large-scale rollover anticline, the near fault strata record reverse and normal drag structures with rather small and strongly variable amplitudes. This observation is supported by the lack of evidence for a listric fault geometry or a connection to a low angle detachment horizon at depth in the seismic dataset (Fig 4-2b). Alternatively, a relation of the observed folds to a reactivation of the fault with thrust kinematics is not documented by any structural evidence in this area.

Using a combination of the seismic and borehole data, the investigated Miocene depositional sequence is subdivided in several chronostratigraphic domains illustrated by different amplitude geometries recorded within the 3D seismic block. The sedimentary cycle begins with the limnic-fluvial Aderklaa Formation comprised of conglomerates, sandstones and interbedded pelites deposited on the pre-Neogene basement. After a change in the tectonic regime, sedimentation started discordantly during the Early Badenian with the deposition of the transgressive Aderklaa Conglomerate Formation representing a braided river system (Weissenbäck, 1996). In the central Vienna Basin the Badenian succession is characterized by distal and proximal deltaic clastics and carbonates (Strauss et al., 2006). After a period of sea-

level drop dated at the Badenian/Sarmatian boundary, a renewed transgression in Sarmatian resulted in the deposition of marls and clays within the central areas of the basin. In the subsequent Early to Middle Pannonian period another transgression covered most of the Sarmatian succession (Harzhauser et al., 2004) with a clayey and sandy lacustrine sequence. The Middle Pannonian Formation Top is the highest section of the seismic dataset that is chronostratigraphicaly constrained and is represented by a similar clastic sequence.

4.3 **Seismic dataset and analytical methods**

4.3.1 **3D seismic data from the Vienna Basin**

The database used for this study is a high-resolution 3D seismic survey located at the central part of Vienna Basin (Fig 4-1). The time-migrated 3D seismic reflection dataset covers ~64 km^2 with a recording time of 4000 ms TWT (Two-Way-Traveltime; corresponding to about 7 km depth) and has line spacing of 25m with ca. 30 m vertical resolution.

The seismic amplitudes provided satisfactory resolution of morphological changes in map view, as well as in cross-sections enabling high-resolution seismic images of the near-fault material (Fig 4-2). The chronostratigraphic framework was constrained in an OMV in-house work by calibration with numerous deep exploration boreholes. The five most prominent, and continuously traceable seismic markers characterized by distinctive high amplitudes were mapped in the 3D seismic cube, i.e. h1 (Lower Sarmatian), h2 (Lower Pannonian), h3 (Middle Pannonian), h4
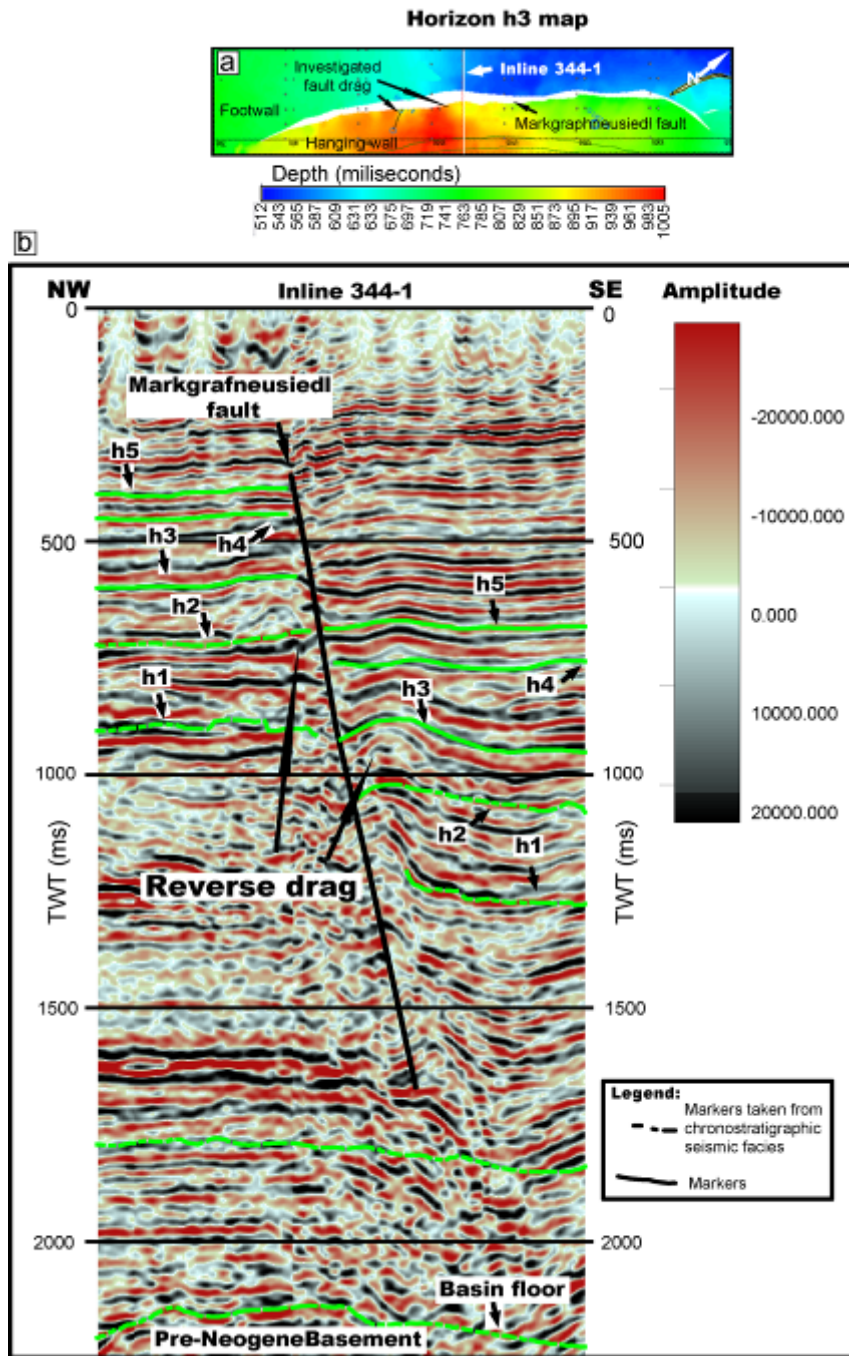
Figure 4-2. (a) The mapped horizon h3 (Middle Pannonian -20) within the 3D seismic block indicated as the rectangle at Fig1b. Reverse drag of marker is clearly visible in hanging wall, but also gently developed in the footwall of the Markgrafneusiedl fault. Map of the horizon h3 is separated by the Markgrafneusiedl fault into the two seismic domains: hanging wall (SE) and footwall (NW). (b) The seismic inline 344-1. The five most prominent seismic amplitudes as stratigraphic markers were seismically constrained throughout the entire 3D cube volume: h1

(Lower Sarmatian), h2 (Lower Pannonian), h3 (Middle Pannonian -20), h4 (Middle Pannonian -12) and h5 (Middle Pannonian -5).

(Middle Pannonian) and h5 (Middle Pannonian). As the resolution of the seismic data and the quality of the markers decreases significantly with depth (roughly below 1300 ms TWT), our investigation is focused on the sedimentary pile deposited from the top Lower Sarmatian up to Middle Pannonian period (Fig 4-2b).

The 3D interpretation and fault mapping was based on detailed picking of the aforementioned horizons in numerous inlines, crosslines and additional lines roughly perpendicular to the fault strike using the seismic interpretation software Landmark (GeoGraphix). Subsequently, horizon and fault surfaces were generated in Gocad (Paradigm)by triangulation from the mapped datapoints using preferably equilateral triangles. The elements of the resulting 3D structural model mapped in TWT were subsequently converted to depth using a formula proposed by Hinsch et al. (2005b), assuming an exponential increase of the seismic velocity with depth in the Miocene sedimentary succession due to an increase in compaction with depth.

4.3.2 Generation of a structural model

The final 3D model contains a section approximately from 230 m down to 2800 m of Markgrafneusiedl normal fault. The model was constructed by using the 3D seismic data and information from the boreholes indicated in Fig. 4-1b. The quality seismic data provided a traceable fault plane almost down to the basement rocks (Fig 4-2), but unfortunately, reflections in a vicinity of the lower fault tip are below seismic resolution. The highly irregular seismic amplitude pattern in this lower section of the 3D block, having a poor visual traceability is extremely difficult to map accurately. In contrast, the central fault region contains abundant continuous subhorizontal seismic amplitudes that are excellently traceable as stratigraphic horizons.

Therefore, the interpretation that is restricted to the central fault section was bracketed the investigated fault area between 280m to 1350m (Fig 4-3a). Using this fault section, we analyzed the displacement distribution between four hanging wall and footwall horizons, h2 up to h5. Displacement near marginal markers records a sudden decrease that is actually an artifact induced by a lack of traceable horizons. Therefore, in order to avoid erroneous interpretation we disregarded displacement values adjacent to the hanging wall of a boundary horizon h1, and above a footwall of the marker h5.

In order to characterize the geometry of the fault surface and the deformed horizons, we carefully analyzed five different attributes, i.e. fault azimuth, fault dip, fault curvature, horizon dip and fault displacement within the depth migrated structural model. For the visualization of the fault topography, we calculated the Gaussian curvature (k_G) across the entire fault surface. The Gaussian curvature is the product of the minimum and maximum curvature at a point. Cylindrical structures or flat planes have a value of $k_G=0$, while saddles have $k_G<0$ and domes or basins $k_G>0$ (e.g. Mynatt et al., 2007; Lisle and Tomil, 2007). Areas wih $k_G \neq 0$ represent irregularities or corrugations in the fault surface probably associated with older fault segments (e.g., Walsh et al., 1999; Mansfield and Cartwright, 2000; Marchal et al., 2003). Accordingly, areas with positive curvature are convex to the hanging wall, and indicate areas of linkage, while areas with negative curvature are concave to the hanging wall and represent former segments (Lohr et al., 2008). In addition to fault curvature, dip and azimuth are calculated from each of the equally sized, equilateral triangles of the fault plane.

Once the fault morphology was constrained, the fault displacement was calculated by using the five horizons listed above (h1 to h5). The 3D fault displacement mapping is constructed in Gocad by defining the upper and lower boundary of the horizons (cutoff lines) and subsequent

computation of a midline between the cutoff lines. Finally, the fault surface is color-coded with the throw information based on the constructed midline.

4.4 <u>Geometrical analysis of fault plane and marker horizons</u>

4.4.1 Geometric features of the fault surface

Geometric features of the fault surface were analyzed to identify heterogeneities, and were subsequently correlated with the distribution of displacement along the fault surface, calculated from the five investigated horizons. For these analyses, only the central section of the investigated fault was considered, which shows the most prominent and thus best interpretable geometrical variations (Fig 4-3a).

Fault azimuth and dip

The average azimuth of the investigated section of the fault lies around 40-65° whereby areas displaying the dominating azimuth can be summarized as Region 1 (Fig 4-3b). However, there are several areas with deviating azimuth values oriented roughly parallel to the fault dip, which separate these areas of homogeneously average azimuth values. These localized deviations roughly correlate with the areas of highest dip values >60° (Fig 4-3c). The area marked as Region 2 comprises two subparallel zones of higher (to the SE) and lower (to the NW) azimuth than average, and corresponding high and low dip angles.

Fault curvature

The values of Gaussian curvature are highly variable across the fault surface (Fig. 4-3d). Zones with zero curvature are elongated roughly parallel to the fault dip, and represent cylindrical corrugations along the fault plane. These cylindrical areas are interrupted by zones of negative curvature, which

are interpreted as former fault segments. The maximum negative curvature values are located at former segment tips. The linkage zones between these
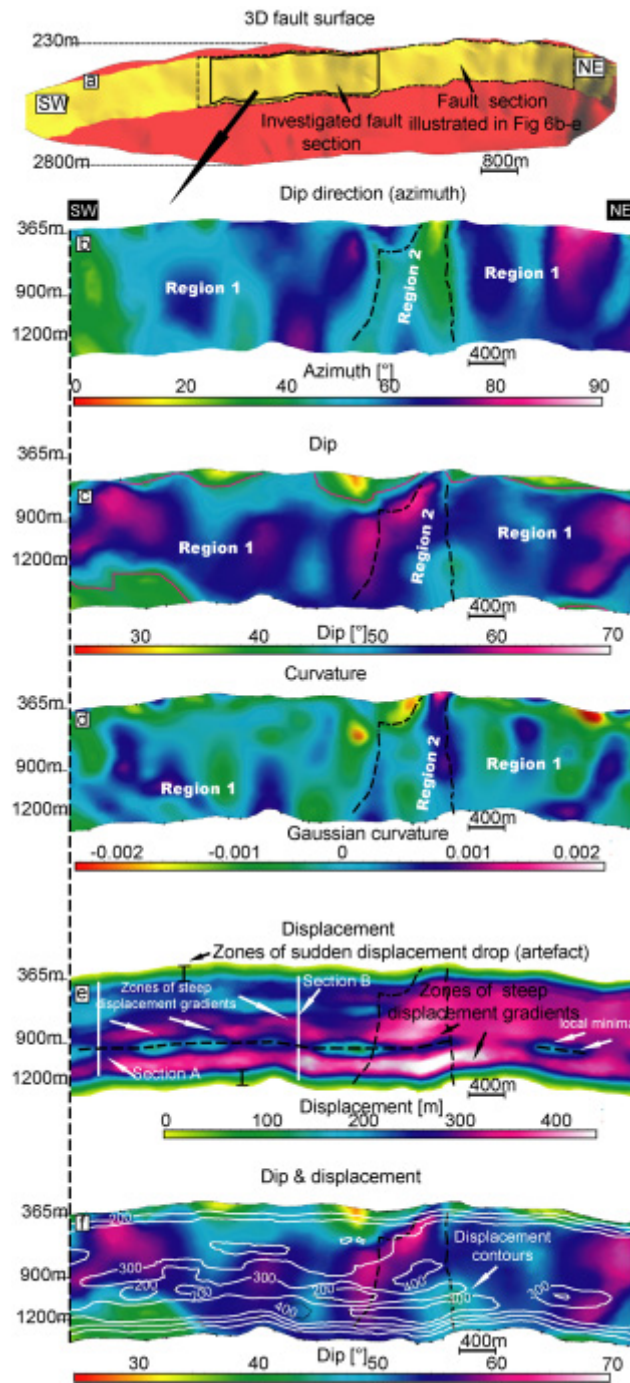
Figure 4-3. (a) Oblique-frontal view to the 3D modeled surface of the investigated part of the Markgrafneusiedl fault, including the position of the section analyzed in detail in (b-f). Fault attribute maps: (b) Dip direction (azimuth) map, (c) Dip map, (d) Gaussian curvature map,(e)

Displacement map, (f) Cross plot of dip and displacement map. See the main text for a detailed explanation.

initial segments are characterized by positive curvature values. Zones comprising high dip are in good correlation with zones of negative Gaussian curvature, i.e. the assumed fault segments. In contrast, a correlative mixture of high and low dip angle sections characterizes the linkage zones or areas of positive Gaussian curvature. Generally, all of these structural features are aligned parallel to the fault dip, suggesting the evolution of the fault plane from a train of small, vertically elongated fault segments, which at a later stage linked to form a common fault plane. On a larger scale, Region 2 is highlighted by azimuth, dip and curvature values deviating from the mean values, and can thus be interpreted as a linkage zone between two earlier, large but geometrically poorly detectable segments (i.e. the two areas marked as Region 1 and separated by Region 2). Dip values ranging around 40° and less (green and yellow areas delimited by a red line in Fig 4-3c) distributed as a "belt of localized dip islands" seems to have a delimiting role of the upper section of a Region 1. This observation is underpinned by areas of low negative curvature (yellowish-green areas on the Fig 4-3d parallel to section boundaries) and thus this irregular discrepancy can represent a vertical contact of the two earlier poorly recognizable large segments.

Fault displacement

Similar to the previously investigated geometrical attributes, the displacement distribution contoured on the fault surface also gives an irregular pattern (Fig. 4-3e). Zones lining the top and bottom of the investigated fault section are artifacts, which result from the lack of traceable horizons above and below these depths. The displacement distribution map indicates two prominent areas of displacement maxima (~400 m and 480 m), which are elongated roughly along the fault strike. These zones are interrupted by several local minima with only 150 - 200 m

of displacement, aligned as a string of elliptical contours at two distinct depth levels. The transition between the maxima and the local minima are marked by steep displacement gradients. Generally, the NE part of the investigated fault section displays larger areas of high displacement, while the SW part, especially in the upper half of the fault, shows by trend lower displacement values. The transition between these zones occurs roughly at the center of the investigated fault section.

Fault displacement-distance plots and relation to fault dip

The overlapped dip and displacement contour-attribute map (Fig 4-3f) discloses the fact that the areas of steep displacement gradient (narrow area between highest and lower displacement) are represented by slightly higher dip values (>60°) than the displacement maxima itself. Generally, the dip values of the investigated triangles range between 28 and 76° (Fig 4-4a), displaying roughly a normal distribution with a mean around 51°. To analyze the relation between dip and maximum displacement, we plot the extracted dip values against the maximum displacement of the corresponding area. The results indicate a correlation between fault dip and displacement (Fig 4-4b), whereby fault sections of 30-40° dip correlate with a maximum displacement of ~280 m, whereas the sections of 40-44° have significantly higher maxima of 400 m. At last, sections with the steepest dip angles of 45-50° are characterized by maximum displacement values of up to 480 m. A vertical displacement value is actually a 3D vector value measured between two separated points at the intersection between of the marker in the hanging wall and footwall. In both vertical displacement profiles, displacement is measured exclusively along the investigated fault section (indicated in Fig. 4-3a), and is not measured from the actual fault tips due to the lack of reliable horizons.
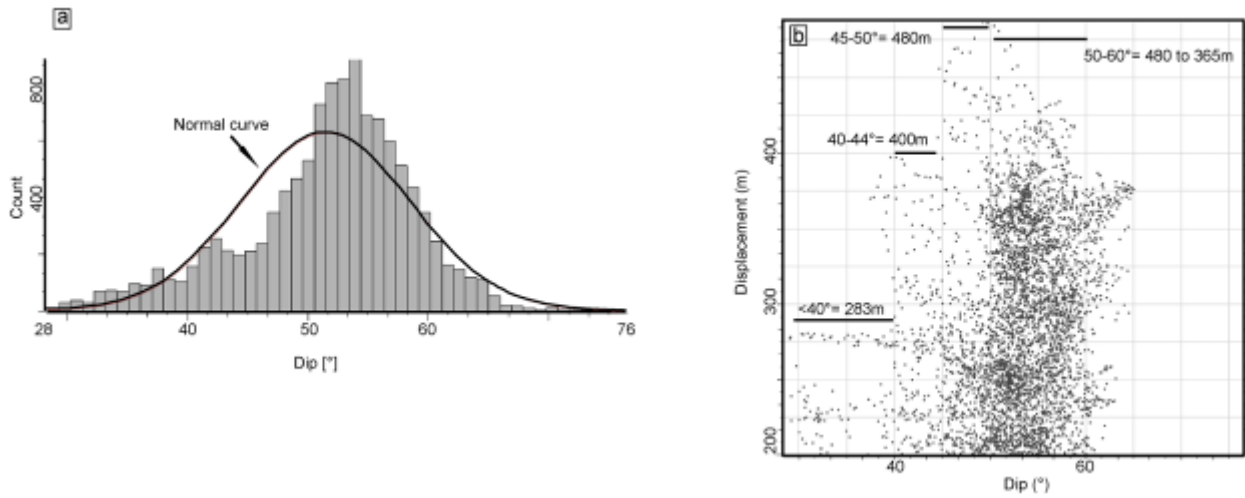
Figure 4-4. (a) Histogram of the dip attribute map. (b) The dip-displacement point-based diagram illustrates the relation between maximal displacement and dip angle. Fault sections between 30°-40° have a maximum displacement of ~280m, whereas the sections of (ii) 40°-45° have the maxima of 400m and finally the sections of (iii) 45-50° are characterized by max values of 480m.
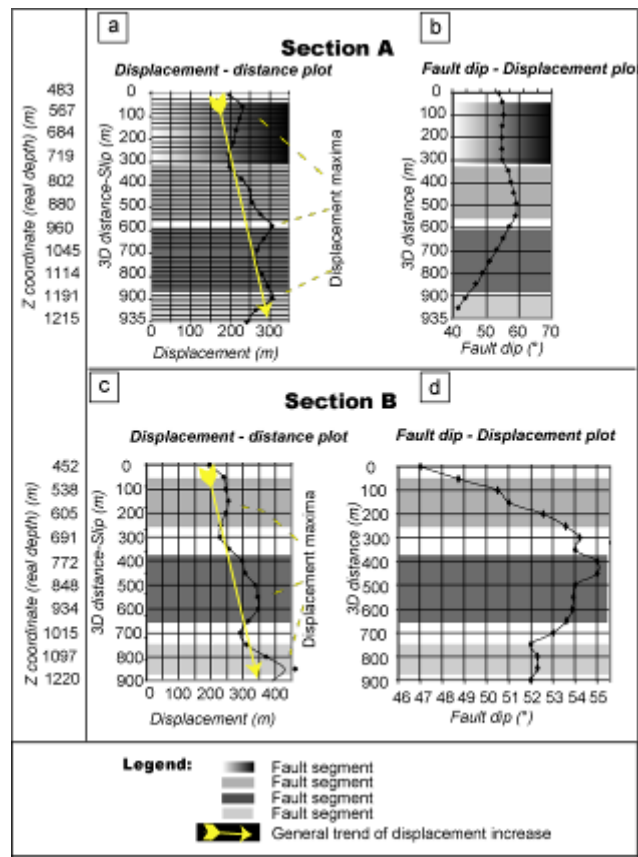
Figure 4-5. Displacement-distance plots (a, c) of two sections (A and B, marked in Fig. 3e) recorded along the dip direction of the Markgrafneusiedl fault, and the corresponding dip-displacement profiles (b, d). The maximum displacement measured along both sections varies between 200 and 425 m. The displacement maxima are separated by the several minima, whereby a general increase in displacement downwards can be observed. Both in displacement and in dip-distance diagrams, sections with a similar dip are marked. Changes in dip angles commonly correlate with changes in displacement along the fault.

The profiles A and B exhibit three prominent maxima that are separated by the two minima in Sections A and B, whereby a general increase in displacement is observed downwards i.e. towards the deeper fault sections (Fig 4-5a and 4-5c). The fault dip-distance plots (Fig 4-5b and 4-5d allow a distinction of vertical sections comprised of areas with a similar dip, whereby sudden variations in dip angle point to the existence of a segment boundary.

4.4.2 Geometric features of marker horizons

Variation of reverse and normal fault drag along dip and strike of the fault

The 3D structural model reveals a complicated pattern of antiform-synform folding ('antiform-synform fold train', Grasemann et al, 2003) developed in both hanging wall and footwall domains (Fig 4-6a-e).

Within the hanging wall, the deepest reliable horizon h2 illustrates the lowest structural section of the investigated fault part, approximately at the center of the Markgrafneusiedl fault. In the 3D perspective view of the horizon color-coded for depth, three distinctive features of relatively high-amplitude-wavelength reverse drag structures - R1, R2 and R3 - are developed (Fig 4-6b, yellow colored sections of the marker h2). Each reverse drag structure is separated by a similar amplitude normal drag - N1, N2, N3

- whereby N3 has significantly larger amplitude (Fig 4-6b, light red colored sections of the marker h2).

Figure 4-6. (a) Oblique view on the 3D modeled reverse and normal drag developed within the footwall and hanging wall of the Markgrafneusiedl fault. The sections of the 3D model illustrated the different amplitudes reverse and normal drags distributed within the hanging wall

tracked from a bottom towards a higher fault domain: (b) marker h2, (c) marker h3, (d) marker h4, (e) marker h5. (f)-(h) Contact between the marker h3 and the fault, associating the fault attributes (dip, curvature and displacement) with the fault drag geometry (g) additionally displays the more gentle, large scale reverse and normal drag superposed onto the smaller scale features . i) Dip of the marker horizon recorded along the fault strike varies between 0 and 27° (location of the profile marked in (h)), illustrating alternating reverse and normal drag along the fault.

The fault drag amplitude is represented by the maximum curvature of a particular fold measured from the zero Gaussian curvature contour (Fig 4-6b-e, approximation of zero curvature represented in black lines). The distribution of the fault drag structures with a different sense within the footwall (Fig. 4-6a) is complementary with the hanging wall fault drag array, however, unlike the high drag amplitudes recorded within the hanging wall, the footwall amplitudes are significantly lower but still are visible and mathematically measurable. For example the footwall normal drag N1' (Fig 4-6a) juxtaposed to N1 with 24m of amplitude has only a magnitude of ~6 m. Difference in fault drag volumes can be explained by several reasons (for a detailed explanation see chapter 5.4.). In order to illustrate the relationship between fault segments and fault drag, omitting uncertain footwall drag amplitude discussion, we confined the investigation on the well-developed drag structures in the hanging wall. In contrast to the previously described three prominent reverse drags (R1, R2 and R3), the most prominent feature is a large-scale normal drag (N3), which is developed in all of the four investigated horizons (Fig. 4-6b-e). Large normal drag is associated to the adjacent Region 2 of the fault surface. This high-amplitude, downwards deflected hanging wall feature clearly separates the central region of all markers from the surrounding large positively upwards-deflected host rock material (Fig 4-6b, 'generalized drag geometry').

In the next investigated horizon h3, ca. 100 m above h2, the magnitude of the locally developed reverse drags R1, R2 and R3 slightly decreases (Fig 4-6c). The two reverse drag features R2 and R3 that are

developed near the large-scale normal drag N3 are coalesced, and are here represented by a single reverse drag (R2+3). A decrease in amplitude, including a modification of the drag sense and coalescence of the two neighboring drag features (R2 and R3) are in accordance with the local distribution of displacement along the fault plane.

In the upper fault sections (horizon h4, Fig 4-6d), the amplitude of reverse drag including the amplitude of large-scale normal drag record a general decrease. The reverse drag features accommodated across the Region 1 dominate the horizon geometry in comparison to normal drag, whereby the large central marker depression (N3) also records a volume drop. R1 and R2 form a single reverse drag structure (R1+2) with two local maxima but with a negligible interruption by, compare to the distinct N1 feature observed in the horizons below and above. In contrast, N2 is well developed between R3 and the R1+2 structures. A decrease of the h4 marker amplitudes is most likely associated with a decrease of the finite displacement that is related to the proximity of fault tips (large upper contact of Region 1, red line in Fig 4-3c).

A similar situation can be observed across the shallowest horizon h5 (Fig 4-6e), where the drag amplitude and the finite offset further decreases. However, R1, N1, R2, N2, R3 and N3 can be still discriminated.

Correlation between fault drag and fault attributes

In order to examine the correlation between fault drag and other fault attributes, we focus on the drag geometries of horizon h3 (Fig 4-6f, g and h), analyzing the drag features from left to right along the fault. The R1 substructure is a well developed reverse drag antiform, which is related to a negative Gaussian curvature (Fig 4-6f) as well as a local displacement maximum of ~400 m (Fig. 4-6g) and moderate fault dip values (Fig. 4-6h). In summary, these observations suggest that the location of R1 represents an initial fault segment.

The neighboring normal drag N1 is spatially restricted between the two well-developed reverse drags, R1 and R2+3. N1 is developed around a field of positive Gaussian curvature, suggesting a position at a local transfer or tip zone. Additionally, both small displacement values, as well as high dip values in this area contribute to this assumption.

The R2+3 represents the locally developed fault drag cluster comprised of three distinguishable amplitude maxima (R2+3a ~ 42 m, R2+3b ~ 21 m, R2+3c ~ 31 m). Along the fault plane, R2+3 is associated with the vertical contact between zones of positive and negative curvature (Fig 4-6f), moderate to high dip values (Fig. 4-6h). The position of R2+3a, which shows the highest amplitude within this cluster of reverse drag, fits perfectly to a high displacement field of ~400 m (Fig 4-6g) The decrease in drag amplitude of R2+3b and R2+3c is related to a decrease in displacement and a zone of negative curvature, probably indicating a later generation relative to R2+3a ,and subsequent coalescence of the two segments.

Further to the right, the amplitude of R2+3 decreases, where eventually the entire reverse drag cluster changes amplitude sign and transits into the large single normal drag (N3). The occurrence of N3 is related to the Region 2 where additionally the displacement maximum of the investigated fault section is located (Fig. 4-6g). The displacement maxima are accompanied by a large normal drag (instead of large reverse drag) comprised of no substructures, we assume that the growth of the N3 is a result of a single propagation event associated with this presumably overlap zone (henceforth F3) between the fault tips of morphologically almost undetectable two large segments (henceforth F1 and F2).

The 3D structural model illustrates the geometrical properties of fault drag emphasizing a significant difference in amplitude between the R1, N1, R2, N2 with respect to the N3. By quantifying amplitude variations, a link between localized fault drag cluster represented by R1, N1, R2, N2 and the

two larger reverse drag structures, separated by N3 (Fig 4-6b, 'generalized drag geometry') can be constrained.

4.4.3 Interpretation of fault architecture

The quantification of fault drag across the horizons h2-h5 clearly indentifies the initial fault segments, however using a fault morphological analysis, the linkage of initial segments resulting in the formation of F1 and F2 is rather unclear.

Linkage or overlap zones are characterized by a distinctive morphology of branch domains (branch lines) (e.g. Walsh et al, 1999). These zones are actually a result of progressive replacement of fault tips during development of linkage zones. Kinematically, the overlapping fault zones can be characterized by a steepening and positioning of the maximum slip that is localized near or inside relay zones (e.g. Peacock and Sanderson, 1991; Marshal et al., 2003).

Fault segment F3 which contains two displacement maxima (Fig. 4-3e) is characterized by a distinctive morphology of overlapping zones (azimuth map, Fig 4-3b) (e.g. Walsh et al, 1999). In addition to these two indicative features of the F3, in the adjacent marker horizons a large normal drag (N3) is developed. This discrepancy can be interpreted as a sign for a secondary or late propagation between the two large faults (e.g Rykkelid and Fossen., 2002) therefore suggesting that the Region 1 is actually divided on two faults (F1 and F2). Confirmation of such spatial arrangement comes from the fact that F1 and F2 already accumulated displacement and caused reverse drag formation in the adjacent markers. Once a thoroughgoing fault surface between F1 and F2 was established, the maximum displacement was accumulated in this central area of the fault, but no reverse drag could be generated due to a lack of displacement gradient. The observed N3 normal drag geometry along F3 is thus interpreted as an inherited feature, which formed at the lateral tips of the early F1 and F2 fault segments.

4.5 <u>Discussion</u>

The structural model of the Markgrafneusiedl fault surface shows the complex morphology of the fault surface and heterogeneous displacement patterns of marker horizons (Fig 4-6). In the following, we want to discuss how geometric parameters are related to mechanical linkage of fault segments and derive a growth history of the Markgrafneusiedl fault including a prediction of the deformation in the footwall of the fault, which is usually poorly constrained by 3D seismics.

4.5.1 Fault displacement and morphology as criterions for segmented faults

The fundamental geometric values that can help to differentiate models of formation of a fault zone or fault array are parameters that identify individual fault segments that may link during fault growth (Walsh et al., 2003). Displacement distribution of faults may help to identify mechanically individual segments from segments that are mechanically hard or soft linked (Fig 2 of Walsh et al., 2003). However, in highly complex large fault zones where fault tips are not exposed in the investigated section, simple displacement – distance analyses may result in rather ambiguous or unclear results. The along-strike displacement – distance profile of the Markgrafneusiedl fault segment (Fig 4-7b and 4-7c) records variations in displacements that are not always directly related to fault segments.
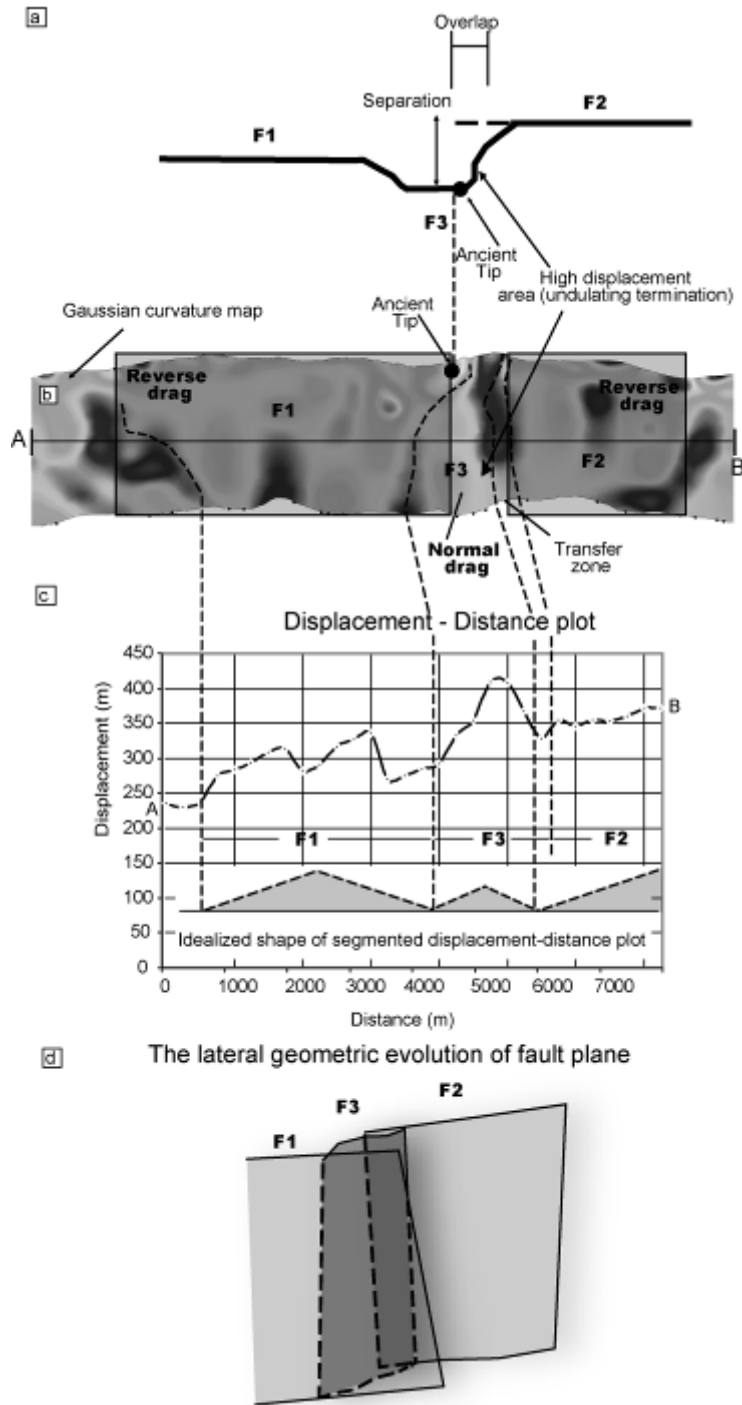
Figure 4-7. (a) Schematic map (top view) and (b) the Gaussian curvature 3D map of the fault plane (oblique view), where two large, slightly overlapping fault segments (F1 and F2) are connected by a relay fault (F3). The presumably older segments F1 and F2 show a reverse drag of the adjacent markers on a large scale (see Fig.6cand 6g), while the relay fault F3 is related to markers with a normal drag. (c) Correlation of the 3D displacement attribute map with the

along strike throw-distance plot (d) Schematic sketch of the relay zone between F1 and F2 breached by the relay fault F3.

The most illustrative section of a displacement profile that might cause an ambiguous interpretation is associated to the section near the F3, where a low displacement zone (tip zone between two segments) should be expected. Surprisingly, this section is characterized by the maximum finite displacement because the inherited tips are connected by the relay fault F3 (Fig 4-7c and 4-7d). Therefore, the linkage and subsequent displacement migration may cause an abrupt finite displacement increase. Such asymmetric slip distributions and/or multiple slip maxima on normal faults may be the result of linkage of individual fault segments or may reflect mechanical interaction between intersecting faults (Peacock and Sanderson, 1996) that produce local perturbations of the stress field resolved on the faults (Maerten et al., 1999). Numerical elastic models demonstrate that multiple slip maxima forced by intersecting faults are not located along the intersections, nor at the fault centers. Therefore, the use of displacement distance plots alone are of limited practical use for the detection of fault segments, especially around such complicated large faults.

In order to increase the limited information of slip distributions along faults, other studies combined analysis of the 3D geometry of segmented faults with displacement asymmetry measurements (e.g. Childs et al., 2003; Lohr et al., 2008). Analyzing a synsedimentary fault, Childs et al., (2003) constructed the varying throw contour patterns on the strike fault projections demonstrating that the locations of fault maximum and minimum fields indicated local growth directions. Lohr et al., (2008) combined 3D fault morphology data with displacement distance graphs, suggesting that the fault segmentation is reflected by triangular to half elliptical shaped real displacement profiles superimposed to the 3D fault segmentation pattern. By using true displacement in along slip normal movement the authors demonstrated significant differences in a real displacement, vertical and

horizontal displacements identifying the former fault segments. The authors caution the use of throw values, which lead to a smoothing of the real displacement curves. Displacement analyses along the Markgrafneusiedl fault demonstrate that results of both techniques, the displacement distance profiles (Fig 4-7c) and the 3D vertical displacement distance plot (Fig 4-5) exhibited a series of local displacement maxima and minima that are weakly correlative with adjacent segment centers or linkage zones.

The mechanical linking of differently sized segments can result in a significant change of the inherited displacement pattern (Zee and Urai, 2005) and therefore analysis of the plot or 3D displacement attribute map of the Markgrafneusiedl fault provided no satisfactory evidences supporting individual segment boundaries delineation, propagation and eventual linkage. Another difficulty in determining the hierarchy of factors that affect the progressive change in displacement is expressed as a constant propagation of local segments that are active even after larger segments being linked. This mechanical interaction is caused by release of large strains in the regions of segments contact (Dawers and Anders, 1994).

Many studies designated fault morphology and fault displacement profiles as techniques that provide either influenced (e.g. Peacock and Sanderson, 1996; Nicol, 1996, Bürgmann, 1994) or incomplete and unclear picture of the possible initial fault segments (Lohr et al., 2008). However, since the segmentation and fault linkage clearly influences the displacement pattern along the fault (Maerten et al., 1999; Walsh et al., 2002) and since displacement gradients generates fault drag, quantification of fault drag may help to detect linked fault segments.

4.5.2 Fault drag as a criterion to identify fault segments

As a result of a fault slip, heterogeneous stress and displacement fields develop in the surrounding rock (Pollard and Segall, 1987). Elastic theory predict and some natural faults demonstrate that the displacement field

around an isolated fault is elliptical, reaching a maximum at the center of the fault and dropping to zero at the fault tips (Rippon, 1985; Barnett et al., 1987; Pollard and Segall, 1987; Walsh and Watterson, 1989). However, the infinite displacement gradient at the fault tips may be significantly influenced by changes in the frictional strength along a fault, spatial gradients in the stress field, inelastic deformation near fault terminations and variations of the elastic modulus of the host rock (Martel, 1997; Cowie and Shipton, 1998; Bürgmann et al., 1999).

The wavelength and the amplitude of fault drag is mainly a function of size, the finite displacement and the displacement gradient of the fault (Grasemann et al., 2005). Larger amplitude drags are facilitated by constant wavelengths (e.g. confined faults) during increasing fault slip (Fig. 4-8a). During fault segment linkage, different wavelength and amplitude of fault drag may be superposed on inherited smaller wavelength and amplitude drag geometries (Fig. 4-8b and 4-8c). Even the sense of the drag (e.g. normal drag) may be inherited in a linked larger structure (e.g. reverse drag).

Fault drag has been described and analyzed in natural examples at various scales, as well as in analogue and numerical models (e.g. Barnett et al., 1987; Passchier, 2001; Exner et al, 2004; Coelho et al., 2005; Grasemann et al., 2005; Wiesmayr and Grasemann, 2005; Resor, 2008 and Spahić et al., in press). The modeling results of drag around a single finite fault plane predict different drag sense on a central marker line (reverse or normal) as a function of the orientation of the marker line with the fault. Importantly, the magnitude but also the sense of drag must change on

Mechanism of a progressive fault drag magnitude development around fault segment

[a]

Stage 3

Stage 2

Stage 1

Fault drag amplitude

Segment length

No or restricted segment spatial propagation

Unrestricted radial segment growth

Stages 1 and 2: Segments propagation and subsequent linkage

[b]

Reverse drag

Breaching point (zone of large normal drag relict)

Reverse drag

Normal drag

Reverse drag

Fault segment

Fault segment

Enlarged fault segment

Stage 3: Mature fault zone with multiple segment generations

[c]

Fault drag discrepancies (small segment reverse drag)

Fault drag discrepancies (small segment normal drag)

Generalized reverse drag geometry

Fault undulations

Large fault surface

Figure 4-8. Normalized fault (segment) length – fault drag amplitude diagram illustrating the mechanism of progressive fault drag amplitude development (top view). Initially growth of isolated non-restricted fault segment presented has symmetry in fault length and drag amplitude (stage 1). Subsequently after segment tips being restricted, an amplitude increase is likely to occur (stage 2 and 3). (b) Schematic growth model and coalescence of two different laterally juxtaposed fault segments with the similar amplitudes. After segments have coalesced, a relic of normal drag remained. (c) A schematic growth model of final large-scale fault surface accompanied by the overall reverse fault drag that records a slight amplitude increase. The overall drag geometry is disturbed by the continuous propagation of local segments.

marker horizons, which do not meet the center of the fault, in order to maintain strain compatibility (Grasemann et al., 2005). Consequently, a smaller wavelength/amplitude drag may change its sense during fault propagation and/or linkage because the relative position of the marker with respect to the center of the fault has changed.

An excellent example of inherited drag is preserved in the horizons h2-h5 along the Markgrafneusiedl fault (Fig. 4-6), where the association of reverse and normal drag (anti- and synforms) may represent earlier individual fault segments that finally linked by the fault segment F1.

The suggested growth history of the Markgrafneusiedl fault is not intuitive from the displacement and morphology analysis of the fault alone because of the heterogeneous displacement gradient superposition due to fault linkage By including in our investigations the mapping of drag along the marker horizons, we present in the following a suggested growth history for the Markgrafneusiedl fault (Fig 4-9).

4.5.3 Evolution of the Markgrafneusiedl fault

The investigated section of the Markgrafneusiedl fault dating from the Lower Sarmatian up to almost Middle Pannonian time evolved in three distinctive growth phases. We assume that the Markgrafneusiedl fault propagated progressively towards the today tip zones since the fault dimensions and displacement values display a general decrease towards the fault tips.

The nucleation of the discontinuity was most likely induced by the activity of a precursor fault embedded in a pre-Neogene basement (see Kröll and Wessely, 2000). Locally distributed and isolated fault planes of similar size generated fault drag structures in the adjacent sedimentary horizons (Fig 4-9a). A maximum age of the initial propagation phase is the Lower Pannonian (~11 Ma), since the oldest fault drag is observed in the horizon

h3.
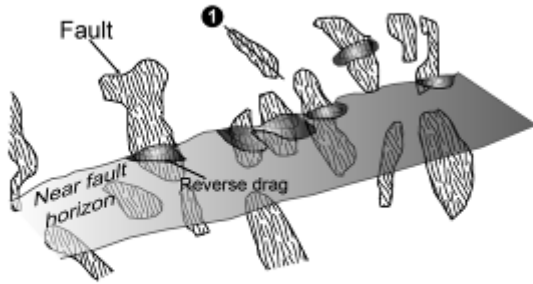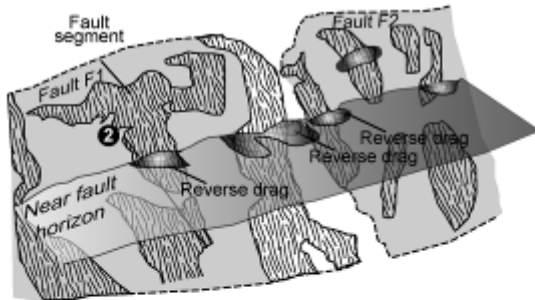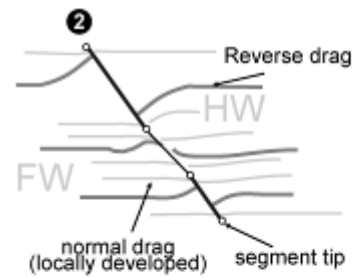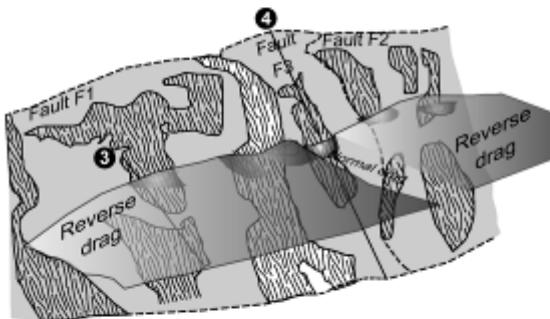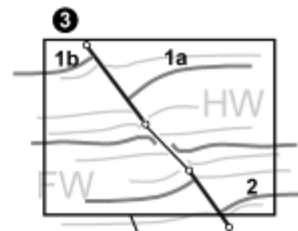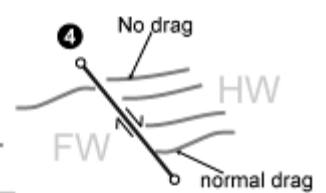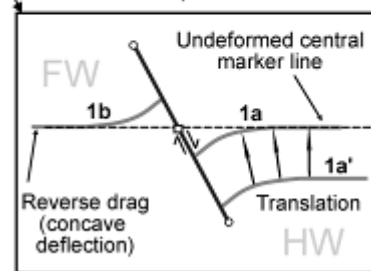
Figure 4-9. A schematic illustration of the evolution of a Markgrafneusiedl fault (left, oblique 3D view on schematic reconstruction; right, schematic cross-section): (a) isolated small fault

segments produce reverse fault drag in the adjacent marker horizons; (b) propagation and linkage of initial localized segments towards the larger fault segments F1 and F2 which are also associated with a larger reverse drag (c) relay fault F3 breaches the overlap between the large segments, and generates normal drag geometries in the adjacent marker horizons (d) schematic cross-section illustrating the prediction technique of a not-displaced (1a and 1b) and displaced reverse drag in a far fault deformation field (1a'). The technique of prediction is described in text.

After the vertically elongated faults have linked (Fig 4-9b), the successive deformation phase was characterized by a new enlarged, but still separated displacement field associated to the newly generated larger fault segments F1 and F2. The new resulting perturbation strain induced mechanical interaction between two segment generation, resulting in a localized mild obliteration of the inherited drag amplitude pattern unraveled by the minor amplitude fluctuations within the R2+3. Finally, lateral bifurcation of the fault tips of faults F1 and F2 ended in a linkage leaving a single normal large drag (N3) that accompanies propagation of this overlap (Fig. 4-9c). The volume of N3 records a progressive drop directed towards the higher fault sections (from h2 towards h5), whereby significant decrease is associated to Middle Pannonian, in a time between the markers h4 and h5. Additionally, the h5 illustrated lowest or zero amplitude of N3, corroborating suggestions that the linkage of F1 and F2 was before h5. This once propagating relay zone evolved in a typical geometry that characterizes relay faults ('completely breached relay zones' (Marchal et al., 2003, Fig.16-6). After the relay zone was breached, the spatial restriction of the new fault F3 disabled further lateral propagation, enabling accumulation of larger strains (Ackermann et al., 2001). Thus, the largest finite displacement values are associated to the today's central fault section that is tapered around the segment F3.

Including fault drag into the standard investigations of fault evolution, a growth history of a Markgrafneusiedl fault zone has been suggested. In the following, we use the same technique in order to predict the footwall

geometry of the Markgrafneusiedl fault, which is less well constrained by 3D seismics than the horizons in the hanging wall.

4.5.4 Footwall geometry prediction

Deformation in the footwall is frequently observed in outcrops and seismic data (Kasahara, 1981; McConnell et al., 1997; Mansfield and Cartwright, 2000) but hanging wall deformation is much better constrained in structural models of faults (Tearpock and Bishke, 2003) because of following reasons. Firstly, displacements due to a drag effect in the footwall can be less intensive than those in the hanging wall, especially when inclined faults interact with the earth surface (Grasemann et al., 2005). However, footwall deformation along near surface faults provides a strong evidence that the fault has a displacement gradient (e.g. Spahić et al., in press). Secondly, the resolution of 3D seismic record near a fault plane may frequently result in a much higher resolution within a hanging wall (Tearpock and Bischke, 2005) whereby a footwall record is often obscured or can have poor seismic resolution (e.g. compare lower structural levels of the footwall in Fig 4-2b). Furthermore, it has been shown that flattening normal faults are disappearing in the seismic data with increasing depth (e.g. Tearpock and Bischke, 2003). Listric fault models (e.g. McClay et al., 1990) have been frequently used to define a structural model for hydrocarbon exploration near large normal faults. Since many of these models are based upon the assumption that the footwall below the fault surface behaves as a rigid body (e.g. Yamada and McClay, 2003), the petroleum targets are mainly confined to the hanging wall anticlines. In contrast to the listric model predictions, against the commonly observed hanging wall reverse drag assets above a finite normal fault, (e.g. Porras et al., 2002) an additional hydrocarbon reservoir could be expected within footwall synclines. Unfortunately, as described above, in contrast to hanging wall domains, very often deformations along a footwall of large non-vertical normal faults that record

a plane dip have deteriorated seismic resolution due to a reduced rate of propagating seismic waves through a fault plane.

In order to predict the footwall drag shape and more importantly the position of a contact with adjacent fault plane (cutoff), the two key factors, hanging wall fault drag amplitude and the position of fault tips needs to be constrained beforehand. Surprisingly, disarrangement between the footwall and hanging wall amplitudes (e.g. Fig 4-6a) induced by an unequal fault slip ratio has a minimized effect on prediction of the position of a footwall reverse drag (see Fig 4-6a).

According to the elastic analytical solutions (Pollard and Segall, 1987) both reverse and normal fault drag develops around planar fault segments (Grasemann et al, 2005), whereby reverse drag refers to the markers that are concave in the direction of a fault slip. (e.g. Fig. 4-9c, markers 1a, 1b and 2). According to the model, the highest amplitudes of the hanging wall reverse drag are associated to central fault sections. Taking this relationship into account, the here exhibited footwall prediction technique is based upon this central and near-central markers that are associated to the fault sections characterized by highest displacement (Fig 4-9c and 4-9d markers 1a and 1b). In order to facilitate a footwall prediction technique that can be also applied in the case of a segmented fault, in further text will be regarded complicated deformation pattern of after-segments linkage (Fig 4-9c, Stage 3). Since displacement gradually decreases away from the central fault section towards the tips, causing contemporaneous reverse drag amplitude decrease, eventually in the proximity of fault tips reverse drag abruptly transits to a normal drag (Fig 4-9c, stage 3 thinner pale black lines). As a consequence, the along slip fault drag amplitude migrates and changes drag sense, hence variations in drag amplitude indicate the position of fault tips, which might be very useful for discriminating inherited tips among linked segments (Wiesmary and Grasemann, 2005).

Once the position of fault tips is identified, another important issue is the structural level of the footwall drag, i.e. determining if the marker displays is an offset in the far field. If the investigated marker is not displaced in a far fault field (e.g. markers 1a and 1b at Fig 4-9d), the geometry of the assumed central marker in the hanging wall can simply be mirrored in the footwall whereby according to the same elastic model of Grasemann et al. (2005), the footwall geometry has exactly the same shape as the hanging wall anticline.

However, very often a hanging wall marker is displaced in subsequent deformation phase resulting in a downwards directed slip of the hanging wall (e.g. marker h2, Fig 2b). Similarly, the prediction of displaced footwall marker geometry can be achieved by mirroring of the hanging wall marker (Fig 9d, marker 1a') at the level of the corresponding chronostratigraphic horizon in the footwall (1b in Fig 9d).

In summary, a detailed structural investigation of reverse and normal drag in the hanging wall of a normal fault may not only identify hydrocarbon traps in the hanging wall, but may be used to extrapolate footwall drag geometries which commonly remain unexplored for hydrocarbon reservoirs.

4.6 <u>Conclusions</u>

The presented structural model mapped from a 3D seismic of the Markgrafneusiedl natural fault in the Vienna basin focuses on near-fault deformations of marker horizons in the hanging wall of the fault. Using this additional information to conventional displacement distance plots and fault morphology, we conclude:

(1) Fault drag is the near-fault feature that can occur at basin scale.

(2) Including fault drag into the established methods of fault analysis (fault morphology and displacement) gives additional information on initial segmentation and segment linkage during fault growth.

109

(3) Fault segments and fault drag are scale-dependent, whereby large segments consisted of linked local faults are accompanied by similar size fault drag that is comprised of local drag substructures. Around propagating fault tips, a normal drag may develop, however unlike drag around segment centers, drag originating from a tip propagation contains no substructures. Therefore, such fault drag hierarchy can promptly disclose parent and overlapping fault segments.

(4) Investigation of fault drag allows prediction of the geometry and position of footwall horizons, which may record only bad signal in 3D seismics. Syncline geometry characterized for a footwall drag can expand the hydrocarbon exploration on below-fault blurred seismic domains.

(5) The investigation results clearly warned that not always, an intuitive, shuffle-shaped fault surface comprised of relatively mild dip values necessarily leads towards the listric fault model, but requires more detailed morphological, kinematical and near-fault deformation analyses.

Acknowledgements

References

Ackermann, R. V., Schlishe, R.W., Withjack, M.O. (2001), The geometrical and statistical evolution of normal fault systems: an experimental study of the effects of mechanical layer thickness on scaling laws, J. of Struct.Geol., 23, 1803-1819.

Barnett, J. A. M., Mortimer, J., Rippon, J.H., Walsh, J.J., Watterson, J. (1987), Displacement Geometry in the Volume Containing a Single Normal Fault. , AAPG Bull., B 71, 925-937.

Beidinger, A. (2009), Geophysical, geomorphologic and geological investigations along the Lassee-Segment of the Vienna Basin Transfer Fault System (VBTF), 2009, Unpub. Mast. Thesis., pp 82.

Brix, F., Schultz, O. (1993), Erdöl und Erdgas in Össtereich. pp 688.

Bürgmann, R., Pollard, D.D., Martel. S.J. (1994), Slip distributions on faults: effects of stress gradients, inelastic deformation, heterogeneous host-rock stiffness, and fault interaction, J. of Struct.Geol., 16, 1675-1690.

Cartwright, J. A., Trudgill, B.D, Mansfield C.S. (1995), Fault growth by segments linkage: an explanation for scatter in maximum displacement and trace lenth from the Canyonlands Grabens of SE Utah, J. of Struct.Geol., 17, 1319-1329.

Childs, C., Nicol, A., Walsch, J.J., Watterson J. (1996), Growth of vertically segmented normal faults, J. of Struct.Geol., 18, 1389-1397.

Childs, C., Nicol, A., Walsch, J.J., Watterson J. (2003), The growth and propagation of synsedimentary faults, J. of Struct.Geol., 25, 633-648.

Coelho, S., Passchier, C., Grasemann, B. (2005), Geometric description of flanking structures, J. of Struct.Geol., 27, 597-606.

Contreras, J., Anders, M.H., Scholz, C.H. (2000), Growth of a normal fault system: observations from the Lake Malawi basin of the east African rift, J. of Struct.Geol., 22, 159-168.

Cowie, P. A., Shipton Z.K. (1998), Fault tip displacement gradients and process zone dimensions, J. of Struct.Geol., 20, 983-997.

Davis, K., Burbank, D.W., Fisher, D., Wallace, S., Nobes, D. (2005), Thrist-fault growth and segment linkage in the active Ostler fault zone, New Zealand, J. of Struct.Geol., 27, 1528-1546.

Dawers, N. H., Anders, M.H. (1995), Displacement-length scaling and fault linkage, J. of Struct.Geol., 5, 607-614.

Decker, K. (1996), Miocene tectonics at the Alpine-Carpathian junction and the evolution of the Vienna Basin, Mitteilungen der Gesellschaft der Geologie- und Bergbaustudenten, 41, 33-44.

Decker, K., Peresson, H., Hinsch, R. (2005), Active tectonics and Quaternary basin formation along the Vienna Basin Transform fault, Quat.Sci. Rev., 24, 307-322.

Exner, U., Mancktelow, N.S., Grasemann, B. (2004), Progressive development of s-type flanking folds in simple shear, J. of Struct.Geol., 26, 2191–2201.

Fodor, L. (1995), From transpression to transtension: Oligocene-Miocene structural evolution of the Vienna basin and the East Alpine-Western Carpathian junction, Tectonophys., 242, 151-182.

Fuchs, R., Hamilton, W. (2006), New depositional architecture for an old Giant: the Matzen field, Austria. In: Golonka, J., Pischa, F.J. (Eds.), The Carpathians and their foreland: Geology and hydrocarbon resources, AAPG Memoir, 84, 205-219.

Gawthorpe, R. L., Jackson, A.-L.C., Young M.J., Sharp, .I.R, Moustafa, A.R., Leppard, C.W. (2003), Normal fault growth, displacement localisation

and evolution of normal fault populations: the Hammam Faraun fault block, Suez rift, Egypt, J. of Struct.Geol., 25, 883-895.

Grasemann, B., Martel, S., Passchier, C. (2005), Reverse and normal drag along a fault, J. of Struct.Geol., 27, 999-1010.

Grasemann, S., K., Vannay, J.-C. (2003), Sense and non-semse of shear in flanking structures, J. of Struct.Geol., 25, 19-34.

Gupta, A., Scholz, C.H. (2000), A model of normal fault interaction based on observations and theory, J. of Struct.Geol., 22, 865-879.

Hamilton, W., Wagner, L., Wessely, G. (2000), Oil and gas in Austria, Mitteil. der Österr.Geol. Gesell., 92, 235-262.

Harzhauser, M., Daxner-Höck, G., Piller, W.E. (2004), An intergrated stratigraphy of the Pannonian (Late Miocene) in the Vienna Basin, Austrian J. of Earth Sci., 95/96, 6-19.

Hinsch, R., Decker, K., Wagreich, M. (2005a), 3-D mapping of segmented active faults in the southern Vienna Basin, Quat. Sci. Rev., 24, 321-336.

Hinsch, R., Decker, K., Peresson, H. (2005b), 3D seismic interpretation and structural modelling in the Vienna Basin: implications for Miocene to recent kinematics, Austrian J. of Earth Sci., 97.

Hölzel, M., Wagreich, M., Faber R., Strauss, P. (2008), Regional subsudence analysis in the Vienna Basin (Austria), Austrian J. of Earth Sci., 101, 88-98.

Hölzel, M., Decker, K., Zámolyi, A., Strauss, P., Wagreich, M (2010), Lower Miocene structural evolution of central Vienna Basin, Mar. and Petrol. Geol., 27, 666-681.

Kasahara, K. (1981), Earthquake Mechanics, Cambr. Unive. Press, Cambridge.

Kelly, P. G., Peacock, D.C.P., Sanderson, D.J. (1998), Linkage and evolution of conjugate strike-slip fault zones in limestones of Somerset and Northumbria, J. of Struct.Geol., 20, 1477-1493.

Kim, Y.-S., Sanderson, D.J. (2005), The relationship between displacement and length of faults: a review, Earth-Sci. Rev., 68, 317-334.

Kristensen, M. B., Childs, C.D., Korstgård, J.A. (2008), The 3D geometry of small-scale relay zone between normal faults in soft sediments, J. of Struct.Geol., 30, 257-272.

Kröll, A., Wessely, G (1993), Wiener Becken und angrenzende Gebiete. Geologische Themenkarte der Rep. Österreich 1:200.000., Geolog. Bundesanst. Wien.

Linzer, H.-G., Decker, K., Peresson, H., Dell`Mour, R., Frisch, W. (2002), Balancing lateral orogenic float of the easten Alps, Tectonophys., 354, 211-237.

Lisle, R. J., Toimil, N. (2007), Defining folds on three-dimensional surfaces, Geol.l Soc. of Am., 35, 519-522.

Lohr, T., Krawczyk, C.M., Oncken, O., Tanner, D.C. (2008), Evolution of a fault surface from 3D attribute analysis and displacement measuremants, J. of Struct.Geol., 30, 690-700.

Maerten, L., Willemse, E.J.M., Pollard, D.D., Rawnsley, K. (1999), Slip distributions on intersecting normal faults, J. of Struct.Geol., 21, 259-271.

Mansfield, C. S., Cartwright, J.A (2000), Stratal fold patterns adjacent tonormal faults: observations from the Gulf of Mexico. In: Cosgrove, J.W., Ameen, M.S. (Eds.), Forced Folds and Fractures, Geol. Soc. Spec. Pub., , vol. 169, 115–128.

Marchal, D., Guiraud, M., Rives, T. (2003), Geometric and morphologic evolution of normal fault planes and traces from 2D to 4D, J. of Struct.Geol., 25, 135-158.

Martel, S. J. (1997), Effects of Cohesive Zones on Small Faults and Implications for Secondary Fracturing and Fault Trace Geometry, J. of Struct.Geol., 19, 835-847.

McClay, K. R. (1990), Extensional fault systems in sedimentary basins: a review of analogue model studies. , Mar. Petrol. Geol., 7, 206–233.

McConnell, D. A., Kattenhorn, S.A., Benner, L.M (1997), Distribution of fault slip in outcrop-scale fault-related folds, Appalachian Mountains, J. of Struct.Geol., 19, 257–267.

Mynatt, I., Bergbauer, S., Pollard, D.D. (2007), Using differential geometry to describe 3-D folds, J. of Struct.Geol., 29, 1256-1266.

Nicol, A., Walsh, J.J., Watterson J., Breatn, P.G. (1995), Three-dimensional geometry and growth of conjugate normal faults, J. of Struct.Geol., 17, 847-862.

Nicol, A., Watterson J., Walsh, J.J., Childs, C. (1996), The shapes, major axis orientations and displacement patterns of fault surfaces, J. of Struct.Geol., 18, 235-248.

Passchier, C. W. (2001), Flanking structures, J. of Struct.Geol., 23, 951–962.

Peacock, D. C. P., Sanderson, D.J. (1991), Displacements, segment linkage and relay ramps in normal fault zones, J. of Struct.Geol., 13, 721 - 733.

Peacock, D. C. P., Sanderson D.J. (1996), Effects of propagation rate on displacement variations along faults, J. of Struct.Geol., 18, 311-320.

Peacock, D. C. P. (2002), Propagation, interaction and linkage in normal fault systems, Earth-Sci. Rev., 58, 121-142.

Peresson, H., Decker, K. (1997), The Tertiary dynamics of the northern Alps (Austria): changing palaeostresses in a collisional plate boundary, Tectonophys., 272, 125-157.

Pollard, D. D., Segall, P. (1987), Theoretical displacements and stresses near fractures in rocks. , In: Atkinson, B.K. (Ed.), Fracture Mechanics of Rock. Academic Press, London, pp. 277–349.

Porras, J. S., Vallejo, E.L., Marchal, D., Selva, C. (2003), Extensional folding in the Eastern Venezuela Basin: examples from fields of Oritupano-Leona Block, Search and Discovery, Article #50003:50007.

Ratschbacher, L., Merle, O., Davy, P., Cobbold, P. (1991), Lateral extrusion in the eastern Alps: Part I. Boundary conditions and experiments scaled for gravity., Tectonics 10 (2), 245–256.

Reches, Z., Eidelman, A (1995), Drag along faults, Tectonophys., 247, 145-156.

Resor, P. G. (2008), Deformation associated with a continental normal fault system, western Grand Canyon, Arizona, GSA Bull., 120, 414-430.

Rippon, J. H. (1985), Contoured patterns of throw and hade of normal faults in the coal measures (Westphalian) of northeast Derbyshire, Proc. of the Yorkshire Geol. Soc., 45, 147–161.

Royden, L. H. (1985), The Vienna Basin: a thin-skinned pull-apart basin. In: Biddle, K.T., Christie-Blick, N. (Eds.), Strike Slip Deformation, Basin Formation and Sedimentation, Society of Economic Paleontologists and Mineralogists, Spec.Pub., 37, 319– 338.

Rykkelid, E., Fossen, H. (2002), Layer rotation around vertical fault overlap zones: observation from seismic data, field examples, and physical experiments, Mar. and Petro. Geol., 19, 181-192.

Sauer, R., Seifert, P., Wessely, G. (1992), Guidbook to excursions in the Vienna Basin and the adjacent Alpine –Carpathian thrustbelt in Austria, Mitteil. der Geolog. Gesell., 85, 1– 264.

Spahić, D., Exner, U., Behm, M., Grasemann, B., Haring, A., Pretsch, H (in press), Listric versus planar normal fault geometry: an example from

the Eisenstadt-Sopron Basin (E Austria), Int. J. of Earth Sci., DOI 10.1007/s00531-00010-00583-00535.

Strauss, P., Harzhauser, M., Hinsch, R., Wagreich, M. (2006), Sequence stratigraphy in a classic pullapart basin (Neogene, Vienna Basin). A 3D seismic based integrated approach

Geol.Carp., 57, 185-197.

Tearpock, D. J., Bischke, R.E. (2003), Applied Subsurface Geological Mapping, pp 821.

Walsh, J. J., Watterson, J. (1989), Displacement gradients on fault surfaces, J. of Struct.Geol., 11, 307-316.

Walsh, J. J., Watterson, J., Bailey, W.R., Childs, C. (1999), Fault relays, bends and branch lines, J. of Struct.Geol., 21, 1019-1026.

Walsh, J. J., Nicol, A., Childs, C. (2002), An alternative model for the growth of faults, J. of Struct.Geol., 24, 1669-1675.

Walsh, J. J., Bailey, W.R., Childs, C., Nicol, A., Bonson C.G. (2003), Formation of segmented normal faults: a 3-D perspective, J. of Struct.Geol., 25, 1251-1262.

Watterson, J. (1986), Fault dimensions, displacements and growth, Pure Appl. Geophys., 124, 365-373.

Weissenbäck, M. (1996), Lower to Middle Miocene sedimentation model of the central Vienna Basin. In: Wessely, G., & Liebl, W- (eds.): oil and gas in Alpidic thrustbelts and Basins of the Central and Eastern Europe., EAGE Spec.Publ., 5, 355-363.

Wessely, G. (1988), Structure and development of the Vienna basin in Austria. In: Royden LH, Horváth F (eds), AAPG Bull, 45, 333–346.

Wiesmayr, G., Grasemann, B. (2005), Sense and non-sense of shear in flanking structures with layer-parallel shortening: implications for fault related folds, J. of Struct.Geol., 27, 249–264.

Yamada, Y., McClay K. (2003), Application of geometric models to inverted listric fault systems in sandbox experiments. Paper 1: 2D hanging wall deformation and section restoration, J. of Struct. Geol., 25, 1551–1560.

Zee, W. v.-d., Urai, J.L. (2005), Processes of normal fault evolution in a siliciclastic sequence: a case study from Miri, Sarawak, Malaysia, J. of Struct.Geol., 27, 2281-2300.

5.Synthesis: importance of fault drag criterion in assessment of fault surface geometry and segmented pattern

5.1 <u>General conclusions</u>

The correct interpretation and recognition of faults and associated near field deformations, i.e. fault drag, are fundamental for a comprehensive reconstruction of the kinematics and history of fault propagation. Based on balancing methods and 3D visualization of natural fault and fault drag structures that are presented in this thesis, the importance of near fault deformation around planar discontinuities is stressed out and several new insights are obtained.

5.1.1 Significance of 3D structural modeling

The understanding of processes, which are linked to deformations in the Earth's crust, various balancing techniques as well as scales analogue models provide best visualization tools subsequently used for physical models. Such structural quantifications need as many quantitative constraints for the setup of appropriate models as possible. One major group of important input data is the spatial geometry of geological surface and subsurface structures.

Using 3D modeling, we spatially visualized the relation between two different types of structures (e.g. Fig 6-1), which is very often only detectable partially in cross sections (fault traces and profile of fault drag). Furthermore 3D visualization is a proven tool to detect relations between different data sets, which otherwise are hidden or unclear, e.g. fault traces exposed on outcrop and 3D spatial visualization of same traces behind an outcrop.

Data examples and resulting interpretations are discussed in the frame of existing models of the Vienna Basin system focusing on some important

differences between the Miocene meso- and large-scale fault and near-fault deformation systems.
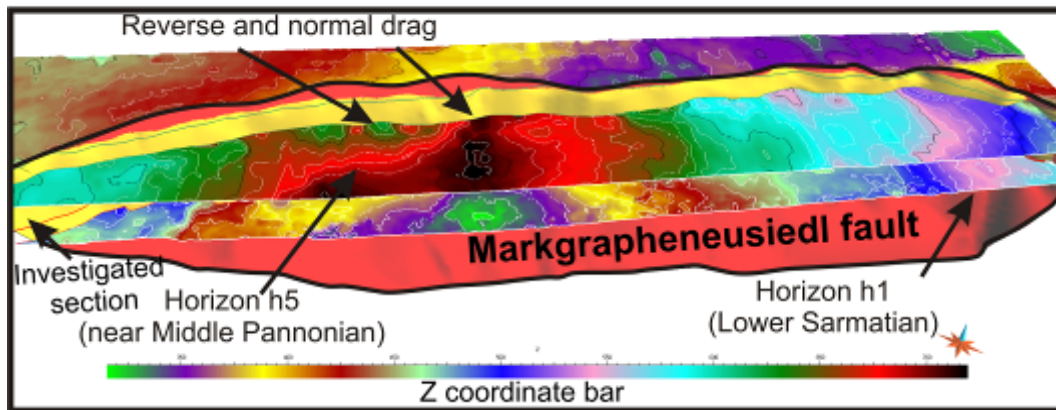

Fig.6-1. Oblique view of the depth migrated structural 3D model of the Markgrafneusiedl fault and near-fault markers.

5.1.2 Reverse fault drag and geometrical fault models

Using a set of visualization (GPR and 3D seismic), modeling and balancing methods, the large deflections of initially planar markers around two regional normal faults is investigated. Initially, the resulting balanced solution implicated that large-scale reverse drag structure has been developed around the final length normal fault (Chapter 3). The application of combination of field mapping, GPR, and depth-to-detachment balancing method revealed:

> **(1)   NO LISTRIC OR DOWNWARDS FLATTENED FAULT SECTION OR SMALLER-SCALE DETACHMENT IS OBSERVED ALONG THE FAULT EXPOSED ON GRAVEL PIT NEAR ST. MARGAREHTEN; NEITHER IS A WEAK DETACHMENT (E.G. CLAY OR SALT LAYER) IN A LOWER STRUCTURAL LEVEL OF THE NORMAL FAULT DISOCVERD, RESULTING IN A DISMISSAL OF BOTH A LISTRIC FAULT SENSU STRICTU OR A TECTONIC RAFT SYSTEM.**

Subsequently the presented structural model mapped from a 3D seismic block of the Markgrafneusiedl normal fault in the Vienna basin (chapter 5) focuses on the deformation of marker horizons in the hanging wall of the fault. Using this additional information to conventional displacement distance plots and fault morphology, we conclude:

(2) **THE INVESTIGATIONS OF DEFLECTED MARKER HORIZONS NEAR THE IRREGULAR MARKGRAFNEUSIEDL FAULT SURFACE PROVE THAT FAULT DRAG IS A FUNCTION OF A SINGLE PROPAGATING SEGMENTS AS WELL AS FROM THEIR COALESCENCE AND SUBSEQUENT GROWTH**

### 5.1.3 Fault drag as criterion to recognize fault segments

Investigation and identification of coalesced fault segments has been commonly comprised of the displacement distribution analysis sometimes combined with studies of fault morphology (e.g. Watterson, 1986; Barnett et al., 1987; Walsh and Watterson, 1989; Cartwright et al, 1995; Contreras et al., 2000; Kim and Sanderson, 2005; Marchal et al., 2003; Lohr et al., 2008a). Although displacement analyses provide satisfactory results, very often displacement-distance graphs exhibit ambiguous disturbed elliptical shape (Nicol et al, 1996).

The basic principles of geometrical fault drag analysis discussed in Chapter 4 assume that fault drag is a function of each active fault segment induced by displacement asymmetry. Therefore, the argument of the aforementioned study is that quantification studies of fault drag can be used as an additional tool in recognition of fault segments and importantly for reconstruction of the overall fault evolution. Consequently, the investigations of a planar-segmented mature fault that records a displacement gradient revealed that the evolution of each segment can induce a local different scale-dependent development of fault drag in the adjacent marker horizons. Deciphering different origin of propagating fault segments by using a combination of fault morphology and drag amplitude studies, it was

concluded that fault drag can help to distinguish parent from linkage or relay faults.

5.1.4 Progressive evolution of segmented faults reconstructed by fault drag amplitude criterion

The models that describe fault drag with segmented fault growth are limited. The model of vertical segment propagation (Wiesmayr, 2005) investigates the 2D distribution of fault drag around two finite length fault segments. Reverse drag develops in the center of a fault segment whereby normal drag is associated with segment tip zone. (Fig 4-10 in Wiesmayr, 2005).
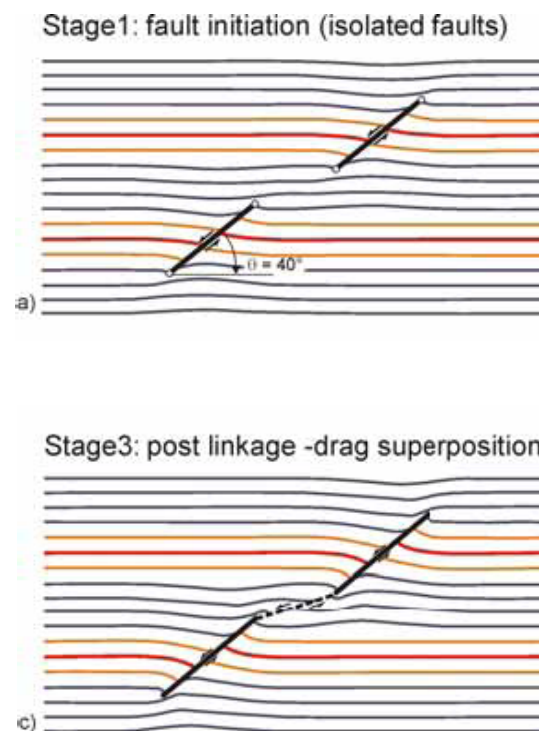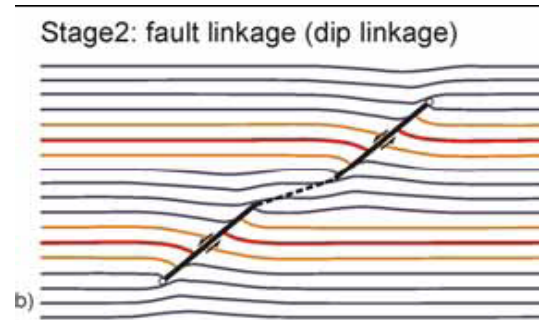
Figure 6-2: 3-stage conceptual model based on flanking structure theory according to Wiesmayr, 2005. *a) Stage 1: Isolated flanking structures develop along planar fault segments, fault tips remain stationary. b) Stage 2: Fault tips propagate and individual fault segments start to link to form a segmented normal fault. c) Stage 3: Post-linkage fault displacement occurs and forms fault drag superposition on shallow segments*.

In chapter 5 the usefulness of the fault drag as a criterion to characterize the evolution of segmented faults was analyzed. Linking the study of drag magnitude, its evolution and role in segment linkage emphasized the importance of this structural feature. The study has shown how additional information can be gained from detailed structural mapping of fault drag, which significantly extends the recognition of fault segments from displacement-distance measurements and other geometrical parameters of the fault surface.

5.2 <u>Presented solutions and future outlook</u>

5.2.1 Numerical modeling of propagating segments and associated fault drag

Often natural examples of structural phenomena have been used to confirm application and results of numerical analyses and theoretical results. Despite the complex relationship between fault segmentation and fault drag illustrated by the model of the Markgrafneusiedl fault, numerically computed fault drag behavior during segment linkage could indicate development of

fault drag around local perturbations, depicting the mechanical behavior during processes of segment propagation and subsequent linkage.

Analytical models of the instantaneous displacement field around an isolated fault in an infinite elastic body predict that fault drag develops on both sides of the fault (Grasemann et al., 2005). Theoretical displacement field around a single dip-slip fault that reveal normal and reverse drag develop due to a slip confirmed by the model predicting increase of drag magnitudes toward the center of fault. Additionally, the angular relationship between the fault surface and the adjacent layers is constrained, whereby normal drag develops around low angle fault and reverse drag occurs around a high angle fault.

Using constrains of the above analytical solution, numerical models could capture fault drag amplitude development during fault propagation. The investigation of perturbed fault-slip distributions with complex three-dimensional geometries has been performed using the Boundary Element Method (e.g. Maerten et al., 1999). The results could provide additional constraints and confirm the proposed scenario of the development of the segmented Markgrafneusiedl normal fault (Chapter 4).

5.2.2 Predicting possible weak zones near faults in hydrocarbon reservoirs

Fractured reservoirs can be difficult to model and to exploit. The key to a better understanding of sub-seismic structures lies in well data, but commonly limited use is made of the vital data collected from core and borehole images, even though these data provide the only direct information about joints in hydrocarbon reservoirs. However, in the following the role of fault drag in understanding of fracture distribution near hydrocarbon reservoirs will be emphasized.

According to the inhomogeneous fault roughness, the rocks around the fault should show an inhomogeneous strain field with high fracture

concentration in areas of strong fault undulations or high curvature (Lohr et al., 2008a). Here, analyzed zones of high curvature are actually different-scale small segment centers accompanied by reverse fault drag. These zones of high curvature are affected by higher deformation in the surrounding horizons induced by larger displacement along the fault, and therefore should be characterized by a higher fracture density in these horizons adjacent to the fault. Thus, a large segmented fault surface can exhibit a variable fracture density in the adjacent host rock along both fault strike and fault depth. From fault plane and fault drag analysis on the here studied scale, it might be possible to make qualitative predictions about fracture density around the major fault.

However, the influence of fault drag on a much smaller scale, e.g. below the seismic resolution down to a few meters or even well data scale is rather unexplored. Investigations of fault drag might help to localize strongly fractured zones not visible in seismic data (e.g. Lohr et al., 2008b), which is important for analyses of fluid migration and for reservoir characterization.

The complexity of the segmentation of a near-fault reservoir can lead to the development of discrete fault blocks resulting in the compartmentalization of a reservoir (e.g Freeman et al, 1998; Myers et al, 1998; Harris et al., 2003). Such geometrical complexity can cause a significant stress variation across the hydrocarbon reservoir (Yale, 2003; Morris and Ferrill, 2009; Maerten et al, 2002), and therefore a segmented surface might affect fault sealing properties due to the development of fracture zones (e.g. Aydin, 2000). Consequently, sealing efficiency (Harris et al, 1998), trap integrity, and compartmentalization could be initially illustrated by using a fault drag geometrical study in addition to analysis of the fault surface geometry. The concept could be based on a fault segmentation pattern adjacent to a hydrocarbon reservoir, whereby the most important step is the delineation of the areas of a radical change in segment orientation that can often represent local deformation zones characterized by intensive fracturing (e.g Barr, 1998; Tearpock and Bischke,

2005; Aarland and Skjervena, 1998). These zones as a product of dominant strain component accommodated by large faults (Lohr et al., 2008b) additionally can be delineated by analyzing fault drag geometry. Using intense changes in fault plane orientation frequently assigned as a transfer or tip zone, which could be confirmed by the change from reverse to normal drag along the fault plane, as shown on the example of the Markgrafneusiedl fault (Fig 6-3).
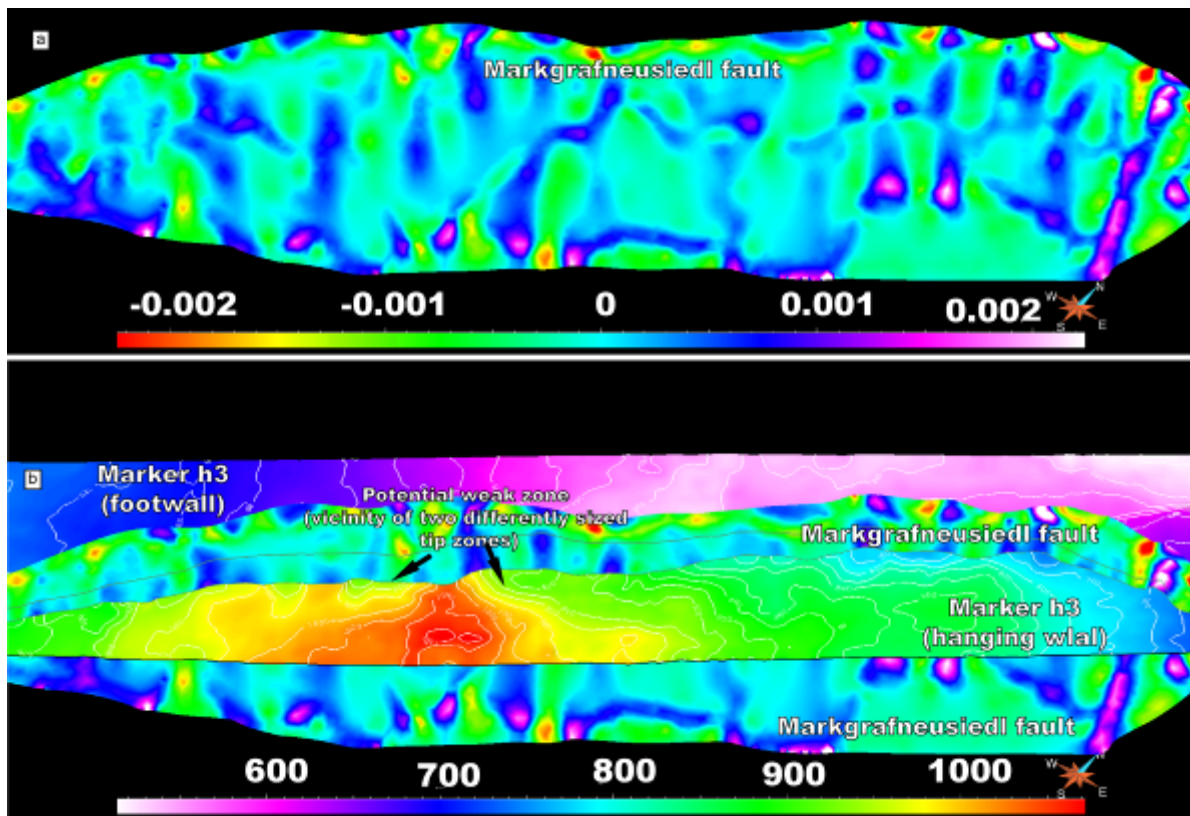

Fig. 6-3. Oblique view on the 3D Markgrafneusiedl fault surface. (a) Gaussian curvature map exposing the fault undulations; (b) Combination of the same 3D fault undulations with 3D fault drag can delineate potential weak zones (black arrow).

References

Aarland, R. K., Skjerven, J. 1998. Fault and fracture characteristics of a major fault zone in the northern North Sea: analysis of 3D seismic and oriented cores in the Brage Field. In: Coward, M. P., Databan, T. S. & Johnson, H. (eds) Structural Geology in Reservoir Characterization. Geological Society, London, Special Publications 127, 209-229.

Aydin, A. 2000. Fracture, faults, and hydrocarbon entrapment, migration and flow. Marine and Petroleum Geology 17, 797-814.

Barnett, J. A. M., Mortimer, J., Rippon, J.H., Walsh, J.J., Watterson, J. . 1987. Displacement Geometry in the Volume Containing a Single Normal Fault. American Association pf Petroleum Geologists B 71, 925-937.

Barr, D. 1998. Conductive faults and sealing fractures in the West Sole gas fields, southern North Sea. In: Coward, M. P., Databan, T. S. & Johnson, H. (eds) Structural Geology in Reservoir Characterization. Geological Society, London, Special Publications 292, 431-451.

Cartwright, J. A., Trudgill, B.D, Mansfield C.S. 1995. Fault growth by segments linkage: an explanation for scatter in maximum displacement and trace lenth from the Canyonlands Grabens of SE Utah. Journal of Structural Geology 17, 1319-1329.

Contreras, J., Anders, M.H., Scholz, C.H. 2000. Growth of a normal fault system: observations from the Lake Malawi basin of the east African rift. Journal of Structural Geology 22, 159-168.

Freeman, B., Yielding, D.T., Needham, D.T., Badley, M.E. 1998. Fault seal prediction: the gouge ratio method In: Coward, M. P., Databan, T. S. & Johnson, H. (eds) Structural Geology in Reservoir Characterization. Geological Society, London, Special Publications 127, 209-229.

Grasemann, B., Martel, S., Passchier, C. 2005. Reverse and normal drag along a fault. Journal of Structural Geology 27, 999-1010.

Harris, S. D., McAllister, E., Knipe, R.J., Oding, N.E. 2003. Predicting the three-dimensional population characteristics of fault zones: a sudy using stochastic models. Journal of Structural Geology 25, 1281-1299.

Kim, Y.-S., Sanderson, D.J. 2005. The relationship between displacement and length of faults: a review. Earth-Science Reviews 68, 317-334.

Lohr, T., Krawczyk, C.M., Oncken, O., Tanner, D.C. 2008a. Evolution of a fault surface from 3D attribute analysis and displacement measuremants. Journal of Structural Geology 30, 690-700.

Lohr, T., Krawczyk C. M., Tanner, D., Samiee, R., Endres, H., Thierer, P.O., Oncken, O., Trappe, H., Bachmann, R., Kukla, P. 2008b. Prediction of subseismic faults and fractures: Integration of three-dimensional sismic data, three-dimesnional retrodeformation, and well data on an example of deformation around an inverted fault. AAPG Bulletin, V.92, 473-485.

Maeten, L., Gillespie, P., Pollard, D.D. 2002. Effects of locall stress perturbation on secondary fault development. Journal of Structural Geology 24, 145-153.

Marchal, D., Guiraud, M., Rives, T. 2003. Geometric and morphologic evolution of normal fault planes and traces from 2D to 4D. Journal of Structural Geology 25, 135-158.

Myers, R. D., Allgood, A., Hjellbakk, A., Vrolijk, P., Breidis, N. 1998. Testing fault transmissibility predictions in a strcuturally dominated reservoir: Ringhorne field, Norway. In: Coward, M. P., Databan, T. S. & Johnson, H. (eds) Structural Geology in Reservoir Characterization. Geological Society, London, Special Publications 292, 271-294.

Nicol, A., Walsh, J.J., Watterson J., Breatn, P.G. 1995. Three-dimensional geometry and growth of conjugate normal faults. Journal of Structural Geology 17, 847-862.

Tearpock, D. J., Bischke, R.E. 2003 Applied Subsurface Geological Mapping. pp 821.

Walsh, J. J., Watterson, J. 1989. Displacement gradients on fault surfaces. Journal of Structural Geology 11, 307-316.

Yale, D. 2003. Fault and stress magnitude controls on variations in the orientation of in situ stress. From: Ameen, M. (ed.) Fracture and In-Situ Stress Characterization of Hydrocarbon Reservoirs. Geological. Society, London, Special Publications 209, 55-64.

6. Appendix 1

CURRICULUM VITAE

CURRICULUM VITAE – DARKO SPAHIĆ, STRUCTURAL GEOLOGIST (3D MODELER)

SUMMARY
A geologist with almost 10 years of multidisciplinary geological experience collected in Algeria, Angola, Austria, Hungary, Italy, Libya, Serbia, Spain and Tunisia. Proven in applied subsurface research – and direct operational experience in both offshore & onshore operations: have conducted geological mud logging/wellsite geology and rig monitoring for vertical and horizontal wells. In general, along with a background in sequence stratigraphy, 3D geomodeling, field engineering, petrophysics, and expertise in structural geology, have relevant safety and petroleum industry trainings, excellent technical and IT abilities. As a proven team lead/player and innovative thinker, I have excellent communication abilities and presentation skills, fluent in English, German, Russian, and Italian.
OBJECTIVE
TO WORK AS A CONSULTANT GEOLOGIST (STRUCTURAL GEOLOGIST/3D MODELER).

ACADEMIC QUALIFICATIONS	
October 2007- October 2010	**PH.D. CANDIDATE** in advanced structural geology, University of Vienna, Austria, Department for Geodynamics and Sedimentology . Geozentrum,, Althanstrasse 14, 1090, Vienna, Austria.
2001 – 2006	**M.SC OR MAGISTER DIPLOMA** in Tectonics/Structural Geology (hon.), University of Belgrade, Faculty of Mining and Geology, Department of Dynamic Geology/Tectonics. Djušina 7, 11000 Belgrade, Serbia.
1993 – 1999	**GEOLOGICAL ENGINEERING DIPLOMA IN REGIONAL GEOLOGY** (5 years). (hon.), (equivalent to Diploma in Geology/Paleontology according to Bologna Program) - University of Belgrade, Faculty of Mining and Geology, Department of Regional Geology and Paleontology. Djušina 7, 11000 Belgrade, Serbia.

CAREER HISTORY	
October 2007 – October 2010:	**RESEARCH ASSOCIATE** at the Department for Structural Geology and Sedimentology, University of Vienna, Austria, engaged on Project: "Modeling of faults in various scales". http://geologie.univie.ac.at/structural-processes-group/current-projects/natural-fault-geometries/
Sept 2004 to September 2007:	**ASSISTANT OF CHIEF OF GEOLOGICAL DEPARTMENT**, Geological Survey of Serbia and International Research Center, Tripoli, Libya. Surface mapping/exploration of the Sirte Basin (Libya) contracted as Structural Geologist, Senior Mapping Geologist (Sheet Coeditor) and Arc GIS specialist.
July 2002 to August 2004:	Geoservices International, Paris, France. http://www.geoservices.com **GEOLOGICAL DATA ENGINEER** - Angola: Cabinda deep off-shore, Semisub Sedneth 701, client Chevron-Texaco, 12/2003 – 08/2004. **SENIOR LOGGING GEOLOGIST** – Algeria, Hassi Messaoud, El Merk North….client Groupment Berkine Anadarko, 11/2002-12/2003. Logging Geologist – Italy on-shore: Villa d`Agri, client Agip, 09/2002-11/2002.
June 2001 to June 2002:	**RESEARCH & TEACHING ASSISTANT**, Faculty of Mining & Geology, Belgrade, Department for Geological mapping. Structural geologist interpretation of 2-D seismic sections (Drmno Project, southern Pannonian Basin, Serbia and Serbo-Macedonian Unit); http://www.rgf.bg.ac.rs/

WORK SKILLS	
STRUCTURAL & PETROLEUM GEOLOGY	- Structural Interpretation of 2D and 3D Seismic Datasets including construction and 3D models fine-tuning; - Evolution of segmented mature faults – a 3D geometrical fault plane study in order to understand fault evolution (recognition of segments, linkage and overlap zones etc - Near-fault deformation as potential hydrocarbon reservoirs and their significance in trap integrity assessments, sealing efficiency, and compartmentalization risking predictions. - Structural validation - geometrical viability of fault planes in areas with complex deformational styles; - Field structural mapping: basins and highly deformed terrains; cross-section reconstruction and balancing;
	- Analyze & interpret geological & geophysical data; - Build & evaluate large and detail, complex computerized geological models in Gocad & Petrel 3D modeling software; - Integrate seismic, core, engineering, petrophysical and drilling data into geologic model;
WELLSITE GEOLOGY	- Experience of well monitoring, real time geological logging, engineering among the various geographical regions allowed me comprehensive and self-confident Wellsite Geological work: - Had direct responsibility for, the effective management of the mud logging unit, including personnel and equipment; assisted other well site geological personnel and the drilling operation by monitoring and recording drilling parameters, drilling fluid properties and pumping parameters; provided primary well control surveillance by plotting pressure trends; logging information on the rock formations being drilled by describing geological cuttings and monitoring gas shows; - to analyze, evaluate and describe formations whilst drilling by using cuttings, gas, FEMWD and wireline data; core chips description, pore pressure analyses, picking casing and core points, wireline QA/QC, recognizing unexpected significant drilling breaks, oil fluorescence observations, knowledge of MWD tools such as gamma and resistivity including the knowledge of spatial 3D modeling are valuable assets for geosteering; - experience of HPHT, horizontal or directionally drilled wells including standard vertical wells.
INFORMATION TECHNOLOGY	Geoscientific: - Landmark/GeoGraphix, Paradigm (Gocad), Petrel 2004 & 2009.2, Reflex, Arc GIS, Tectonics FP, Surfer 8, Geogebra (2-D balancing); - General: - Operating systems: Windows NT/2000/XP, Windows Vista & Windows 7 (administrator level); - MS Word, Excel, basics of Access, Corel, Power Point AutoCAD, Adobe Photoshop, Int. Explorer, Fine Reader, etc; - Cartographic expert (drafting): using Adobe Illustrator to draft files from Arc GIS; - Familiar with databases and basic principles of objective oriented programming (C++);
BUSINESS	- Experienced skills as a team leader and project coordinator; experienced in working in multi-cultural, multi-ethnic teams; comfortable working as a team player in a multi-disciplinary and fast-paced environment; - Self-starter, fast learner, motivated and dedicated professional with a reputation for quality work and high standards; - Experience in making presentations, scientific papers & reports in a comprehensive and concise manner;

LANGUAGES (POOR, MEDIUM, GOOD OR FLUENT)				
	LANGUAGE	WRITTEN	SPOKEN	READ
1	English	Fluent	Fluent	Fluent
2	German	Good	Fluent	Fluent
3	Russian	Medium	Good	Fluent
4	Italian	Medium	Good	Fluent
6	Serbian-Croatian–Bosnian	Mother tongue		

LIST OF SELECTED SCIENTIFIC PUBLICATIONS AND PRESENTATIONS

Spahić, D. Exner, U., Grasemann B. (submitted): Identifying fault segments from 3D fault drag analyis. Journal of Geophysical Research.

Spahić, D. Exner, U., Grasemann B. (2010): 3D fault drag characterization: an import tool in a fault description. Geophysical Research Abstracts, Vol. 12, EGU2010-0, 2010. EGU General Assembly 2010.

Spahić D., Exner U., Behm M., Grasemann B., Haring A., Pretsch H. (accepted): Listric versus planar normal fault geometry: an example from the Eisenstadt-Sopron Basin (E Austria). International Journal of Earth Science.

Spahić D., Exner U., Behm M., Grasemann B., Haring A., Pretsch H. (2010): Heterogeneous distribution of the displacement gradient along normal fault system and possibilities of a model prediction, an example from Eastern Austria (Burgenland). 15th Congress of the Geologists of Serbia. May 2010. Belgrade.

Spahic, D. Exner, U., Behm, M., Grasemann, B. & Haring, A. (2009): Chatacterization of shallow normal fault systems in unconsolidated sediments using 3-D ground penetrating radar (SE Vienna Basin, Austria). Geophysical Research Abstracts, Vol. 11, EGU2009-0, 2009. EGU General Assembly 2009.

G. Timár, B. Székely, A. Zámolyi, G. Houseman, G. Stuart, B. Grasemann, E. Dombrádi, A. Galsa, D. Spahic, E. Draganits and the ELTE-Leeds-UniWien Workgroup Team (2009): Neotectonic implications by geophysical surveys of topographic features by Airborne laser scanning in the Neusiedlersee/Ferto area (Austria/Hungary). Geophysical Research Abstracts, Vol. 11, EGU2009-0, 2009. EGU General Assembly 2009.

Spahic, D. Exner, U., Behm, M. & Grasemann, B. & Haring, A. (2008): Structural 3D modelling using GPR in unconsolidated sediments. International Meeting of Young Researchers in Structural Geology and Tectonics,. Vol.28.Trabajos de Geologia. Oviedo. Spain.

Vasić N., K.A.Sherif, Spahić D., Komarnicki S., et.al. (2007): Geological map of Libya in scale 1 : 250.000, sheet Dur At Tálah. Geol.Inst.of Sebia, Belgrade & Int.Res.Cent., Tripoli, Libya.

Marović M., Spahić D., Djoković I., Toljić M. Milivojević J. (2006): Extensional unroofing in the area of the Veliki Jastrebac Dome. Annales Géologiques de la Peninsule Balkanique pour l`anne 2007, 68 : 9-20.

Marović M., Djoković I., Toljić M. Milivojević J. Spahić D. (2006): Paleogene – Lower Miocene deformations of Bukulja – Venčac crystalline (Vardar Zone, Serbia). Annales Géologiques de la Péninsule Balkanique pour l`anne 2007. 68 : 21-27.

Grants, Awards & Professional Affiliations	Award winner for the best Master Thesis Project in Geology - award title "Milan Milićević geological engineer" Faculty of Mining & Geology, Belgrade, 2006. http://www.rgf.bg.ac.yu/rgfNagrade.html Award of International Research Grants winner – South East Europe Geoscience Foundation, 2006; http://www.see-geoscience.org/news.php AGU, EAGE Member.
E-mail Address	E-mail: darko.spahic@univie.ac.at or darkogeo2002@hotmail.com

DARKO'S GEOWORLD
from 2000 to 2010